COMPUTATION IN THE HIGH-CONDUCTANCE STATE

Franziska Ursula Isolde Hellmundt

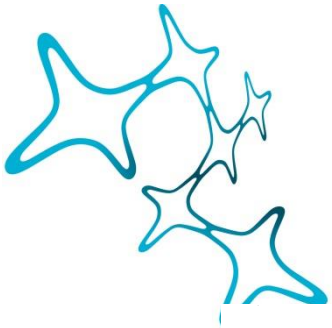

Graduate School of
Systemic Neurosciences

LMU Munich

Dissertation at the
Graduate School of Systemic Neurosciences
Ludwig-Maximilians-Universität München

July, 2019

Supervisor
Prof. Dr. Christian Leibold
Department Biologie II
Ludwig-Maximilians-Universität München

First Reviewer: Prof. Dr. Christian Leibold
Second Reviewer: Prof. Dr. Felix Felmy
External Reviewer: Prof. Dr. Raoul-Martin Memmesheimer

Date of Submission: 26th of July, 2019
Date of Defense : 10th of December, 2019

What if I fall?
Oh, but my darling,
what if you fly?
- Erin Hansen

List of abbreviations

ACN	Anteroventral Cochlear Nucleus
AP	Action Potential
AVCN	Anteroventral Cochlear Nucleus
CN	Cochlear Nucleus
cPSC	compound Postsynaptic Current
DG	Dentate Gyrus
DNLL	Dorsal Nucleus of the Lateral Lemniscus
EC	Entorhinal Cortex
GBC	Globular Bushy Cells
HC	Hippocampus
HF	Hippocampal Formation
ILD	Interaural Level Difference
ITD	Interaural Time Differenc
LFP	Local Field Potential
LSO	Lateral Superior Olive
LTD	Long-Term Depression
LTP	Long-Term Potentiation
MNTB	Medial Nucleus of the Trapezoid Body

MSO	Medial Superior Olive
O-LM	Oriens–Lacunosum-Moleculare
PSC	Postsynaptic Current
SBC	Spherical Bushy Cell
STDP	Spike-Time Dependent Plasticity
SWR	Sharp-Wave Ripple

Summary

At high-conductance state, a neuron is exposed to increased synaptic bombardment. We analyzed the ability of hippocampal pyramidal neurons, as well as the principle cell type of the medial superior olive (MSO), to perform reliable computations under these circumstances. While those neurons come from two completely different brain areas, they are nevertheless ideal study objects, as they are well studied and ample functional knowledge is available.

Pyramidal neurons exhibit sharp-wave ripple events, a specific type of oscillation, during memory consolidation. They are characterized by sharp voltage deflections, accompanied by fast, ripple oscillation. We were interested in the memory capacity of one ripple cycle. To test the correlation between spiking at one cycle with respect to the activity at the previous cycle, the excitatory conductances were modified such that the amplitude of a specific cycle was increased until an AP was generated. We observed only small dependencies between different cycles. Thus, we conclude that a major part of compound postsynaptic currents act as background activity.

In another set of experiments, learning capabilities of a single cell were tested. For this, 10,000 synapses targeting a single cell were simulated, each with the potential to generate postsynaptic currents. Predefined patterns had to be replicated. The number of patterns as well as the coding ratio (percentage of active synapses) were systematically varied.

The compound postsynaptic currents were injected into two different model versions, a multi compartment, Hodgkin-Huxley type neuron, and a single compartment, leaky integrate-and-fire neuron. The leaky integrate-and-fire neuron reflects the synaptic drive of a cell *in vivo*, by allowing to set an optimal firing threshold.

In both models, a small number of patterns can be retrieved using sparse inputs. For physiological sparseness, pattern retrieval was improved in the leaky integrate-and-fire neuron, when adding inhibition, but only at low signal-to-noise ratios.

From our finding, we conclude that the CA1 is an unlikely candidate network for the storage of large numbers of patterns.

Medial superior olive neurons are characterized by a very high membrane conductance, which results in a low probability for action potential generation. However, MSO neurons can produce high firing rates and are known for their precise coincidence detection. To understand this apparent contradiction, we implemented a biophysically inspired, multi-compartment model and combined its finding with results from immunohistochemical stainings and *in vitro* recordings.

The model neuron included a detailed axonal compartment, which allowed to test the impact of the distribution of ionic channels on the firing properties. With the help of *in vitro* patch-clamp recordings we investigated the effect of the input frequency on the firing threshold, by varying this frequency.

One major finding concerns the site at which APs can be generated. With increasing input frequency, a lot of APs in the model are initiated at the nodes of Ranvier, in contrast to the axon initial segment.

Contents

1 Introduction

1.1 The High-Conductance State

The state of a single neuron largely depends on the activity of the network, the cell is embedded in. The high-conductance state describes a cell which is surrounded by active neurons (Destexhe et al., 2003). Typically, this can be observed in an awake animal. During sleep, high-conductance state is comparable to a state in which the neuron exhibits a depolarized membrane voltage, the Up state, in contrast to a more hyperpolarized voltage, the Down state (Paré et al., 1998).
In the high-conductance state, the neuron is exposed to an increased synaptic bombardment. Such high synaptic background activity has several impacts on integration properties of a single cell. A main focus of this thesis is the analysis of the ability of cells to perform reliable computations under these circumstances. The effect of a high-conductance state is discussed with respect to hippcampal pyramidal neurons, as well as to the principle cell type of the medial superior olive (MSO).
Pyramidal neurons represent a well described cell type. Thus, models can be based on well understood physiological parameters. In a high-conductance state, hippocampal pyramidal neurons are more sensitive to normally subthreshold activity and may respond to them (Hô and Destexhe, 2000). Additionally, fast ripple oscillations occur during population burst in the HC and are assumed to play a crucial role in memory consolidation (Buzsáki et al., 1983; English et al., 2014).
MSO cells can integrate inputs with a high temporal precision (Klumpp and Eady, 1956). Interestingly, this precision is enhanced in a high-conductance state (Ratté

et al., 2013).

Thus, both systems benefit from a high conductance state to perform very precise computations, thus enabling them to function as coincidence detectors (Abeles, 1982; Klumpp and Eady, 1956).

Before going into further details, the term conductance needs to be introduced. Conductance is the property that denotes the flow of electric currents. Its inverse, the electrical resistance is calculated as voltage per current. In neurons, the conductance is determined by the composition of ion channels in the membrane. The excitability of neurons is mainly affected by conductance changes. Hence, altering the conductance state of a neuron can result in a changed spiking behavior.

The membrane conductance of a neuron influences the membrane time constant. This time constant describes how quickly the membrane potential of a cell rises or decays. It is calculated as the product of membrane resistance and membrane capacitance. This correlation allows MSO neurons, in high conductance states, to have extremely low time constants, which they need to perform with a high temporal precision (Scott et al., 2005).

A detailed discussion on the impact of this state on the integration properties of single neurons can be found in the discussion chapter, at the end of this thesis.

In the remaining part of the introduction, I will introduce the hippocampus, as well as the MSO. I will start with an overview of the hippocampus, including synaptic connections, area specific cell types, as well as typical oscillations. The subsequent section is dedicated to learning and memory formation. At the end, the focus lies on sound localization, including a section about the MSO.

1.2 Hippocampus

The hippocampus (HC) is a brain region which can be found in both hemispheres within the medial temporal lobe in mammals. Looking at the three-dimensional structure reveals the eponymous shape of the HC, which is often said to resemble the form of a seahorse. The name hippocampus is deduced from the Greek word for seahorse. Another, older, denotation is Cornu Ammonis based on a comparison to a ram's horn. Its abbreviation CA is found in the notation of the

hippocampal subregions.

Being part of the limbic system, the HC was and still is associated with various functions. Early on, a role in the underlying mechanism of processing emotions was suggested. This sparked further research on the brain region (Redish and Touretzky, 1997). Before, the HC had only been mentioned as being involved in olfaction (Brodal, 1947).

The case study of patient H.M. from the 1950s was a meaningful event in the field of memory and the role of the human HC in general (Scoville and Milner, 1957; Milner, 1972). H.M. suffered from severe epilepsy with a focal point in the hippocampal region. As the seizures affected his daily life in a very severe fashion, both hippocampi were surgically removed. As an unexpected consequence, H.M. developed a profound anterograde amnesia, i.e., he had problems forming new memories. Particularly, he was not able to remember what happened during his days, but he could learn new motor skills (Milner et al., 1968). Thus, his declarative memory, i.e., memory about facts and events, seemed to have suffered profoundly, in contrast to his non-declarative memory.

Observing H.M. throughout his whole life, till he died in 2008, offered seminal insights into human memory formation. Specifically indicating that the hippocampus on its own can not be responsible for

1. all types of memories
2. one type of memory without any other helping brain structure (Eichenbaum et al., 1992).

Besides these observations, more precise research was conducted to unravel the functions of the HC as well as the process of memory formation.

Here, lesion studies in animals contributed significantly to this progress (Douglas, 1967). In contrast to studies with humans, in animal studies controlled lesions can be performed and it is possible to record from specific brain areas depending on the scientific questions one is interested in. Nowadays, memory formation and spatial cognition are assigned as major functions to the HC (Eichenbaum and Cohen, 2014). In doing so, the HC is thought to play a crucial role in the integration of different memories (Giovanello et al., 2009). Hereby, a certain flexibility within

the neural network is needed in order to link novel experiences to already gained ones. A typical learning paradigm to test this ability would be to learn to associate word pairs. The flexible expression of declarative memory could be shown in rats (Bunsey and Eichenbaum, 1996) and humans (Preston et al., 2004). The rats had to associate pairs of odors whereas humans were trained with pairs of faces and houses. The type of memory tested here is known as the flexible relational memory.

Another theory about the HC tackles its contribution in spatial learning and is called the cognitive map theory (O'Keefe and Nadel, 1978). The theory states that the HC builds an internal representation of the external environment which can be used, e.g., for navigation. The theory was kick-started by the discovery of the hippocampal place cells (O'Keefe and Dostrovsky, 1971). The firing of a place cell in an animal, in a predetermined maze, is highly correlated to the location of the animal. A detailed description of place cells can be found below.

The discovery of place cells was trend-stetting in the field of neuroscience, and subsequently John O'Keefe won the Nobel Prize for Physiology or Medicine in 2014. He shared the Nobel Prize with May-Britt and Edvard Moser who were in 2005 the first to describe a similar cell type in the entorhinal cortex, namely the grid cells (Hafting et al., 2005). In contrast to place cells, grid cells feature multiple firing fields in a more or less regular hexagonal fashion.

1.2.1 Hippocampal subregions

Together with its surrounding structures, the HC is part of the hippocampal formation (HF) (Amaral and Witter, 1989). The following areas belong to the HF: the entorhinal cortex (EC), pre- and parasubiculum, subiculum, and dentate gyrus (DG) (see Figure 1.1). There are various connections within this brain regions as well as projections to other areas which will be examined in the following.

The HC can be anatomically as well as functionally divided into different subfields. As mentioned above, they are labeled with the abbreviation CA followed by a number to distinguish the parts from each other.

Already in 1911, Cajal revealed, by looking at Golgi stainings and providing drawings, a significant portion of the underlying anatomical structure as well as projec-

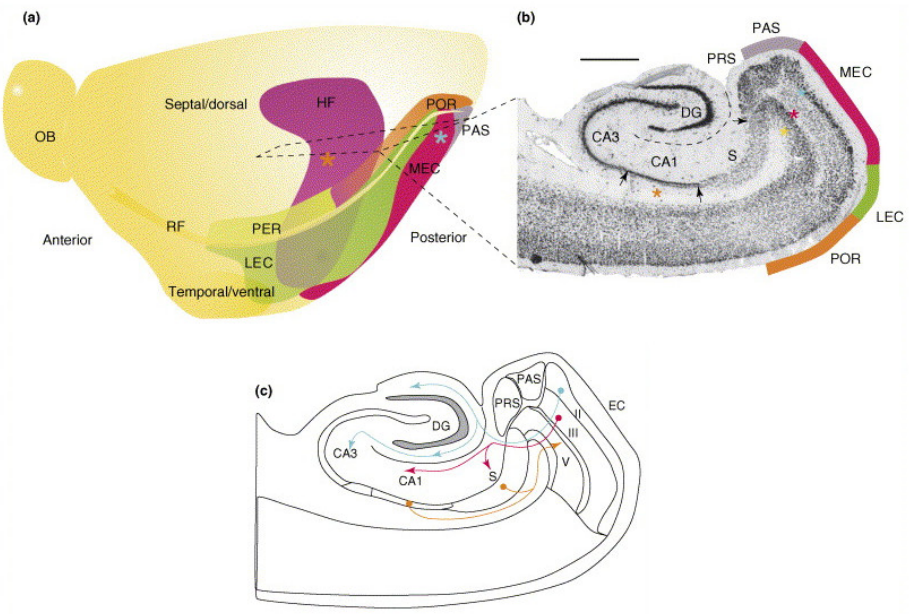

Figure 1.1: Rat brain from a posterolateral view. (a) Anterior part is characterized by the olfactory bulb (OB). In violet the HF is depicted with its neighboring regions. (b) Horizontal section through the HF. (c) Main synaptic connections in the HF. Adapted from Witter et al. (2000) with permission,

tions from and to different cell layers within the HF (Cajal, 1911). Some of which even got forgotten over the years and were found again later, like the projection from the EC to CA1 and CA3 (Witter et al., 2000; Steward and Scoville, 1976).

Layers. Each layer in the HC is characterized by the type of cell bodies as well as axonal and dendritic connections located in it. These distributions can already be seen in older drawings of hippocampal slices, as mentioned above. Additionally, electrophysiological *in vitro* or *in vivo* recordings reveal differences in the layers, as well as molecular analysis of it.

The HC is characterized by the following layers (see, e.g., Amaral et al. (2007) and Benson (2020) as references):

- Stratum lacunosum-moleculare
- Stratum radiatum
- Stratum lucidum
- Stratum pyramidale
- Stratum oriens

Stratum lacunosum-moleculare is the layer that is most superficial. In CA3, projections from EC layer II terminate in this layer. Below it, stratum radiatum can be found with septal and commissural axons. Stratum lucidum only appearce in CA3. It cannot be found in CA1 and CA2. Mossy fibers from DG terminate in stratum lucidum. Attached, stratum pyramidale is located, containing the cell bodies of the principal cell type in the HC, the excitatory pyramidal neurons (Freund and Buzsáki, 1998). Stratum oriens concludes the layers. It mainly contains cell somata of inhibitory neurons, like basket cells.
The variety of inhibitory interneurons is considerably higher than that of pyramidal cells (Klausberger and Somogyi, 2008). More than 20 have been found in the CA1, in contrast to a small single-digit number of types of pyramidal cells (Spruston, 2008). These inhibitory cells spread the entire area. Pyramidal neurons in the CA1 are packed in a denser fashion than those in CA3.
Overall, pyramidal neurons in CA1 and CA3 have very similar properties (Spruston, 2008). In contrast, pyramidal neurons found in the CA2 are more different, e.g., they possess a higher membrane capacitance, a lower input resistance, and are more hyperpolarized (Dudek et al., 2016). Furthermore, in CA2 no long-term potentiation seems possible (Dudek et al., 2016).
For the sake of completeness, the CA4 has to be mentioned. It is sometimes referred to as the hilar region when assigned to the DG (Amaral, 1978). Regarding the cells of CA4, which resemble more closely those in the DG than in other CA areas, the assignment to DG seems sensible (Blackstad, 1956). Beyond, CA4 is mainly mentioned in the context of schizophrenia (Falkai and Bogerts, 1986).

In patients with schizophrenia a loss in the volume of CA4 can be registered in comparison to healthy subjects (Haukvik et al., 2015).

1.2.2 Synaptic connections

Trisynaptic Circuit. In the classical view of hippocampal connections the focus lies on the trisynaptic loop (McNaughton and Morris, 1987). As its name implies, it consists of three synapses. Starting from layer II of the EC, neurons project via the perforant path to the DG. Here, granule cells are connected to the area CA3 via the mossy fibers. Finally, the CA3 pyramidal neurons show dense connections to pyramidal neurons in area CA1, called Schaffer collaterals. Area CA3 and DG exhibit many recurrent connections, in contrast to cells in CA1 (Lisman, 1999). Nevertheless, compared to primary sensory cortices, those recurrent connections are sparse (Miles et al., 2014).
The lamellar hypothesis which came up in the 1970s, suggested that the HC is organized in parallel lamellae (Andersen et al., 1971). This means that all the fibers have the same orientation in the three-dimensional space of the HC, i.e., transverse to the longitudinal axis. According to this theory, activation in a small portion of the EC would subsequently lead to a similar amount of activation in the underlying fiber connections. Thereby, parallel stacks of processing units would exist, with very little exchange across each other. The lamellar hypothesis sounded very plausible because it was in line with the anatomical organization of the HC. However, more modern tracing technologies, like anterograde tracers, finally disproved this (Amaral and Witter, 1989). Thereby, a much more diverse connectivity map could be revealed, including extensive connections also in the longitudinal axis.

Modern view. Although the trisynaptic loop builds a nice basis, e.g., for computational networks of the hippocampal area, as already indicated, ongoing work suggests a more complicated view (Lisman, 1999). First, it has to be mentioned that the trisynaptic loop can be bypassed via a direct connection between layer III of the EC to area CA1 (Van Hoesen et al., 1975). Moreover, the EC posses

direct projections to the subiculum (Witter et al., 1988). There is also a disynaptic loop from EC to CA3 and further on to CA1. Thus, it is possible to have specific information processing for different purposes, e.g., for pattern separation or completion (Jones and Mchugh, 2011). Pattern separation needs a sparse firing environment to give the possibility to activate different combinations of cells for different pattern. This environment can be found in the DG with its granule cells. In contrast to it, pattern completion is linked to the recurrent network of the pyramidal cells in area CA3.
At last, area CA2 has been disregarded for the most time and is getting only very recently more attention by analyzing, e.g., its gene expression or electrophysiological profile (Jones and Mchugh, 2011). Besides, it was shown that CA2 plays a crucial role in social memory formation (Hitti and Siegelbaum, 2014). The exact involvement of CA2 in hippocampal learning is still unclear. There is strong inhibition of the excitatory inputs from CA3 onto the pyramidal neurons in CA2. Thereby, actions potentials are suppressed in CA2 (Nasrallah et al., 2015). However, the generation of action potentials can be achieved by using high frequency distal inputs or induce long-term depression (Nasrallah et al., 2017).
Overall, it has to be mentioned that within the HF lots of parallel circuits exist (Witter et al., 2000). Here, the EC has to be mentioned as the gatekeeper of the HF providing the input as well as receiving the output.

1.2.3 Place cells

The HC is very important in spatial cognition, i.e, the navigation through different environments (see also Burgess et al. (2002)). In the HC, pyramidal neurons are the principal cell type. *In vivo* recordings of these neurons in area CA1 and CA3 of rodents reveal a very specific firing pattern in moving animals.
This particular type of experiment was first published by O'Keefe and Dostrovsky in 1971 (O'Keefe and Dostrovsky, 1971). They implanted electrodes into the HC of rats and placed the animals into a maze to freely explore the space. Later analysis of the data allowed them to report on locations of single cell activity, i.e., single action potentials of one specific cell. Mapping the activity of one cell onto the real maze revealed a high correlation between location and activity. Some

cells showed very distinct firing fields and generated with their activity a representation of the outside location. Based on this finding, these neurons were named place cells. Combining the information of several of these cells, allows to follow the trace of the animal through the environment by analyzing the cell's activity (Wilson and McNaughton, 1993). The easy decoding of place cells strengthens the idea of the HC playing a central role in forming a cognitive map (O'Keefe and Nadel, 1978).

Over the following years, because of their fascinating firing pattern, the study of place cells became more and more popular. Thus, recordings in various environments, from simple linear tracks (Lee and Wilson, 2002) up to mazes in virtual reality setups (Harvey et al., 2009), exist. Some of them had a fixed layout, others were flexible, e.g., in the location of walls or the appearance of visual cues. Often, these studies wanted to test the dependency of place cell firing with respect to cues from the outside world. Changes observed in the firing pattern of place cells are called remapping.

There are two kinds of remapping, rate remapping and global remapping (Leutgeb et al., 2005). In rate remapping changes in the environment affect only the firing rate of the place cells, but do not alter the position of the firing fields in the maze. In contrast, global remapping means a complete change of the firing field location of a place cell.

Recently, the firing profile of verified place cells was tested with respect to frequency of sound (Aronov et al., 2017). The question was whether the hippocampal-entorhinal system allows only the mapping of spatial cues or whether the circuit can be also used for non-spatial cues. Therefore, rats were trained to push a button as long as a presented pure tone reached a predetermined frequency. In fact, the authors could show that many cells preferably fired at one specific frequency of the sound. Thus, the authors reported that the hippocampal-entorhinal circuit is capable of processing various types of information by using similar mechanisms. Testing the circuit on sound frequency came from the idea to test the system on another continuous variable besides space.

Even the existence of social place cells in bats has been reported recently (Omer et al., 2018). Social place cells were defined as cells being active at locations of

an observed conspecific. To define social place cells, the firing activity of a place cell in the observer bat was mapped onto to movement trace of the watched conspecific. A similar experiment was performed in rats (Danjo et al., 2018).
To what extend the activity in the neurons of the observer represents a social place cell or planning of future movement is highly debated. The authors claim that future planning can be excluded as the fields do not vanish when sharp-wave ripples are disrupted in the observer, although they would be necessary for action planning (Omer et al., 2018).

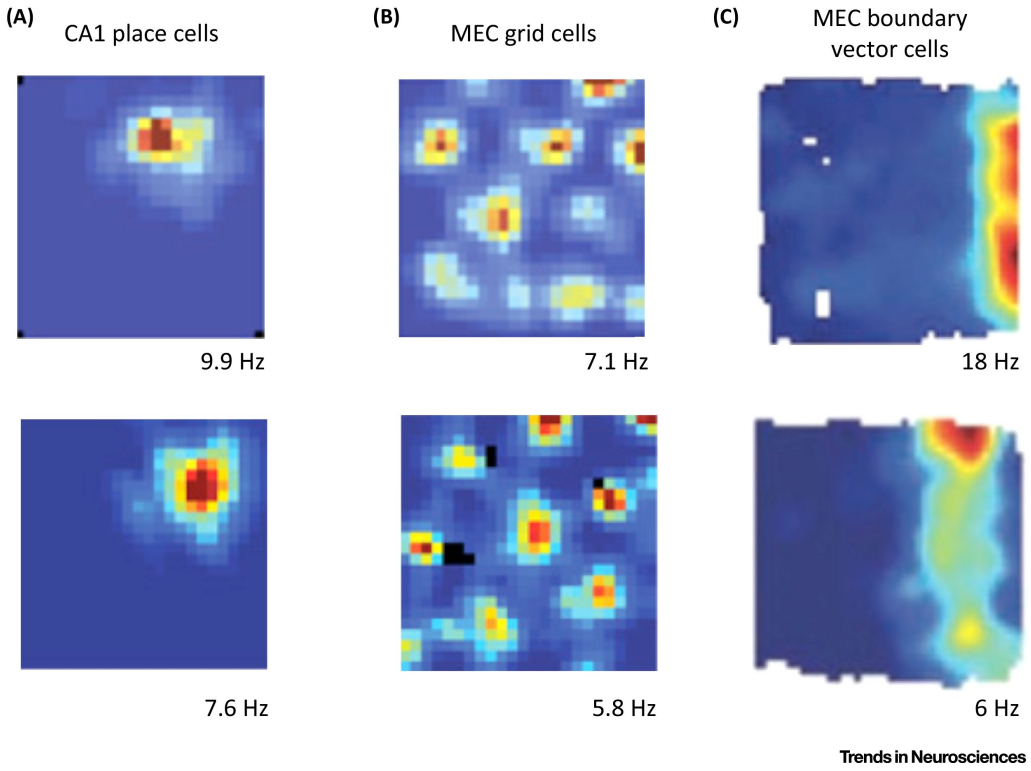

Figure 1.2: Rate maps of spatially organized cells in the HF. Blue colors indicate low firing rates, whereas red colors stand for high firing rates. The number below depicts the peak firing rates. (A) Place cells in the CA1. (B) Grid cells in the MEC. (C) Boundary vector cells in the MEC. Adapted from Sanders et al. (2015) with permission.

1.2.4 Other spatially organized cells in the HF

Additionally, to the spatially organized place cells in the HC, a variety of cells can be found in the EC and surrounding structures, which also exhibit location dependent firing patterns (see Figure 1.2).

As referred to before, in 2014 the Nobel Price was not only awarded to John O'Keefe for the discovery of place cells, but also to May-Britt and Edvard Moser for being the first to describe **grid cells** in the EC of rats (Fyhn et al., 2004; Hafting et al., 2005). In contrast to most of the place cells, grid cells posses several firing fields in one environment. These fields are not distributed randomly, but follow a very specific and highly interesting pattern. They are arranged in a hexagonal fashion. The single fields of these grids vary in size along the dorsal-ventral axis (Brun et al., 2008) and they come in various orientations. Together with place cells they form a distinct representation of the outside location which is easy to decode.

Another type of important cells, regarding the navigation through space, are **head-direction cells** (Taube et al., 1990a). As the name implies, firing of these cells depends on the direction of an animal's head on a horizontal plane. Very early on, it was clear that the firing largely dependent on the environment with its local and distal cues (Taube et al., 1990b). By changing these cues one can shift the preferred angle of a head-direction cell.

Sargolini et al. (2006) could show that in deeper layers of the medial EC conjunctive cells, exhibiting the properties of grid and head-direction cells, can be found. Additionally, the activity of these cells depends on the running speed of the animal, a property also reported in plain grid and head-direction cells. The convergence of information about direction, movement, and position within these conjunctive cells indicates a possible role of these neurons in updating the grid coordinates during exploration.

The next class of spatially dependent firing cells are **border cells** (Solstad et al., 2008). These neurons are located in the medial EC as well as the parasubiculum and fire with respect to geometric borders, e.g., the wall of a maze. Border cells become active when the animal is, e.g., close to the wall.

Furthermore, Lever et al. (2009) found **boundary vector cells** in the subiculum. The activity of these cells is determined by the distance to a boundary, with each cell having a peak firing rate at a different distance. Their existence has been predicted since 1996 to explain the expansion of a place field when an environment is stretched (O' Keefe and Burgess, 1996; Burgess and O'Keefe, 1996).

Recently, the finding of **speed cells** has been reported in the medial EC (Kropff et al., 2015). These neurons adapt their firing rate with respect to the running speed. Thus, they could serve as information source about the velocity of the animal for grid cells to adapt their firing rate.
The list of cells with spatial firing of spatially firing cells corresponds to the current view but might be incomplete. New cell types, like the social place cell or the sound dependent cells are described. To what extent these cell types can be in fact considered completely new types is a matter of debate. Hereby, the experimental protocols carefully need to be analyzed. Especially an expected reward has the tendency to increase firing in certain cells and thereby strongly influences the firing pattern.

1.2.5 Hippocampal oscillations

Depending on the current state of the brain, largely constrained by the behavior, different oscillations are particularly obvious in electroencephalography (EEG) or local field potential (LFP) recordings of the HC (Draguhn and Buzsaki, 2004). In general, local synchronous rhythms seem to be important to select inputs and provide plasticity in the underlying network (Draguhn and Buzsaki, 2004). Oscillations of different frequency bands often show close relationships to certain behavioural states. Comparing, e.g., the awake to the sleeping brain, reveals profound differences in the power spectrum.
In the context of memory formation, oscillations in the cortex are thought to provide time windows in which information transfer and storage is possible. This might be achieved, e.g., by synchronizing the phases of oscillations over different brain regions and thereby establishing precise spike timing.
Here, I want to give a short overview of the three prominent oscillations in the cortex. Each type is characterized by a frequency band which exact borders are highly debated among scientist. Thus, the given values below do not need to be seen as exact numbers but rather as a rough range of the respective frequency band for different oscillations in the HC.

Theta. An oscillation with a frequency between 8 to 10 Hz is called theta. Theta oscillations are highly prominent during locomotive behavior and rapid eye movement sleep (REM) (see Figure 1.3). In contrast, they are mainly absent during resting behavior and slow wave sleep (Jouvet, 1969). Interestingly, theta frequency exhibits a strong correlation with the running speed (Fuhrmann et al., 2015).

Different mechanisms seem to be able to generate theta, with pyramidal neurons being discharged in a synchronous fashion (Buzsáki et al., 1983). This, in turn, induces a synchronous discharge of interneurons, targeted by the pyramidal cells (Tóth and Freund, 1992).

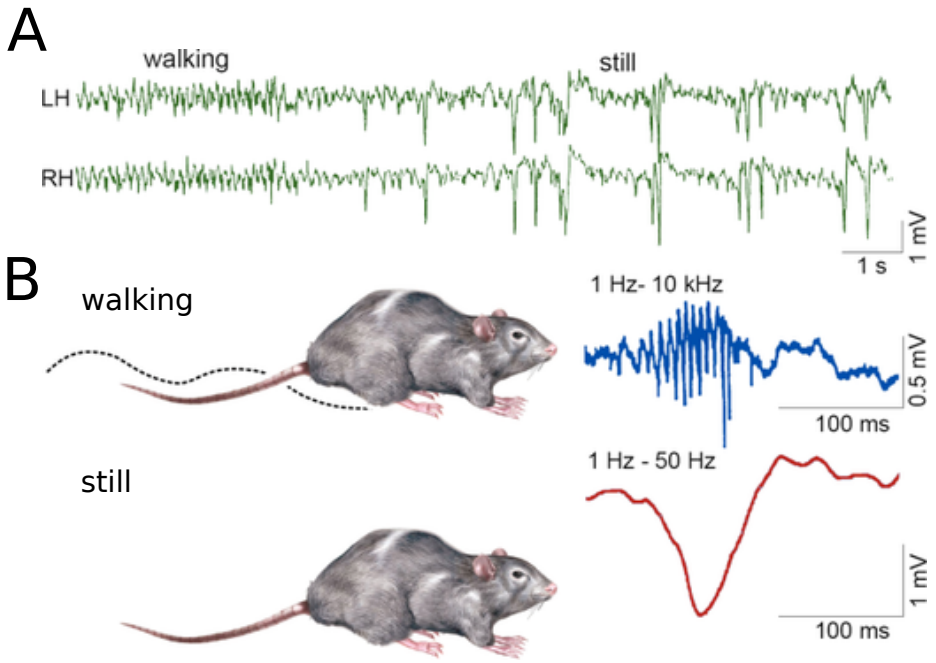

Figure 1.3: Hippocapal oscillations. Depending on the behavior of an animal, the LFP shows different oscillatory pattern. The figure shows the oscillatory differences in the hippocampus of a rat while it is moving or inactive (still). (A) The green curves show how the LFP changes over time when the behavior of an animal switches from moving (left side) to still (right side). The upper curve depicts the recording in the left hemisphere (LH) and the lower one in the right hemisphere (RH). (B) The upper rat is moving, while the lower one is still. Next to each rat characteristic voltage traces for the two behavioral states are shown, filtered in the frequencies indicated above. In case of a moving animal, theta oscillations are prominent (around 8 Hz). In resting behavior strong voltage deflections, sharp waves are apparent. Adapted from Buzsáki (2015) with permission.

Theta rhythm became particularly interesting when single spiking activity of pyramidal neurons in the HC were analyzed with respect to the phase of the oscillation. Skaggs et al. (1996) reported a shift in phase when passing through several cycles. Spikes appear earlier and earlier in phase. This phenomenon is called phase precession. During one theta cycle, only a minor fraction of CA1 pyramidal neurons is active (Csicsvari et al., 1998). They correspond to the place cells being active at the current location.
A link between theta and memory formation in rodents was already provided by Winson (1978). He disrupted hippocampal theta oscillations during a spatial learning task whereby the memory performance of the animals decreased. In humans, Backus et al. (2016) were the first to show electrophysiological evidence for the importance of hippocampal theta in the process of memory integration. They found a positive correlation between theta power during memory encoding and the later performance in memory recall.

Gamma. Gamma oscillations are faster than theta. They are often subdivided into fast gamma from 40 to 100 Hz and slow gamma from 25 to 50 Hz. Their amplitude is typically lower than the one of theta oscillations (Buzsáki et al., 1983). The two subtypes seem to have different origins. Whereas fast gamma is generated in medial EC, slow gamma originates in CA3 (Csicsvari et al., 2003). By varying the interplay between these rhythms it appears to be possible to guide information flow during memory formation through connection of specific cell assemblies (Colgin et al., 2009). In these processes precise timing is the key feature. Coordinated spike times might be enabled through synchronization to certain frequencies. Here, it is hypothesized that hippocampal theta plays an important role in the entrainment of gamma (Sirota et al., 2008).

Sharp-wave ripples. During slow-wave sleep and waking immobility, LFP recordings in the HC exhibit in a regular fashion high voltage deflections, sharp-waves (see Figure 1.3), accompanied by fast oscillation, ripples, in the range of 150 to 200 Hz. First described by Buzsáki et al. (1992), very early on, they were associated with memory consolidation.

As sharp-wave ripples (SWR) can be observed in detached hippocampal slices, the HC itself is a good candidate as their origin (Kubota, 2002). Even CA1 minisclices, with CA1 being detached from CA3, can exhibit SWRs (Maier et al., 2011).

Spikes of CA1 place cells show phase locking to ripples in CA1, which argues against an entrainment of CA1 firing by CA3 (Sullivan et al., 2011). But CA3 may still alter the firing properties of CA1 cells during ripples as it can be seen in replay. The phenomenon of replay is dealt with in greater detail the subsequent paragraph.

Before I explain the phenomenon of replay, I would like to go a bit more into detail about the relevance of SWR currents for memory consolidation. To test their importance, a straight-forward approach is to block SWRs during a sleep period directly following a spatial learning task (Girardeau et al., 2009, 2014). In this study, an online detection mechanism was used to filter SWR during the experiment by applying a threshold in the ripple frequency band. The detected SWR could be blocked by directly inserting an electric pulse. Girardeau et al. (2009) showed that rats with post-learning SWR blockage performed worse in the task than the control groups. They controlled for effects of the electrical pulse in general by testing unimplanted animals, as well as for the specificity of the stimulation by applying a pulse 80-120 ms after SWR detection. Both control groups exhibited a similar performance index, measuring the memory stability over several days after the learning task.

Jadhav et al. (2012) conducted a similar experiment. Instead of blocking SWR during post-learning sleep, they blocked SWR occurring in awake rats during the performance of a spatial alternation task. This also resulted in a performance loss.

A later study could identify NMDA receptors as an important component in increasing the SWR drive(Girardeau et al., 2014). Blocking NMDA receptors before training of a spatial learning task resulted in a lower performance of the tested animals. Those results suggest that the consolidation of spatial memories during sleep is regulated by processes that depend on NMDA receptors.

Together, these studies provide strong evidence for SWR playing a crucial role in

the process of memory consolidation.

The mechanisms behind SWR generation are still under debate and various models exist (Donoso et al., 2018). A major point of debate is the origin of SWR oscillations, i.e., do SWR originate from excitation, inhibition, or a combination of both (Draguhn et al., 1998; Memmesheimer, 2010; Ylinen et al., 1995; Stark et al., 2014).

In the case of models based on excitatory induced fast oscillations, pyramidal cells are thought to propagate their signals in a second stage to inhibitory interneurons. The two studies mentioned here, propse different ways of transmission. While Draguhn et al. (1998) suggested a signal transmission via axo-axonic gap-junctions, later Memmesheimer (2010) introduced the concept of supralinear dendritic interactions as a potential mechanism for these coherent oscillations.

In models that rely on inhibition as a source for SWR, the focus lies on recurrent networks of interneurons in area CA3 (Taxidis et al., 2012). These are assumed to generate fast oscillations which in a second step serve as pacemakers for pyramidal neurons in CA1. The transmission to CA1 could either happen via Schaffer collaterals (Csicsvari et al., 2000) or through activation of local pyramidal cells (Stark et al., 2014).

Replay. The term replay describes a specific pattern of the single cell spiking activity of pyramidal cells during SWR. As explained before, during free exploration of an environment, tracking the firing of place cells allows for reconstruction of the pathway the tested animal took. Wilson and McNaughton (1994) were the first to describe a correlation between the firing of these cells during exploration and their activity during resting. Namely, place cells firing together while the animal explored the environment, had the tendency to fire together during subsequent sleep sessions as well. To unravel this phenomenon, detailed multi-site recordings were necessary.

Later on, it was even shown that the relative firing order is preserved Lee and Wilson (2002). The replay during sleep is considered as a re-experience of the previous behavior and thereby as a strong hint that SWR are important in memory consolidation. Moreover, the faster timescale of replay fits the activity profile

of NMDA receptors which are important in spike-timing dependent plasticity (Girardeau et al., 2009).
Interestingly, analysis of single cell activity during short resting times directly after a running session shows reversed replay (Foster and Wilson, 2006). This could be considered to express immediate processing of a recent event.
Within 2d environments, a form of replay before a goal-directed behavior was described (Pfeiffer and Foster, 2013). Thus, replay seems to allow goal-directed movement, an essential part of spatial learning.

Models of ripple generation There are mainly three different types of models trying to explain the generation of ripple oscillations:

1. Axon-axon gap junctions between CA1 pyramidal neurons (Traub and Bibbig, 2000)
2. Solely rhythmic perisomatic inhibition (Pangalos et al., 2013)
3. Phasic inhibition and excitation (Maier et al., 2011).

Based on electrophysiological findings (Draguhn et al., 1998), Traub and Bibbig (2000) developed the idea of an axon-axon gap junction model for ripples. Draguhn et al. (1998) described gap junction dependent 200 Hz oscillations in hippocampal slices, which appeared spontaneously. Spikelets, somatic depolarizations with small amplitude, are thought to represent electrically coupled cells. Experiments could show a correlation between these spikelets and dye coupling of pyramidal cells (Perez-Velazquez et al., 1994). Schmitz et al. (2001) presented evidence in favor of an axonal connection between two pyramidal neurons. This connection would allow for a very fast information transfer between cells, as it is thought to happen during SWR.
The idea of spikelets being important in this process was strengthened by the finding that a strong contribution to place cell firing comes from spikelets (Epsztein et al., 2010).
In contrast, Pangalos et al. (2013) put their focus on perisomatic inhibition from oriens-lacunosum-moleculare (O-LM) interneurons. According to their *in vitro* recordings, O-LM neurons increase their firing during SWR due to excitatory

ripple-locked inputs. Thus, in contrast to previous findings, there is enough activity in O-LM neurons in order to have influence on the synaptic input into CA1 pyramidal neurons during SWR.
Maier et al. (2011) go even a step further and assume that not only inhibition is a key player, but also excitation. By using *in vitro* and *in vivo* recordings, they found evidence of a ripple modulated excitation.
There is still an ongoing debate about whether or not phasic excitation plays a crucial role and is present. Gan et al. (2017) argue against the presence of a phasic excitation. In contrast, Hulse et al. (2016) present findings pointing in the direction of a ripple generation that needs phasic excitation.

1.3 Learning and Memory

Learning is seen as the process of memory formation in order to store information which can be later restored. Classically, memory can be split into a declarative (explicit) and nondeclarative (implicit) form (Squire, 1992; Squire and Zola, 1996). In everyday life the use of the word memory is typically associated with the declarative type.

Declarative Memory. Declarative memory describes the capacity to remember events and facts (Cohen and Squire, 1980). Studies with amnesic patients, e.g., the famous patient H.M., revealed a tight connection between explicit memories and the medial temporal lobe structures. Thus, most studies concerned with learning in the HC try to use experimental settings such that the subject has to use its declarative memory.

Nondeclarative Memory. The term nondeclarative memory was established by Squire and Zola-Morgan (1988) to replace the term procedural memory as antagonist for declarative memory (Winograd, 1975). Thereby, it becomes a true opposite of declarative memory as it includes learning types that are not skill-based like classical conditioning. All of these nondeclarative memory abilities have an implicit information acquisition in common. Nevertheless, they include

a variety of learning and memory types and are, unlike the declarative memory, associated with multiple brain areas.

Furthermore, the division into short-term and long-term memory is widely used with short-term memory comprising memories lasting seconds to minutes. From a molecular perspective this classification is interesting, as long-term memory is dependent on protein synthesis, whereas short-term memory is not (Davis and Squire, 1984; Goelet et al., 1986). Thus long lasting memories can be affected by disruption of protein synthesis, whereas short-term memories cannot.

Memory Capacity. Memory capacity describes the amount of information that can be stored and successfully reproduced. Among other possible ways, behavioral events can be memorized as sequences of neuronal activity, e.g., as it is observable in the HC during replay of place cell activity (Pastalkova et al., 2008). Thus, the number of sequences that can be correctly replayed can be seen as a measurement for memory capacity.
Memory capacity is impacted by different factors (Leibold and Kempter, 2006). Those factors include the complexity of the sequence, i.e., its length, as well as the maximum amount of synaptic connections in the corresponding network. Longer sequences are harder to reproduce and more prone to mistakes. Increasing the number of synapses allows for more synaptic combinations. Consequently, higher connectivity increases the memory capacity of a network.

1.3.1 Learning in the Hippocampus

In 1989, Buzsáki proposed a ”two-stage model of memory formation”, comprising the following steps (Buzsáki, 1989):

1. Encoding
2. Consolidation.

The first stage is accompanied by theta oscillations, whereas the later one by ripple oscillations.
As explained before, memory consolidation is tightly linked to the phenomenon of

ripples in the HC and disruption of ripples in rodents results in impaired behavior in memory tasks. Memory consolidation describes the process of transferring a memory representation from its transitional place, e.g., the HC, to a place for long-term storage. The neocortex was proposed as a possible candidate for long-term memory. Especially associative cortices are known to be highly interconnected with temporal lobe structures like the HC. Additionally, cortical spindles, oscillations at 12 Hz which appear during non REM sleep, co occur with hippocampal ripples (Peyrache et al., 2011). Ripple oscillations were also found in the posterior parietal and midline cortex and were time wise correlated to hippocampal ripples (Khodagholy et al., 2017), thus, providing strong evidence for these cortical structures to be involved in memory consolidation.

Novel Object Recognition Tasks. To test nonspatial memory capacity in rodents novel object recognition tasks, developed by Ennaceur and Delacour (1988), are still very popular. In its original version, the time is measured an animal explores a familiar object in comparison to the time the animal spends with a new object. As rodents are curious animals they typically would spend more time with the unknown object.
In hippocampal lesion experiments after the training, the new object preference was reduced (Gaskin et al., 2003). This reduced novel object preference is seen as loss in the memory. The involvement of the HC could be shown with the help of hippocampal lesion experiments. Performing such lesions after training towards objects, the reduced new object preference was minimized in contrast to sham condition.

Spatial Learning Tasks. A very simple and elegant experimental paradigm to test spatial learning in rodents is the famous Morris water maze (Morris, 1981, 1984). Its setup is rather easy consisting in its basic version of a tank of milky water with a hidden platform the animal has to find (Vorhees and Williams, 2006). To orientate in space, distal cues, usually simply in form of the laboratory environment, are given. Learning is negatively correlated with the time the rodent needs to find the platform in repeating trials. By slight variations of the experimental

setup, e.g., removing or shifting the platform location, different forms of learning can be tested. Another neat advantage is the fact that no pretraining of the animals is required. Nevertheless, there is one big disadvantage, namely the water. Being no concern if one is interested in the rodents behavior, it becomes an issue when one wants to perform recordings in the brain. One possible workaround are virtual reality (VR) setups.
By using VR, the concept of the Morris water maze can now even be applied in humans and can be, e.g., combined with magnetoencephalographic recordings (Cornwell et al., 2008).
A common alternative to test spatial memory capabilities are radial arm mazes (Olton and Samuelson, 1976). Here, from a central platform, several linear tracks go off and the tested animal has to remember, with the help of distal cues, e.g. in which arm it already went in order to receive a reward.
Spatial learning tasks become even more interesting when considering associative memories. Meaningful events like fear or a reward situation can be associated with certain locations. The storage of these associations is linked with strengthening of synaptic connections (Hebb and Bussey, 1949). On this cellular level of learning, high frequency inputs can induce changes at the synapse, which are long lasting, known as long-term potentiation (LTP) (Bliss and Gardner-Medwin, 1973).

Learning on a synaptic level. The term long-term potentiation goes back to 1973 (Bliss and Gardner-Medwin, 1973). As already marked, LTP describes the strengthening of synaptic efficiency. It can be artificially induced by applying high frequency stimulation. It was first observed in the perforant path of the HC and has since then been described in a lot of other excitatory pathways.
The role of LTP, in the the context of learning in the HC, can be best investigated by disabling LTP during learning tasks. To do so, it is helpful to know that N-methyl-D-aspartate receptor (NMDAR) activation is crucial for the induction of a large part of LTP types (Collingridge et al., 1983). Thus, it is sufficient to block NMDAR in order to block at least these specific forms of LTP. The blocking can be achieved mainly with two different approaches.

On the one hand, there is the pharmacological approach, where a NMDAR antagonist is region specifically applied. On the other hand, one can use genetically modified mice to prevent the formation of NMDA receptors in defined brain areas. The difficulty with pharmacological NMDAR antagonists is their precise application, which is virtually not possible. Thus, any experimental outcome has to be interpreted with care.
Long-term depression (LTD) describes the opposite effect of LTP, namely lowering the effectiveness of synapses over a longer period of time (Bramham and Srebro, 1987). It can be induced by continuously applying a low frequency stimulus.

1.3.2 Computational single cell models

To study the computational properties of single neurons, a huge variety of models is available (for reference see, e.g. Abbott and Dayan (2001)). The selection ranges from stochastic models up to biophysically more realistic representations. Neurons can be described with one equation for the whole cell or a complex combination of thousands of differential equations. The complexity of the model should be chosen depending on the scientificquestions. Simple single cell models are a good choice when the focus lies on big neuronal networks. In contrast, highly detailed, biophysically inspired cell models are preferably selected when the focus lies on inner cell computations. Today, supercomputers allow scientists to built complex neuronal networks with detailed single neuron models. Nevertheless, simple models don't lose their right to exists. The fewer parameters used, the easier it is to interpret the results in a meaningful way.
The following section deals with models based on equations for membrane potential changes. In their ordinary form, a whole cell is regarded as one compartment, described by a single membrane voltage V_m. As input, these cell models receive electrical currents I.

Integrate-and-fire neuron The integrate-and-fire neuron is represented by the following equation

$$I(t) = C_m \frac{dV_m(t)}{dt}. \tag{1.1}$$

with C_m being the membrane capacitance. Membrane voltage changes are represented over the time. Additionally, a voltage threshold has to be set. When the this threshold is crossed a spike is elicited in the form of a delta function and the voltage returns to resting state.

Leaky integrate-and-fire neuron As the name implies, the leaky integrate-and fire neuron has an additional term for the membrane leakage I_{leak}. This current mimics the ion permeable membrane and thereby allowing the membrane voltage to return to equilibrium potential even when subthreshold inputs are applied. With the leak current the equation changes to

$$I(t) - I_{\text{leak}} = C_m \frac{dV_m(t)}{dt}, \tag{1.2}$$

with $I_{\text{leak}} = \frac{V_m(t)}{R_m}$.

Hodgkin-Huxley type model The Hodgkin-Huxley model extends the integrate-and-fire neuron with terms for different ion channels (Hodgkin and Huxley, 1952). In the classical version those are sodium, potassium, and a leakage current. As base the current is computed the following way

$$I_i = g_i(V_m - E_i). \tag{1.3}$$

Here, g_i denotes the conductance of channel i and E_i its reversal potential. The sum of sodium, potassium, and leak is represented by

$$I_m = g_{\text{leak}}(V - E_{\text{leak}}) + g_K n^4 (V - E_K) + m^3 h g_{Na}(V - E_{Na}). \tag{1.4}$$

The letters n, m, and h denote the gating variables, which describe the opening and closing dynamics of the channels with respect to membrane voltage changes. Those changes follow the equation

$$\frac{dn}{dt} = \alpha_n(V)(1 - n) - \beta_n(V)n, \tag{1.5}$$

where $\alpha_n(V)$ is the opening and $\beta_n(V)$ the closing rate. The formula can be rewritten as $\tau_n(V)\frac{dn}{dt} = n_\infty(V) - n$, with

$$\tau_n(V) = \frac{1}{\alpha_n(V) + \beta_n(V)} \tag{1.6}$$

and

$$n_\infty(V) = \frac{\alpha_n(V)}{\alpha_n(V) + \beta_n(V)}. \tag{1.7}$$

These two variables represent the time constant τ and the steady-state levels of activation and deactivation, respectively.

One way to enhance this model in order to get a biophysically more realistic neuron is by applying a complex geometrical layout. These models are then called multi-compartment models. In multi-compartment models, each geometrical unit has its own equation for the membrane voltage. This subdivision does not only allow to specify the surface area of specific parts of a neuron but also to individually adjust the type and amount of channels in this area. Geometrically, each compartment. To combine compartments resistive couplings are used.

1.3.3 Hebbian Learning

In order to achieve learning in neuronal networks, the cells within have to be flexible, i.e., they have to adapt their firing characteristics depending on the input from other cells.

The famous Hebb's rule tries to give a possible explanation on how synaptic plasticity can be achieved (Hebb and Bussey, 1949). It acts on the assumption of having two cells A and B that are close enough to be capable of exciting each other. The synaptic connection from neuron A to neuron B can be strengthened by repeatedly triggering action potentials in neuron B via activation of neuron A. In short, the postulate is often reduced to the sentence:

'Cells that fire together wire together'.

Learning is put on a level with stabilizing a specific firing pattern. The principle has been extended to loosing strength in the connections between neuron A and B if activation of neuron A frequently fails to excite neuron B . According to the principal: 'Use it or lose it'.

Nowadays, Hebbian learning is often used as term for correlation based learning rules in form of mathematical formulations (Gerstner and Kistler, 2002). Hence, it plays a major role in implementing artificial neural networks.

Artificial neural networks

One of the original neural network models for associative memory is the Willshaw model (Willshaw et al., 1969). The goal is to store a number of P memories, so called pattern.

The Willshaw model convinces by its very simple learning rule. The most simple version consists of two neuronal layers each with N excitatory neurons. The synaptic efficacy between two neurons is notated by J_{ji}, with j being the jth presynaptic neuron and i the ith postsynaptic neuron. If both cells are active in one presented pattern, J_{ji} is set to 1, otherwise it remains 0. Each memory can be represented by a vector V, for the first layer V_{i} with $i = 1, ..., N$, which leads to a synaptic matrix

$$J_{\text{ji}} = \Theta \sum_{\mu=1}^{p} V_{\text{i}}^{\mu} V_{\text{j}}^{\mu}. \tag{1.8}$$

Early versions of the model were limited to excitation, as the ability to store information was mainly assigned to excitatory synapses. When it became clear that inhibition cannot be neglected, the model was extended such that one synapse combines excitatory and inhibitory properties at the same time. Later addition of an independent inhibitory synapse enhanced the significance of the model (Golomb et al., 1990; Shim et al., 1991). Thereby, the model resembles more physiological findings.

The basic Willshaw model allows for all these adaptations and hence, is still an often used base for neural networks, especially in the context of sparse coding.

In general, artificial neural networks are a big field and recently, their popularity increased in the field of artificial intelligence and machine learning.

1.4 Sound localization

Localizing the source of a sound can be very crucial for the survival of an animal, e.g. in the case of a prey trying to avoid its predator. Thus, it might not be a surprise how precise this ability is in some species. Nevertheless, it is very impressive.
In particular, humans have to be mentioned. They can discriminate angular changes of sound source of around 1 degree (Blauert, 1970).
Physically, sound is nothing but a vibration generating a traveling pressure wave through a medium, e.g., the air or water. A sound wave is characterized through different parameters: amplitude, frequency, and speed. These parameters alter due to the distance a sound wave is traveling or changes in the medium it is traveling through.

Monaural Sound Localization. Already the sound arriving at one ear typically contains spatial information. Responsible for this is a combination of different effects. The ability that even one ear is capable of locating sounds was found very early on (Angell and Fite, 1901). In the 80s it was debated whether these monaural cues can only extract the elevation (Oldfield and Parker, 1986) or if they also add information to azimuth, the horizontal plane position (Butler, 1986). To gather directional information using just one ear seems to be an interplay between two things, spectral cues from the pinna and alterations through the head-shadow effect (Van Wanrooij, 2004). Whereas, healthy binaural subjects seem to disregard the head-shadow effect completely, for monaural listeners it appears to be a crucial input for sound localization.

Binaural Sound Localization. In humans, the two ears are located on opposite sides of the head, i.e., the distance between the ears resembles the width of the head. The easiest way to understand the impact of this arrangement, is to imagine a sound coming exactly from the right side of a human subject at the height of the ear. The sound will clearly arrive first at the right ear and then, with a time lag, at the left ear. This lag is known as interaural time difference, short ITD (see Figure 1.4). Additionally, the loudness of the sound is reduced at the

left ear, because of a higher distance to the sound source. The difference in loudness is called interaural level difference, ILD. Together, ITD and ILD provide good information about the direction a sound is coming from (Thompson, 1882).

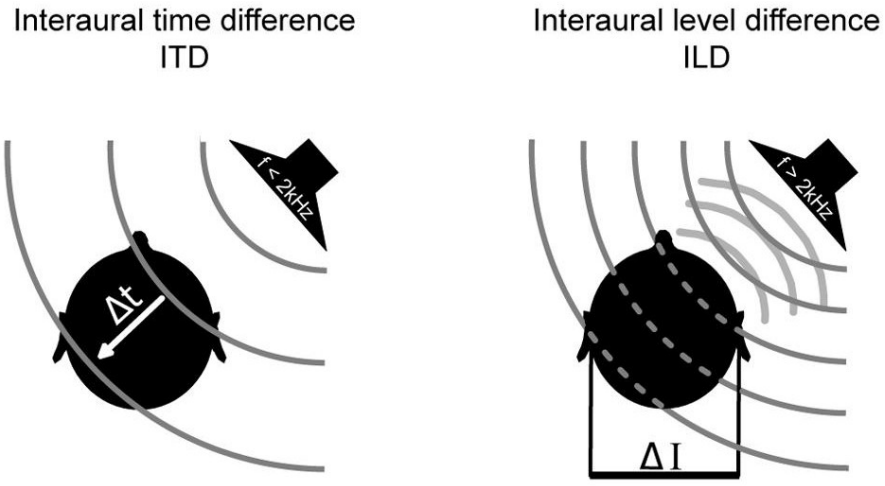

Figure 1.4: Cues for binaural hearing. Left side depicts interaural time differences, whereas on the right side interaural level differences are shown. Adapted from Grothe and Pecka (2014) with permission.

Changing the position of the sound source alters both, ITD and ILD. Shifting a sound source from the right side horizontally on a planar circle around the head towards the front, i.e., facing the nose of a subject, ITD and ILD are reduced until they are zero.

As already mentioned, humans are very accurate in determining the direction a sound is coming from. In the case of ITDs, they can discriminate up to 10 μs (Klumpp and Eady, 1956). For ILDs, changes in the range of 1 to 2 decibel can be detected (Middlebrooks and Green, 1991).

Whereas the minimal ITD is determined by the internal speed of processing the information in the brain, the maximum ITD is restricted by head size. For humans the maximum ITD is about 690 μs. Rodents have smaller values, e.g., the maximum ITD in gerbils is 120 μs (Maki and Furukawa, 2005). Gerbils are a very popular experimental animal in auditory research due to their hearing range (Ryan, 1976). With 0.1 to 60 kHz, their hearing range is comparable to the one in humans with 20 Hz to 20 kHz, especially for the lower frequencies.

It has to be noted that ILDs are particularly useful for high frequencies, whereas ITDs are mainly used for low frequency sound localization. A first to describe this separated paths and giving it the name duplex theory was Lord Raleigh in 1907 (Strutt (Lord Rayleigh), 1907).
It has been shown that gerbils also make use of ITDs localizing low frequency sounds (Heffner and Heffner, 1988). An additional point for their popularity in auditory neuroscience.

1.4.1 Auditory pathways

As mentioned above, it is very impressive how precise sound localization is in humans. Differences in microseconds can be detected. The brain is capable of doing so, despite the fact that the duration of an AP lies in millisecond range. To achieve these levels of accuracy, a high precision in processing is needed in the brain. For a detailed review on the following auditory pathways have a look at Grothe et al. (2010) and see Figure 1.5.
Interestingly, with the calyx of Held, the largest synapse found in the human brain, is part of the auditory pathway (Held, 1893). It was named after the anatomist Hans Held, who, with the help of Golgi stainings in the late 19th century, extensively studied the pathways underlying the auditory system (see Schneggenburger and Forsythe (2006) for a review). This very special synapse connects the anteroventral cochlear nucleus (AVCN) with the contralateral medial nucleus of the trapezoid body (MNTB), thereby taking care of a very accurate ILD processing.
In the **ILD** processing circuit, the lateral superior olive (LSO) is the first nucleus which is sensitive to ILDs (Cant and Casseday, 1986). At the ipsilateral side, there is a direct excitatory connection between spherical bushy cells (SBCs) in the cochlear nucleus (CN) and cells in the LSO (Ryugo and Sento, 1991). Inputs coming from the contralateral CN have to bypass two synapses. Globular bushy cells (GBCs) in the the contralateral CN project onto cells in the MNTB via the already mentioned calyx of Held (Harrison and Warr, 1962). This excitatory connection is afterwards converted into an inhibition from the MNTB to the LSO (Friauf and Ostwald, 1988). It is assumed that the calyx of Held plays a crucial

part in this switch from a very precise excitation to a very precise inhibition (Hermann et al., 2007).

LSO neurons send out inhibitory projections to the ipsilateral dorsal nucleus of the lateral lemniscus (DNLL) and inferior colliculus (IC) and excitatory projections to the contralateral DNLL and IC (Adams, 1979). The IC is the second nucleus at which ILD sensitivity is created (Park and Pollak, 1994). Next to the binaural inhibitory input from ipsilateral, it receives monaural excitatory input from the ipsilateral CN (Adams, 1979).

For this thesis more relevant is the pathway of **ITD** processing. Here, the important nucleus, to be mentioned, is the medial superior olive (MSO). As the MSO is very crucial for study 2, after discussing the ITD processing pathway, I will dedicate a more detailed paragraph to it below.

The very precise information transfer in the analysis of ITDs starts with the inner hair cells (IHC) in the cochlea (Galambos and Davis, 1943). Especially to low frequencies, these cells exhibit phase locking to the incoming wave form (Rose et al., 1967). The phase locking vanishes with increasing frequency, thereby limiting temporal information processing for high frequencies in this circuit.

Information flow continues from GBCs and SBCs in the CN. Ipsilateral and contralateral SBCs send direct excitatory projections onto the MSO (Chirila et al., 2007). GBCs also establish excitatory connections, which are converted into inhibitory connections onto the MSO. On the ipsilateral side, the change happens in the LNTB (Cant and Casseday, 1986), the contralateral projection switches to inhibition in the MNTB (Kuwabara and Zook, 1992). Thus, binaural excitatory and inhibitory inputs converge in the principal neurons of the MS0.

From MSO neurons the signal is further transmitted to the DNLL and IC. In contrast to LSO neurons, the MSO cells send out excitatory connections.

Furthermore, ITD processing is also possible in the LSO, when considering low frequency stimuli (Tollin, 2005).

1.4.2 Medial superior olive (MSO)

The MSO is a nucleus located in the auditory brain stem. Exactly like the HC, analyzing the structure of the MSO goes back to Cajal (Ramón y Cajal, 1909). Cajal

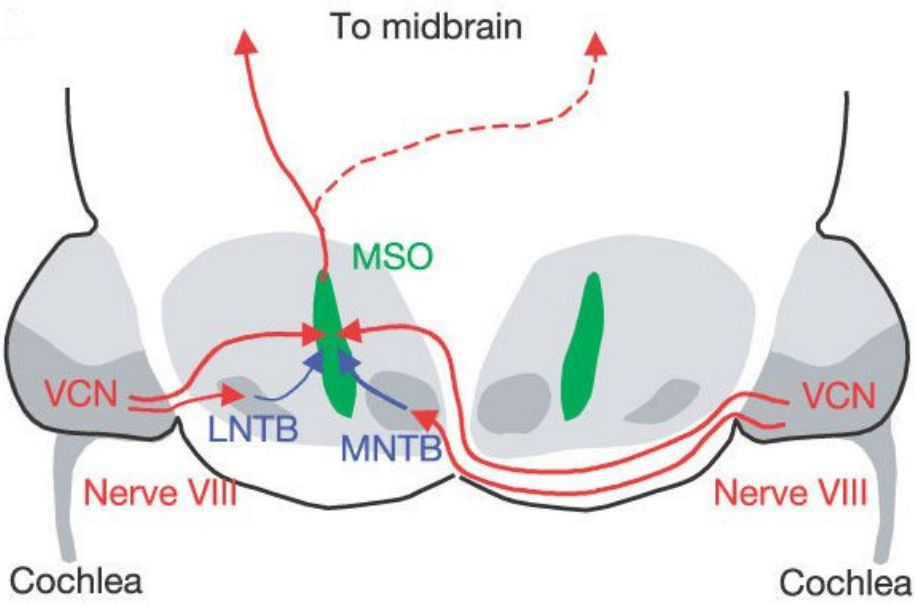

Figure 1.5: Projections from and to the medial superior olive (MSO) in a gerbil brain. Red arrows mark excitatory connections, whereas blue arrows depict inhibitory projections. The MSO receives in total 4 inputs. Contra- and ipsilateral ventral cochlear nuclei have direct excitatory projections onto the MSO. Inhibitory input arrives at the MSO via the lateral nucleus of the trapezoid body (LNTB) from ipsilateral and via the medial nucleus of the trapezoid body (MNTB) from contralateral. Both LNTB and MNTB convert exciation coming from the VCN into inhibition. The MSO targets the dorsal nucleus of the lateral lemniscus and the inferior colliculus with excitatory synapses (not shown). Adapted from Brand et al. (2002) with permission.

already proposed a possible role of the MSO in binaural hearing processing.
The MSO has a laminar structure and is organized from dorsal to ventral according to frequency tuning (Stotler, 1953). The dorsal part is tuned to low frequencies whereas the ventral part codes high frequencies (Guinan et al., 1972). The principal cells in the MSO receive mainly four inputs, which arrive at the individual cell at very distinct positions (Werthat et al., 2008). MSO neurons posses a very unique shape, with two major dendrites emerging from opposite sides of the cell (Kapfer et al., 2002). They are all arranged with the same orientation in para-saggital plane, giving the nucleus a very distinct look. Both ipsilateral and contralateral excitation and inhbition target each principal neuron. The excitatory inputs come from SBCs (Chirila et al., 2007). The ipsilateral excitation targets lateral dendrites,

the contralateral the medial dendrites. The inhibition comes ipsilaterally from the LNTB and contralaterally from the MNTB, both with a very fast transmission rate with little synaptic delay (Grothe and Sanes, 1993). Studies in gerbils show an almost exclusive targeting of inhibition onto the soma of MSO neurons (Kapfer et al., 2002).

It is known, that inputs coming from the MNTB provide very precise temporal information (Hermann et al., 2007). The exact interaction between the four inputs targeting one MSO neuron remains to be identified.

Although MSO neurons act as coincidence detectors, the tuning curves do not exhibit, as one might expect, peak firing at an ITD difference of 0 between the ipsi- and contralateral side. Rather there is a shift towards contra- or ipsilateral leading. This, on a first glance unexpected finding, provides helpful additional information, as explained later in the text.

The expectation of a peak firing rate at ITD 0 goes back to earlier research. Jeffress (1948) wrote a seminal paper on binaural hearing in the barn owl. His theory served for a long time as the model for ITD processing. The Jeffress model is based on an array of cells serving as coincidence detectors of sounds coming from both ears. The two ears supply a series of delay lines. Here, the peak firing rate of the neurons indeed arises at the time point at which the signals coming from the left and the right ear arrive at the same time. The transmission is achieved by excitatory connections only.

The simplicity of this model is quite striking and thus, it is no surprise that for a long period of time it was seen as the model for sound localization. Thus, it seemed likely that a similar mechanism was expected to be found in humans.

But as already mentioned, electrophysiological recordings suggest a different picture in mammals. Hereby, especially the finding of bilateral inhibitory inputs onto the MSO is crucial (Grothe and Sanes, 1993). Looking at experiments in gerbils where the glycinergic inhibition was blocked by inserting strychine, a glycine antagonist, it seems valid to assign an important role in ITD tuning to inhibition (Brand et al., 2002). By blocking inhibitory connections, the peak of the ITD function is moved in direction of 0 ITD, i.e., in direction of the physiological range.

Thus, under normal conditions, without blockage of inhibition, the peak lies outside

the physiological range. Initially, this finding sounds counterintuitive, but this view can be changed, when drawing the attention away from the peak to the steepest slope of the function. In contrast to the peak, the slope lies within the physiological range and could allow for a high acuity (Skottun, 1998). This theory includes the finding that the highest resolution of MSO neurons lies at a rather low variance firing rate.

Overall, there is still room for further discussion about the underlying processes and to what extent results from mammals can be applied to birds and vice versa. Hereby, it is crucial to consider the evolutionary point of view: Processing of auditory spatial stimuli evolved independently in mammals and birds (Grothe et al., 2004). Hence, it seems rather valid to assume different ways to process information on a neuronal level.

1.5 Thesis Aims

The thesis is divided into two separate studies with a following discussion. Both studies have in common the use of a biophysically inspired, compartmentalized neuronal model. Whereas the focus of study 1 lies on CA1 pyramidal neurons in the HC, study 2 is concerned with the integration properties of MSO neurons.

Study 1 - Pattern Separation During Sharp-Wave Ripples using Physiological Inputs

Sharp-wave ripple (SWR) oscillations can be recorded in the hippocampal LFP during slow-wave sleep and quiet wakefulness. They are composed of a high voltage deflection, paired with fast oscillations (ripples) in the range between around 150 to 200 Hz (Buzsáki et al., 1992). Studies identified a connection between SWR and memory consolidation (Girardeau et al., 2009; Jadhav et al., 2012). During the occurrence of SWR, CA1 pyramidal neurons exhibit temporally precise sparse firing (Wilson and McNaughton, 1994).

In the here presented study, the focus lies on these oscillations and on how cellular mechanisms help to overcome the noise to integrate the incoming signals in a meaningful way. Biophysically inspired pyramidal cell models were used.

The physiological inputs of the model are a distinctive feature of the model and used to test learning in a sparse recurrent network. These inputs are based on *in vitro* recordings in the area CA1 during the spontaneous appearance of SWR (Maier et al., 2011). Parameters obtained from recorded currents were used to recreate excitatory and inhibitory conductance traces that then served as our model inputs.

The first aim was to study the origin of the AP sequences that are observable during SWR. The second aim was to test the hypothesis that the sparse recurrent network in CA1 is sufficient to store and successfully recall sequences, despite high background activity.

Study 2 - Action Potential Generation in an Anatomically Constrained Model of Medial Superior Olive Axons

The principal neurons in the MSO are characterized by a distinct electrical property, namely a high membrane conductance (Ratté et al., 2013). This property should make it very hard for the neurons to generate APs. Nevertheless, it is known from *in vivo* recordings that MSO neurons can produce APs with high firings rates (Goldberg and Brown, 1969).

This leaky membrane of MSO neurons arises from a certain arrangement of ion channels, especially Kv1 and HCN channels. The distribution of the latter is assumed to be crucial for the cell to work as a coincidence detector (Svirskis et al., 2004).

The study is based on this observation and uses a mixture of computational modeling, *in vitro* recordings, and immunohistochemical stainings to analyze it.

Thus, the aim of this study was to analyze, how precise ITD coding can be achieved in MSO neurons during a high-conductance state causing a short membrane time constant. The study tried to provide insights on the impact of the distribution of ion channels across the membrane on the signal integration time. Additionally, the goal was to test the influence of varied input frequencies on the firing threshold of a MSO cell.

Overall, both studies share the aim to unravel the cellular mechanisms underlying the ability to perform temporally very precise computations in a high-conductance state.

2

Study 1: Pattern Separation During Sharp-Wave Ripples using Physiological Inputs

This work was done under the supervision of Christian Leibold (CL). Franziska Hellmundt (FH) and CL conceived and designed the research. FH wrote the code, carried out the simulations and analyzed the data. FH and CL discussed the results and wrote the manuscript.

Pattern Separation During Sharp-Wave Ripples using Physiological Inputs

Franziska Hellmundt, Christian Leibold*
Department Biology II, Ludwig-Maximilians-Universität München, Martinsried, Germany
Graduate School for Systemic Neurosciences Munich, Martinsried, Germany
*Bernstein Center for Computational Neuroscience Munich, Martinsried, Germany
author correspondence should be addressed to leibold@bio.lmu.de

September 21, 2020

Abstract

Sharp wave ripple (SWR) events are brief deflections of the local field potential in hippocampal area CA1 that are associated with high frequency "ripples" and they often coincide with recurring sequences of action potentials from the CA1 pyramidal cell population. The mechanistic underpinnings of these SWR-associated sequences are unclear, particularly since CA1 is known to have only little recurrent synaptic connectivity. Nevertheless, these recurrent synapses exist and SWR have also been found in isolated CA1 preparations in-vitro. In this paper, we evaluated the hypothesis that the sparse CA1 recurrent connectivity could indeed be implementing a recurrent associative network for storing sequences by stimulating model CA1 neurons with compound synaptic inputs recorded in an in-vitro model of the SWR state. Our simulations show that, while history effects across cycles are indeed weak, the memory capacity that can be reached assuming physiological sparseness levels are much too low to support the model of a recurrent sequence memory. We thus conclude that the sequences observed during CA1 SWR in vivo must either result from intrinsic stereotypical burst of hyperexcitability, or involve pattern associations via extrahippocampal loops.

Introduction

Hippocampal sharp-wave ripple (SWR) events are characterized by large amplitude deflections of the local field potential (LFP) in hippocampal stratum pyramidale (Buzsáki, 1986) that are accompanied by a transient burst of high frequency ($\sim$ 200 Hz) oscillations (Buzsaki et al., 1992). SWRs were classically thought to play a role in memory consolidation processes (Buzsaki, 1989, 2015), and more recently were shown to be involved in path planning (Jadhav et al., 2012). The latter interpretation is particularly tempting because of the coincidence of SWRs with fast replay of place-field sequences (Lee and Wilson, 2002; Gupta et al., 2010).

Furthermore, SWRs are generated intrinsically in the hippocampus (Sullivan et al., 2011; Maier et al., 2011; Oliva et al., 2016) and thus they may be population signatures of memory-related activity patterns. The physiological mechanisms underlying sequence replay during sharp waves are, however, unresolved. One potential explanation is that sequential activity is merely reflecting different levels of excitability such that highly excitable cells fire early in a CA3-evoked burst, whereas less excitable cells are activated towards the end (Taxidis et al., 2012; Stark et al., 2015). A second explanation could be that the sequential activity structure is actually encoded in the recurrent synaptic connections (Deuchars and Thomson, 1996; Maier et al., 2011) such that at each ripple cycle a different cell assembly is activated from the excitatory drive exerted by the assembly active in the previous ripple cycle either within (Deuchars and Thomson, 1996) our outside the hippocampus.

Mathematical models based on the second hypothesis are supported by the finding that ripple-locked excitation has been observed in CA1 pyramidal cells in vitro even in an isolated CA1 preparation (Maier et al., 2011). However, as yet those models have mostly been discussed in discrete time, where a time step is assumed to reflect one ripple cycle (Leibold and Kempter, 2006; Kammerer et al., 2013). Generalizations to continuous time (Jahnke et al., 2015) so far did not fully explore memory capacity of how many cycle-by-cycle transitions can be retrieved. In this paper, we are asking to which extent the simplifications made in time discrete models are justified by the biophysical constraints of a CA1 pyramidal cell simulated in continuous time, and how they would affect memory capacity. These simplifications particularly concern the cellular memory time scale: In order for a cell to decide on a cycle-by-cycle basis whether it should fire in one specific ripple cycle, its input to the previous cycles must have only little effect. Furthermore, we explore how the ripple-locked nature of inhibitory currents, and the resulting high-conductance state, would contribute to cycle-by-cycle memory retrieval.

Results

Validation of multi-compartment model

To assess the memory capacity of single ripple cycles in CA1 pyramidal neurons, we created a multicompartmental model of a CA1 pyramidal neuron consisting of a soma, and dendritic and axonal compartments. The model was fitted to yield typical input resistance,

resting potential and rheobase values (see Methods for details). Voltage responses of the model cell were simulated for synaptic conductance traces that were reconstructed from in-vitro slice recordings of CA1 pyramidal cells during sharp-wave ripples (Maier et al., 2011), where conductances were derived from double exponential fits (see Methods) of both excitatory and inhibitory compound postsynaptic currents (cPSC). Examples of such conductance trains are shown in Fig.1 A. In our model, inhibitory inputs were located at the soma, excitatory conductances at the dendritic compartment.

We first asked, how well the experimentally recorded synaptic inputs can drive action potentials in our model cell and found that using only the excitatory cPSCs give rise to spiking for 12 % of the recorded cPSCs (126 of 1051 cPSCs). We next intended to combine excitatory cPSCs with inhibitory cPSCs (in total we generated 2000 of those random stimulus combinations). However, as there are no simultaneous recordings of excitatory and inhibitory cPSCs, this required us to decide how cPSCs recorded in different experiments should be temporally aligned. The lack of simultaneous recordings of excitatory and inhibitory cPSCs was due to experimental limitations. To gain either signal, the corresponding other one needed to be blocked. To record excitatory cPSCs the holding potential was shifted towards the reversal potential of Cl^-. Inhibitory cPSCs were recorded by pharmacologically blocking GABAergic synaptic inputs at single-cell level. One possibility would be to align them with respect to the intracellular current recording, more specifically using the fitted onset time of the cPSC (Fig.1 B top), the other possibility was to align inputs with respect to the extracellular recording, i.e., the sharp wave (SPW) peak (Fig.1 B bottom). Comparison of the intracellular cPSC Hilbert-phase distributions between the two alignment methods reveals that, while the intracellular alignment, not surprisingly, results in a better phase coordination in the first few cycles, the SPW peak alignment allows for phase coupling over larger number of cycles. Since we intended to study action potential generation over the whole extent of the SPW, we used the SPW peak as the alignment criterion in what follows. Again measuring the percentage of trials with action potentials, this time with SPW peak aligned excitatory and inhibitory inputs, we obtained an almost unchanged fraction of 11% action potential-eliciting stimuli (229 of 2000). However, the percentage of about 11% active neurons is sparser than the firing of CA1 pyramidal cells during SWRs in-vivo (Csicsvari et al., 1999, 2000). This suggests that a) pyramidal cells in-vivo are more easily excited than in-vitro and b) inhibition seems to only have limited effects on the overall spike output but could rather affect the temporal organization of AP firing. Potentially, the reduced fraction of APs in-vitro could be also explained by less current inputs due to cutting synaptic connection in the slices, although the 200 Hz ripples are very similar to ripples recorded in-vivo (Buzsáki, 1986). To test the latter hypothesis we computed spike phases of our model outputs, and found that indeed the action potentials only significantly lock to the ripple oscillation if inhibitory and excitatory cPSCs are combined (Fig. 1D). The firing phase of about 300 degrees is consistent with in-vivo reports (Csicsvari et al., 1999, note that phase zero is set ripple peak with our Method, whereas phase zero corresponds to ripple troughs there). Moreover, phase-locking also sensitively depends on the overall excitability of the neuron, since adding an additional depolarizing current injection increases spiking probability but removes significant phase locking at both conditions (with and without inhibition; Figure 1E).

Hence, our model of a CA1 pyramidal neuron exhibits sparse firing on physiological SWR inputs with phase-locking critically depending on the sparse activation and the presence of inhibitory conductances.

History dependence of spike timing

As a next question, we asked how independent the neuron can process the inputs it receives in subsequent ripple cycles and thus can function as a pattern associator on a cycle-by-cycle basis.

To this end, the reconstructed cPSCs were modified such that spiking of the neuron could be controlled at a specific ripple cycle. Therefore, we picked one cycle, e.g. cycle 0 (see Fig. 2 A), and removed the PSCs from this specific cycle to replace them by a single mean PSC for which we could freely vary the amplitude. These mean PSCs were constructed from double exponential fits (see Maier et al., 2011) using the mean rise and decay times from the recorded excitatory PSCs. The amplitude of this 'artificial' PSC was then increased until our model generated an action potential.

Figures 2 B to E depict the relationship between the minimal amplitude of the inserted PSC that elicited a spike and the amplitude of the experimentally measured excitatory PSC at the preceding cycle. For pure excitatory inputs, we would expect a negative relationship, such that excitation from preceding cycles reduces the needed amplitude in the following cycle to elicit an AP. To test for effects of cycle number, we removed and replaced PSCs at different ripple cycles from -2 to +1, with cycle 0 determined by the SWR maximum. Left columns show the results for purely excitatory inputs, whereas for the right column excitation was combined with a randomly picked inhibitory cPSC as described for Figure 1.

Only in the case of removing PSCs at cycle -2 a significant, but small negative relationship can be seen (see Figure 2 B and C, p values from Pearson's correlation). In the other cases, a small but not significant negative trend remains and the values for the amplitude of the inserted PSC cluster at about 780 pA (see Figure 2 D and E; conductance amplitudes are obtained by normalizing with the excitatory driving force of -70 mV). This amplitude corresponds to the amplitude needed to elicit an AP with a single PSC (with mean shape). When pairing the adapted excitatory cPSCs with unaltered inhibitory cPSCs, results are qualitatively similar except that there is even a slight positive trend observable when PSCs are modified at cycle 0.

Thus, the influence from preceding cycles on spike timing in the following cycles is very small, if at all present, but appears to be more pronounced in earlier ripple cycles than in later ones. This suggests that the physiological conductance traces used to stimulate our neuron model were typically low amplitude and thus hardly carried over to the next ripple cycle. Most of the cPSCs thus seemed to act as a noise background, that, in the next section, will be interpreted as the result of interference from multiple stored associations.

Pattern associations

Since the history dependence of spike timing was rather weak, we suspected that each ripple cycle might be treated as an individual time step for pattern association. We therefore aimed at quantifying the memory capacity of a ripple cycle.

To this end, we created input patterns (Fig. 3A) assuming that cPSCs arise from a sparse combination of 10,000 synaptic sites. To standardize the input cPSCs we fixed the number of ripple cycles to 7 and the cycle duration to 5 ms. During each cycle every synapse could be active or inactive, with the ratio of active to inactive synapses determined by the coding ratio f; the coding ratio can hence be interpreted as the population sparseness during a ripple cycle. In all synthetic cPSCs we used the 4th cycle to contain the random signal pattern to which the neuron should elicit an action potential, whereas the others cycles were containing random noise patterns to which the neurons should remain silent. Signal patterns differed from noise patterns only in that the synaptic weights were tuned to the signal pattern using Willshaw's learning rule (Willshaw et al., 1969): A synaptic weight was set to a standard conductance value (see Methods) if the synapse is active in at least one of P random signal patterns, otherwise it remains zero.

To quantify the success of memory retrieval, we used the retrieval quality measure

$$\Gamma = \text{fraction of hits} - \text{fraction of false alarms}$$

from (Leibold and Kempter, 2006). Since we probed the neuron with P cPSCs (each of which contained a different signal pattern in cycle 4) this measure amounts to

$$\Gamma = \frac{m}{P} - \frac{n}{6\,P}\ ,$$

where m and n count the number of action potentials in the signal cycle and the noise cycles, respectively.

Our simulations show that the retrieval quality only obtains positive values for a large number P of stored patterns if the inputs are very sparse (coding ratios below 1%); Figure 3A. For denser codes the capacity is limited to about 10 patterns. Adding inhibition does not improve storage capacity bur rather degrades it.

From these findings one may conclude that there is a necessity for sparse inputs. However, the idea of a cycle-by-cycle association additionally requires that the sparseness is similar in all ripple cycles, because the output in one cycle should be the input in the next cycle. Our simulations show that such a self-consistency in firing rate can, if at all, only be obtained for very low pattern numbers and coding ratio of about 0.04, which, assuming 7 ripple cycles, corresponds to sparseness values of about $7 \times 0.04 \approx 0.3$ per sharp-wave, which indeed comes close to what is reported from in-vivo experiments (Csicsvari et al., 2000).

Thus, to be consistent with in-vivo firing rates a cycle-by-cycle pattern association would only have a limited capacity of about ten patterns and thus would not be useful as a sequence memory, at least not if it was implemented by recurrent CA1 synapses (reported to realize a connectivity probability of 1% in Deuchars and Thomson, 1996). A potential problem for the validity of this conclusion could, however, arise from the neuron being modeled according to in-vitro measurements not reflecting the excitability and

synaptic drive CA1 pyramidal cells experience in-vivo. We therefore next repeated capacity measurements in a simpler neuron model which allows us to set an optimal firing threshold.

Pattern associations in leaky integrator neurons

In order to be able to control different spiking thresholds in a controlled manner, we implemented a single compartment leaky-integrate and fire neuron (LIF). Again the neuron was driven by 10,000 synapses, representing the potential input from other CA1 cells, during ripple oscillations. The resulting conductance trains were constructed identically as in Figure 3A. We now simulated multiple variants of the neuron model for a whole range of firing thresholds between -20 mV and -10 mV. For high thresholds the output rate was lower than the input rate (coding ratio), for low thresholds the output rate was higher than f (Figure 4B), such that for each input coding ratio there was a threshold with equal input and output rate (black line Figure 4C). This threshold was then used for capacity calculations for a recurrent regime in which activity in each cycle triggers the activity in the next cycle.

For only excitatory cPSCs (Figure 5D) positive retrieval quality can again only be achieved for sparse ($f < 1\%$) inputs, ruling out cycle-by-cycle retrieval for physiological sparseness values. However, after including inhibition we observe positive but small Γ values for large number of patterns even for physiological sparseness (Figure 5D). Thus adaptive threshold mechanisms could restore a high capacity in the presence of inhibition, but only at low signal-to-noise ratios. It is therefore questionable whether such a recurrent sequence memory is realized in CA1 (see Discussion).

Discussion

Based on physiologically recorded synaptic currents during sharp-wave ripple states in-vitro, this manuscript evaluates the capacity of a putatively recurrently connected CA1 network for sequence memory. Our results show that physiological sparseness values of about 30% (Csicsvari et al., 2000) per sharp wave (corresponding to about 4% per ripple cycle) are only consistent with the recurrent CA1 network hypothesis if ripple-locked excitatory and inhibitory currents are injected simultaneously, if the firing threshold is adaptable, and if low signal-to-noise ratios are sufficient.

Threshold adaptations of pyramidal cells have been shown to occur by both homeostatic changes in cellular excitability and synaptic strength (Burrone et al., 2002; Turrigiano, 2017). As a consequence the adapted threshold in slice recordings during the SWR state could thus indeed reflect the adapted threshold state for situations with of only few stereotypical patterns being repeated (Reichinnek et al., 2012). The adaptive threshold mechanism is needed because slight changes in the threshold lead to a different integration of inputs (Kempter et al., 1998). Only at an optimal threshold value the cell can function as coincidence detector.

To derive storage capacity from single neuron firing behavior, we made fundamental simplifications. First, we assessed sequence replay by the retrieval quality measure which

compares hit and false alarm rates. Such an approach of course would not work in a recurrent setting with entirely independent activity patterns, it rather assumes that the false alarm activation in one cycle contribute to the signal input in the next cycle. However, there is no physiological evidence that activity patterns in different cycles of a single SWR are independent. Thus, our model could still be consistent with recurring sequence motifs (Chenani et al., 2019). Here, the starting pattern defines the specific evolution of sequential activation without the ability to rewire associations between patterns within sequences. Second, the input cPSCs used in our model are derived from in-vitro recordings and it is unclear how well they reflect the in-vivo situation. Indeed (Gan et al., 2017) reported that ripple locked excitation cannot be identified in intracellular recordings in-vivo. The difference between the in-vivo and the in-vitro situation maybe reflecting overall homeostatic excitability increase. Particularly our simulations with added DC currents (Figure 1) show that increased excitability may shadow ripple locking of action potentials and hence that of recurrent EPSCs. Third, inhibitory and excitatory cPSCs cannot be recorded simultaneously from the same cell. We therefore randomly combined excitatory and inhibitory inputs, which disregards the possibility that at the single neuron level both inputs could have a higher degree of temporal coordination eventually leading to a better signal to noise ratio. However, the high postsynaptic connectivity (out degree) (Bezaire and Soltesz, 2013) of inhibitory neurons (particularly parvalbumin positive basket cells) argues in favor of a relatively similar inhibitory signals at all pyramidal cells and therefore such increases in signal-to noise ratio may be small.

Combining the results of our modeling and the limitations listed above, we can conclude that it is rather unlikely that at least under in-vivo conditions the recurrent CA1 network stores a large number of sequences of activity patterns. Since CA1 recordings, nevertheless show an extremely rich reservoir of sequences (Nadasdy et al., 1999; Liu et al., 2018; Chenani et al., 2019) their underlying mechanisms must be different from simple recurrence. There are two most likely alternatives. First, as already eluded to in the introduction, sequences may be generated by an excitability bias (Taxidis et al., 2012; Stark et al., 2015), where more excitably neurons in a pattern tend to fire first. Secondly, sequences may be generated by extrahippocampal recurrent loops. Such a mechanism would solve the independence problem of the noise patterns since consecutive feedforward layers would be able to filter out false alarm activations (Reyes, 2003). Moreover, experimental evidence showing spike timing alterations following medial entorhinal cortex lesions (Schlesiger et al., 2015) and dentate gyrus lesions (Sasaki et al., 2018) are also consistent with this latter idea.

Methods

Fitting of composed postsynaptic currents

The parameters used to reconstruct the post-synaptic currents (PSCs) were received from in-vitro recordings in hippocampal slices (Maier et al., 2011). The conductance of a single

PSC was modeled as follows:

$$I(t) = I_0\,\Theta(t - t_0)\left[\exp\left(\frac{t - t_0}{\tau_d}\right) - \exp\left(-\frac{t - t_0}{\tau_r}\right)\right] \tag{1}$$

with the Heaviside step function $\Theta(t) = 0$ for $t < 0$ and $\Theta(t) = 1$ otherwise. The current $I_0 = A\,N$ is the product of the peak amplitude A of the PSC and normalization factor

$$N = \left(\frac{\tau_r}{\tau_d}\right)^{\frac{\tau_r}{(\tau_d - \tau_r)}} - \left(\frac{\tau_r}{\tau_d}\right)^{\frac{\tau_d}{(\tau_r - \tau_d)}}. \tag{2}$$

Here, τ_r and τ_d denote the rise and decay time, with average values of $\tau_r = 1.7 \pm 0.04$ ms and $\tau_d = 4.04 \pm 0.08$ ms.
Combining several of these PSCs, resembles a compound post-synaptic current (cPSC). The data, collected in the in-vitro recordings, includes 1051 excitatory and 814 inhibitory cPSCs. Currents were transformed into conductances by dividing by the 70 mV which is approximately the driving force used in the experimental recordings.

Extracellular ripple cycles

In order to perform a cycle specific analysis, extracellular ripple cycles had to be mapped onto the intracellular signals. Therefore, the extracellular voltage signal was filtered in the ripple band (120 Hz to 300 Hz) and phases were obtained using a Hilbert transform of the filtered signal. Ripple cycles were subsequently identified as framed by the time points with Hilbert phase zero.

Single-compartment model

To gain control over the firing thresholds, we implemented a single-compartment leaky-integrate-and-fire model of a CA1 pyramidal neuron. The cell is modeled as one single compartment with one membrane voltage V governed by the differential equation

$$c_\mathrm{m}\frac{dV}{dt} = -I_\mathrm{m}, \tag{3}$$

with capacitance $c_\mathrm{m} = 100$ pF and $I_\mathrm{m} = I_\mathrm{leak} + I_\mathrm{exc} + I_\mathrm{inh}$. All currents are modeled as Ohmic,

$$I = g_\mathrm{i}\,(V - E_i), \tag{4}$$

with i being one specific channel type with its corresponding conductance g_i and reversal potential E_i.

The leak current I_{leak} has a conductance $g_\mathrm{leak} = \frac{1}{r}$, with r being the membrane resistance set to $r = 50$ MOhm. The resting potential was set by $V_\mathrm{rest} = E_\mathrm{leak} = -70$ mV, the excitatory and inhibitory reversal potentials were taken to be $E_\mathrm{exc} = -6.5$ mV and $E_\mathrm{inh} = -66$ mV. Additionally, the model contained a refractory time of $\tau = 5$ ms. The firing threshold was a free parameter.

Parameter	Value (μm)
$\text{Radius}_{\text{Dendrite}}$	2.5
$\text{Length}_{\text{Dendrite}}$	200
Radius_{ad}	2
Length_{ad}	7
$\text{Radius}_{\text{AIS}}$	0.5
$\text{Length}_{\text{AIS}}$	50
$\text{Radius}_{\text{Node}}$	0.5
$\text{Length}_{\text{Node}}$	1
$\text{Radius}_{\text{Internode}}$	0.75
$\text{Length}_{\text{Internode}}$	100

Table 1. Geometry of multicompartmental neuron model

Multi-compartment model

The choice for the geometry of our multi-compartment model of a CA1 pyramidal neuron was motivated by Thome et al. (2014). One of their findings was that axons of CA1 pyramidal neurons often emerge from dendrites. Thus, we took this observation and created a model neuron containing two dendritic compartments. One dendrite is directly attached to the soma, whereas the other one is connected via a small axo-dendritic compartment *ad*. From this small unit, the second dendrite as well as the axon branch off. The axon consists of an axon initial segment (AIS) following 8 axonal segments, subdivided into node and internode segments. Inhibitory synaptic inputs target the soma, excitatory synapses target the the axon-carrying dendrite. For the dendritic and axonal morphology we used the values summarized in Table 1.

The geometry of the soma was indirectly determined by fixing the capacity of the whole cell to 150 pF. The voltage was implemented as a Hodgkin–Huxley-type equation

$$c_{\text{m}}\frac{dV}{dt} = -(I_{\text{lk}} + I_{\text{Nav1.2}} + I_{\text{Nav1.6}} + I_{\text{Kv1}} + I_{\text{Kht}} + I_{\text{axial}} + I_{\text{syn}}) \ . \tag{5}$$

The transmembrane currents were modeled as Ohmic

$$I_x(V) = g_x a_x^m b_x^n (V - E_x), \tag{6}$$

with E_x denoting the reversal potential of channel x, g_x denoting the maximal conductance, a, and b are the gating variables and m,and n their cooperativities. Reversal potentials were set to $E_{leak} = -60\text{mV}$, $E_{Na} = 60\text{mV}$, $E_K = -80\text{mV}$.
Axial currents between the ith compartment and its surrounding compartments are calculated as follows:

$$I^i_{axial} = \frac{V_{i-1} - V_i}{R^{i-1,1}_{ax}} + \frac{V_{i+1} - V_i}{R^{i+1,1}_{ax}}, \tag{7}$$

with the axial resistances R_{ax} follow from the geometry and the specific length resistance of $\rho = 150$ Ohm cm.

Our choice of sodium channels was inspired by Hu et al. (2009). We thus inserted two different types of sodium channels Nav1.2 and Nav1.6. Additionally, we also implemented two potassium channels, one standard high-threshold channel (Mainen and Sejnowski, 1996) and a voltage-gated channel Shu et al. (2007).

The channel peak conductances are summarized in table 2. The leak conductance was

	Soma	**Dendrite**	**AIS**	**Node**	**Internode**
Nav1.2	11.28	0.008	2.0	0.0	0.0
Nav1.6	0.08	0.008	0.75	0.1	0.0
Kv1	0.40	0.0	1.0	0.005	0.0
Kht	0.0	0.002	0.2	0.0	0.0

Table 2. Channel densities in $\mathrm{nS}/\mu m^2$

set to $0.000095\mathrm{nS}/\mu m^2$ to account for resting potential of -71 mV and an input resistance of 14 MOhm. The rheobase current of the model is 780 pA.

The synaptic currents I_{syn} were calculated as for the single compartment model.

Setting the synaptic weights

The coding ratio f determines the percentage of active presynaptic cells during one ripple cycle. The exact distribution of active neurons is randomly assigned for each cycle individually. Noise and signal cycles share the same probability of active cells. In contrast, setting of the synaptic weights is solely determined by neurons being active during a signal cycles. We applied Willshaw's (clipped Hebbian) learning rule, which means that a synapse can be either on or off (Willshaw et al., 1969). Whenever a synapse is active in one of the signal cycles P, the synapse is set on all other synapses remain off. As value for the active synaptic weights, we chose a standard conductance of 0.84 nS divided by the number of active synapses. The standard conductance corresponds to the peak of a single, mean PSC which is sufficient to elicit a spike in our model.

References

Bezaire, M. J. and Soltesz, I. (2013). Quantitative assessment of CA1 local circuits: knowledge base for interneuron-pyramidal cell connectivity. *Hippocampus*, 23(9):751–785.

Burrone, J., O'Byrne, M., and Murthy, V. N. (2002). Multiple forms of synaptic plasticity triggered by selective suppression of activity in individual neurons. *Nature*, 420(6914):414–418.

Buzsáki, G. (1986). Hippocampal sharp waves: their origin and significance. *Brain research*, 398(2):242–252.

Buzsaki, G. (1989). Two-stage model of memory trace formation: a role for "noisy" brain states. *Neuroscience*, 31(3):551–570.

Buzsaki, G. (2015). Hippocampal sharp wave-ripple: A cognitive biomarker for episodic memory and planning. *Hippocampus*, 25(10):1073–1188.

Buzsaki, G., Horvath, Z., Urioste, R., Hetke, J., and Wise, K. (1992). High-frequency network oscillation in the hippocampus. *Science*, 256(5059):1025–1027.

Chenani, A., Sabariego, M., Schlesiger, M. I., Leutgeb, J. K., Leutgeb, S., and Leibold, C. (2019). Hippocampal CA1 replay becomes less prominent but more rigid without inputs from medial entorhinal cortex. *Nat Commun*, 10(1):1341.

Csicsvari, J., Hirase, H., Czurko, A., Mamiya, A., and Buzsaki, G. (1999). Fast network oscillations in the hippocampal CA1 region of the behaving rat. *J. Neurosci.*, 19(16):RC20.

Csicsvari, J., Hirase, H., Mamiya, A., and Buzsaki, G. (2000). Ensemble patterns of hippocampal CA3-CA1 neurons during sharp wave-associated population events. *Neuron*, 28(2):585–594.

Deuchars, J. and Thomson, A. M. (1996). CA1 pyramid-pyramid connections in rat hippocampus in vitro: dual intracellular recordings with biocytin filling. *Neuroscience*, 74(4):1009–1018.

Gan, J., Weng, S. M., Pernia-Andrade, A. J., Csicsvari, J., and Jonas, P. (2017). Phase-Locked Inhibition, but Not Excitation, Underlies Hippocampal Ripple Oscillations in Awake Mice In Vivo. *Neuron*, 93(2):308–314.

Gupta, A. S., van der Meer, M. A., Touretzky, D. S., and Redish, A. D. (2010). Hippocampal replay is not a simple function of experience. *Neuron*, 65(5):695–705.

Hu, W., Tian, C., Li, T., Yang, M., Hou, H., and Shu, Y. (2009). Distinct contributions of Na(v)1.6 and Na(v)1.2 in action potential initiation and backpropagation. *Nat. Neurosci.*, 12(8):996–1002.

Jadhav, S. P., Kemere, C., German, P. W., and Frank, L. M. (2012). Awake hippocampal sharp-wave ripples support spatial memory. *Science*, 336(6087):1454–1458.

Jahnke, S., Timme, M., and Memmesheimer, R. M. (2015). A Unified Dynamic Model for Learning, Replay, and Sharp-Wave/Ripples. *J. Neurosci.*, 35(49):16236–16258.

Kammerer, A., Tejero-Cantero, A., and Leibold, C. (2013). Inhibition enhances memory capacity: optimal feedback, transient replay and oscillations. *J Comput Neurosci*, 34(1):125–136.

Kempter, R., Gerstner, W., Hemmen, J. L. v., and Wagner, H. (1998). Extracting oscillations: Neuronal coincidence detection with noisy periodic spike input. *Neural Computation*, 10(8):1987–2017.

Lee, A. K. and Wilson, M. A. (2002). Memory of sequential experience in the hippocampus during slow wave sleep. *Neuron*, 36(6):1183–1194.

Leibold, C. and Kempter, R. (2006). Memory capacity for sequences in a recurrent network with biological constraints. *Neural Comput*, 18(4):904–941.

Liu, K., Sibille, J., and Dragoi, G. (2018). Generative Predictive Codes by Multiplexed Hippocampal Neuronal Tuplets. *Neuron*, 99(6):1329–1341.

Maier, N., Tejero-Cantero, A., Dorrn, A. L., Winterer, J., Beed, P. S., Morris, G., Kempter, R., Poulet, J. F., Leibold, C., and Schmitz, D. (2011). Coherent phasic excitation during hippocampal ripples. *Neuron*, 72(1):137–152.

Mainen, Z. F. and Sejnowski, T. J. (1996). Influence of dendritic structure on firing pattern in model neocortical neurons. *Nature*, 382(6589):363–366.

Nadasdy, Z., Hirase, H., Czurko, A., Csicsvari, J., and Buzsaki, G. (1999). Replay and time compression of recurring spike sequences in the hippocampus. *J. Neurosci.*, 19(21):9497–9507.

Oliva, A., Fernandez-Ruiz, A., Buzsaki, G., and Berenyi, A. (2016). Role of Hippocampal CA2 Region in Triggering Sharp-Wave Ripples. *Neuron*, 91(6):1342–1355.

Reichinnek, S., von Kameke, A., Hagenston, A. M., Freitag, E., Roth, F. C., Bading, H., Hasan, M. T., Draguhn, A., and Both, M. (2012). Reliable optical detection of coherent neuronal activity in fast oscillating networks in vitro. *Neuroimage*, 60(1):139–152.

Reyes, A. D. (2003). Synchrony-dependent propagation of firing rate in iteratively constructed networks in vitro. *Nat. Neurosci.*, 6(6):593–599.

Sasaki, T., Piatti, V. C., Hwaun, E., Ahmadi, S., Lisman, J. E., Leutgeb, S., and Leutgeb, J. K. (2018). Dentate network activity is necessary for spatial working memory by supporting CA3 sharp-wave ripple generation and prospective firing of CA3 neurons. *Nat. Neurosci.*, 21(2):258–269.

Schlesiger, M. I., Cannova, C. C., Boublil, B. L., Hales, J. B., Mankin, E. A., Brandon, M. P., Leutgeb, J. K., Leibold, C., and Leutgeb, S. (2015). The medial entorhinal cortex is necessary for temporal organization of hippocampal neuronal activity. *Nat. Neurosci.*, 18(8):1123–1132.

Shu, Y., Yu, Y., Yang, J., and McCormick, D. A. (2007). Selective control of cortical axonal spikes by a slowly inactivating K+ current. *Proc. Natl. Acad. Sci. U.S.A.*, 104(27):11453–11458.

Stark, E., Roux, L., Eichler, R., and Buzsaki, G. (2015). Local generation of multineuronal spike sequences in the hippocampal CA1 region. *Proc. Natl. Acad. Sci. U.S.A.*, 112(33):10521–10526.

Sullivan, D., Csicsvari, J., Mizuseki, K., Montgomery, S., Diba, K., and Buzsaki, G. (2011). Relationships between hippocampal sharp waves, ripples, and fast gamma oscillation: influence of dentate and entorhinal cortical activity. *J. Neurosci.*, 31(23):8605–8616.

Taxidis, J., Coombes, S., Mason, R., and Owen, M. R. (2012). Modeling sharp wave-ripple complexes through a CA3-CA1 network model with chemical synapses. *Hippocampus*, 22(5):995–1017.

Thome, C., Kelly, T., Yanez, A., Schultz, C., Engelhardt, M., Cambridge, S. B., Both, M., Draguhn, A., Beck, H., and Egorov, A. V. (2014). Axon-carrying dendrites convey privileged synaptic input in hippocampal neurons. *Neuron*, 83(6):1418–1430.

Turrigiano, G. G. (2017). The dialectic of Hebb and homeostasis. *Philos. Trans. R. Soc. Lond., B, Biol. Sci.*, 372(1715).

Willshaw, D. J., Buneman, O. P., and Longuet-Higgins, H. C. (1969). Non-holographic associative memory. *Nature*, 222(5197):960–962.

Figure Captions

Figure 1

A Suprathreshold activation by in-vitro cPSCs. **A** Examples of reconstructed excitatory (orange) and inhibitory (blue) conductance trains from in-vitro cPSCs. Note the different scale bars indicative for generally larger inhibitory conductances. **B** Ripple phase histograms (upper panels) and ripple phase profile as a function of time (lower panels) of all 1051 excitatory cPSCs aligned relative to cPSC onset (top) and SWR peak (bottom). Color code of the phase histograms (upper panels): the darker the more cPSCs fall into the phase bin. Color code of the phase profiles: cyclic with white corresponding to phase 0. **C** Left column: Spike raster plots for all 1051 excitatory cPSC (top) and 2000 random combinations of excitatory and inhibitory cPSC. Right column: Same as left for an additional constant input current $I_{\mathrm{DC}} = 100\mathrm{pA}$. **D** Phase histograms for all four tested conditions from C. P-values are derived from a Rayleigh test on uniform phase distribution.

Figure 2

History dependence of spike timing. **A** Example cPSC as derived from the in-vitro recordings. In order to generate APs at a specific cycles, the existing cPSC is removed and replaced by an artificial PSC at the starting at the same time as the removed PSC. Grey bar marks the cycle of the deleted/inserted PSCs. **B** Relationship between the minimal amplitude of the inserted PSC at cycle -2, which elicited a spike, and the amplitude of the PSC at the preceding cycle. Linear regression line is drawn in orange. Left column depicts the results without inhibition, right column is simulated with inhibition. **C** Regression slopes from the scatter plots in B.

Figure 3

Cycle-by-cycle capacity. **A** Schematic drawing of the generation of cPSCs. Every input conductance is constructed from 7 ripple cycles each of which samples inputs from a population of 10,000 synapses (only 7 shown). The weight vector is chosen according to a clipped Hebbian learning rule constructed from all P input patterns arriving in the 4th cycle (red). During the other cycles (blue) inputs are randomly sampled owing to interference with the patterns stored in the weight vector. **B** Retrieval quality Γ (averaged over 10 repetitions) for different numbers P and coding ratios f (colors as indicated). Left: only excitatory cPSCs (constructed as shown in A); Right: Excitatory and inhibitory cPSCs (inhibition from in-vitro experiments). **C** Population sparseness in the output versus populations sparseness in the input (coding ratio). Colors indicate different values of P.

Figure 4

Cycle-by-cycle capacity with adaptable threshold. **A** For varying coding ratios f and firing thresholds, output sparseness was computed and parameter combinations were marked

blue or orange for which output sparseness was below or above the input sparseness (coding ratio). The black line connects the parameter combinations where input and output sparseness were identical. **B** Examples of cPSCs and corresponding voltage responses for a case in the blue (top) and a case in the orange (bottom) regimes from A. The grey rectangle marks the signal cycle (4th cycle). **C** Retrieval quality as a function of P for various values of f (colors as indicated). Left: Simulations with only excitatory cPSCs. Right: Combination of excitatory cPSCs (constructed as shown in Figure 3A) and inhibitory cPSCs from in-vitro recordings.

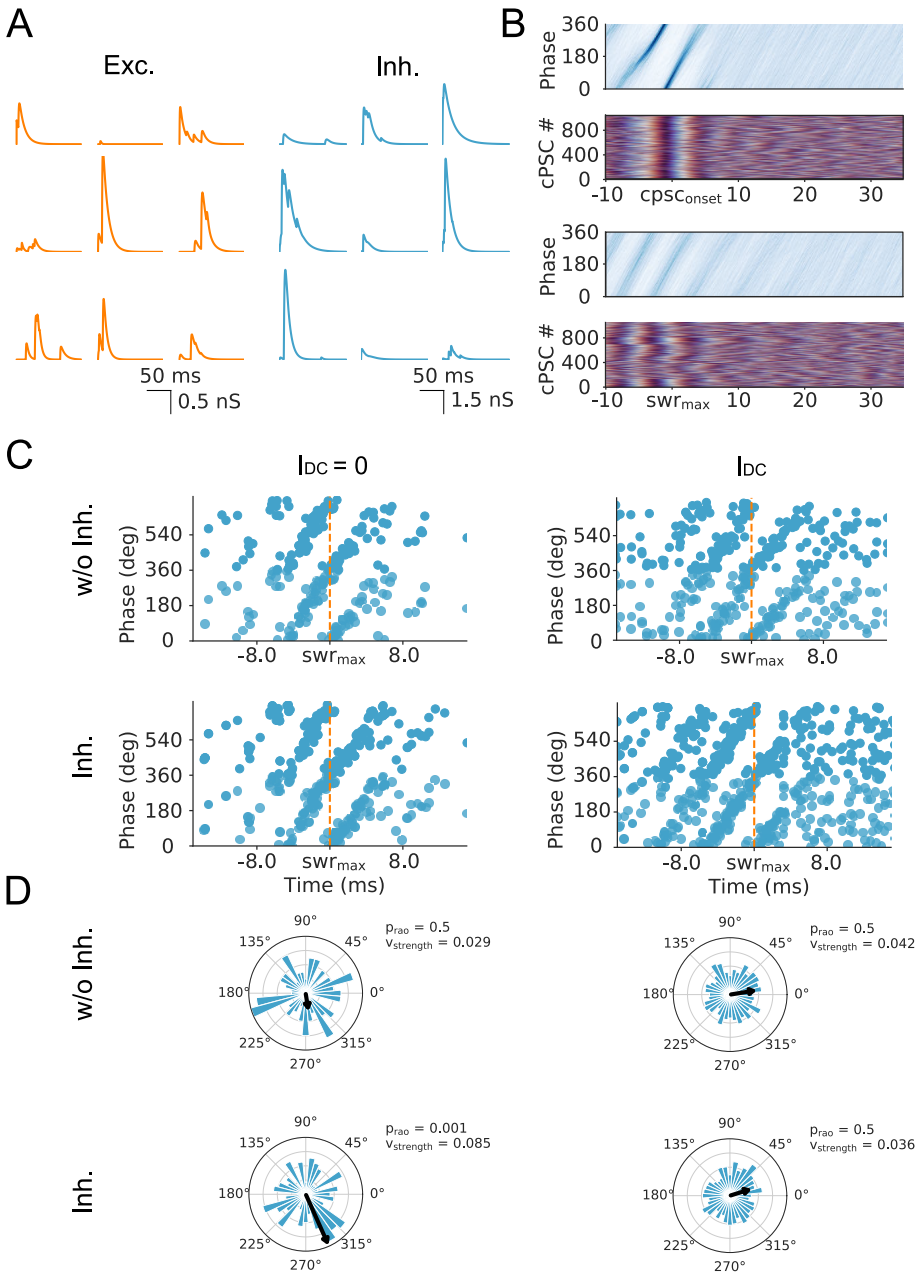
A
Exc.
Inh.
50 ms
0.5 nS
50 ms
1.5 nS
B
Phase
360
180
0
cPSC #
800
400
0
-10
cpsc_onset
10
20
30
Phase
360
180
0
cPSC #
800
400
0
-10
swr_max
10
20
30
C
I_DC = 0
I_DC
w/o Inh.
Inh.
Phase (deg)
540
360
180
0
-8.0
swr_max
8.0
Time (ms)
D
w/o Inh.
Inh.
90°
45°
0°
315°
270°
225°
180°
135°
p_rao = 0.5
v_strength = 0.029
p_rao = 0.5
v_strength = 0.042
p_rao = 0.001
v_strength = 0.085
p_rao = 0.5
v_strength = 0.036

Figure 1

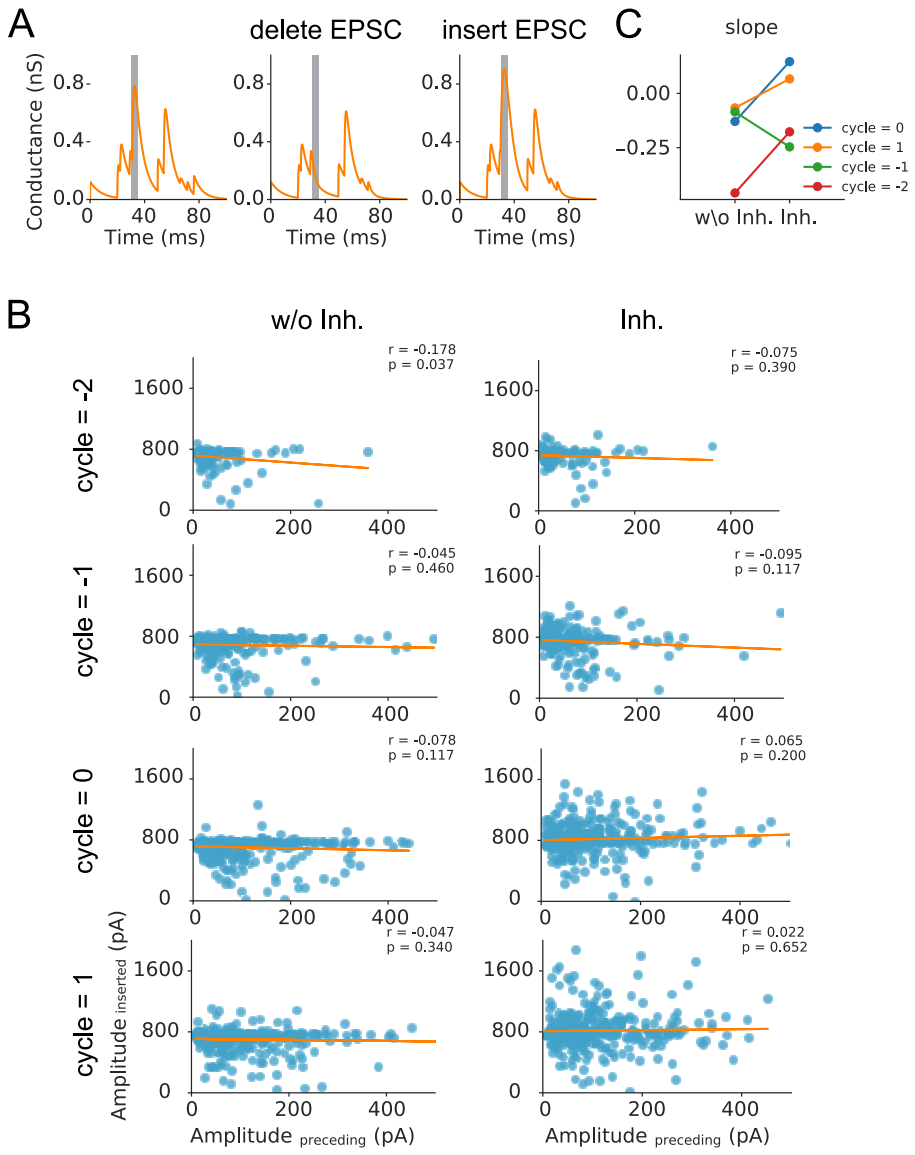
A
delete EPSC
insert EPSC
Conductance (nS)
0.8
0.4
0.0
0
40
80
Time (ms)
C
slope
0.00
−0.25
cycle = 0
cycle = 1
cycle = -1
cycle = -2
w\o Inh.
Inh.
B
w/o Inh.
Inh.
cycle = -2
cycle = -1
cycle = 0
cycle = 1
r = -0.178
p = 0.037
r = -0.075
p = 0.390
r = -0.045
p = 0.460
r = -0.095
p = 0.117
r = -0.078
p = 0.117
r = 0.065
p = 0.200
r = -0.047
p = 0.340
r = 0.022
p = 0.652
1600
800
0
200
400
Amplitude inserted (pA)
Amplitude preceding (pA)

Figure 2

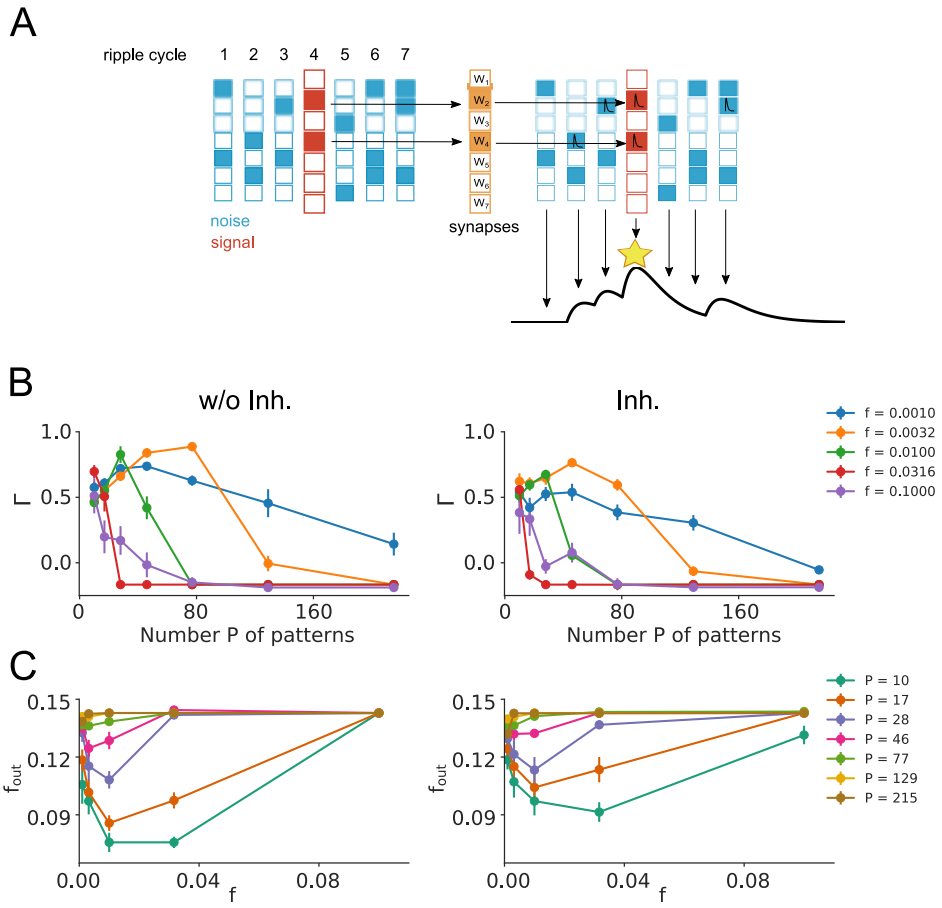
A
ripple cycle
1 2 3 4 5 6 7
noise
signal
synapses
B
w/o Inh.
Inh.
Γ
1.0
0.5
0.0
0
80
160
Number P of patterns
f = 0.0010
f = 0.0032
f = 0.0100
f = 0.0316
f = 0.1000
C
fout
0.15
0.12
0.09
0.00
0.04
0.08
f
P = 10
P = 17
P = 28
P = 46
P = 77
P = 129
P = 215

Figure 3

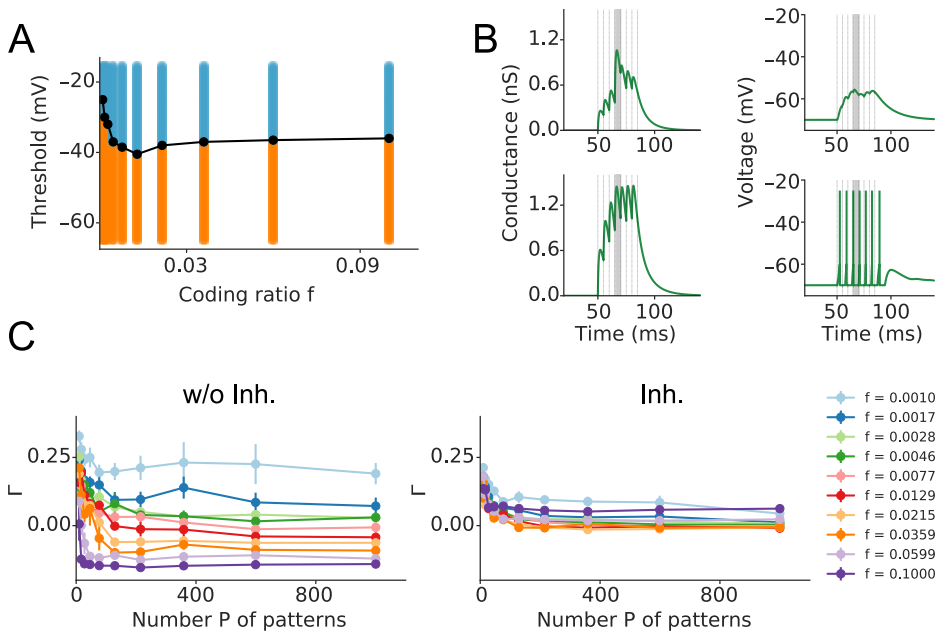
A
Threshold (mV)
-20
-40
-60
0.03
0.09
Coding ratio f
B
Conductance (nS)
1.2
0.6
0.0
50
100
Time (ms)
Voltage (mV)
-20
-40
-60
C
w/o Inh.
Inh.
Γ
0.25
0.00
0
400
800
Number P of patterns
f = 0.0010
f = 0.0017
f = 0.0028
f = 0.0046
f = 0.0077
f = 0.0129
f = 0.0215
f = 0.0359
f = 0.0599
f = 0.1000

Figure 4

3

Study 2: Action Potential Generation in an Anatomically Constrained Model of Medial Superior Olive Axons

Simon Lehnert (SL), Marc C. Ford (MCF), Olga Alexandrova (OA), Felix Felmy (FF), Benedikt Grothe (BG), and Christian Leibold (CL) designed the research. SL performed the computational modeling. Morphometric measurements were performed by MCF, and OA. FH and FF performed the electrophysiological recordings. SL, MCF, OA, FH, and FF analyzed the data. SL, MCF, FF, BG, and CL wrote the paper.

The paper has been published in *The Journal of Neuroscience* (Lehnert et al., 2014).

Systems/Circuits

Action Potential Generation in an Anatomically Constrained Model of Medial Superior Olive Axons

Simon Lehnert,[1] Marc C. Ford,[1,2] Olga Alexandrova,[1] Franziska Hellmundt,[1,2] Felix Felmy,[1,3] Benedikt Grothe,[1] and Christian Leibold[1]

[1]Department Biology II, [2]Graduate School of Systemic Neurosciences, and [3]Department Biology I, BioImaging Zentrum, Ludwig-Maximilians-Universität München, D-82152 Planegg-Martinsried, Germany

Neurons in the medial superior olive (MSO) encode interaural time differences (ITDs) with sustained firing rates of >100 Hz. They are able to generate such high firing rates for several hundred milliseconds despite their extremely low-input resistances of only few megaohms and high synaptic conductances *in vivo*. The biophysical mechanisms by which these leaky neurons maintain their excitability are not understood. Since action potentials (APs) are usually assumed to be generated in the axon initial segment (AIS), we analyzed anatomical data of proximal MSO axons in Mongolian gerbils and found that the axon diameter is <1 μm and the internode length is ~100 μm. Using a morphologically constrained computational model of the MSO axon, we show that these thin axons facilitate the excitability of the AIS. However, for ongoing high rates of synaptic inputs the model generates a substantial fraction of APs in its nodes of Ranvier. These distally initiated APs are mediated by a spatial gradient of sodium channel inactivation and a strong somatic current sink. The model also predicts that distal AP initiation increases the dynamic range of the rate code for ITDs.

Key words: **action potential; axon; coincidence detection; interaural time difference; sound localization**

Introduction

The generation of action potentials (APs) is widely assumed to take place in the axon initial segment (AIS). Evidence for this assumption stems predominantly from cortical pyramidal neurons and cerebellar Purkinje neurons using simultaneous somatic and axonal whole-cell recordings (Stuart and Sakmann, 1994; Stuart et al., 1997; Kole et al., 2007; Shu et al., 2007) and voltage-sensitive dye imaging (Palmer and Stuart, 2006; Foust et al., 2010; Palmer et al., 2010; Popovic et al., 2011). At rest, these neurons have relatively high input resistances of 10–200 MΩ, allowing them to integrate synaptic inputs over several milliseconds. Thus, during depolarizing stimuli, the soma generally serves as a strong and temporarily stable current source for the AIS. In neurons with very low input resistances of 2–5 MΩ, the mechanisms of AP initiation have not yet been studied in such great detail. In those cells, the membrane time constants are too short to allow the soma to serve as a temporarily stable current source. Conversely, the soma might even act as a current sink to the AP generating zone and therefore increases the AP threshold at the AIS.

Received Sept. 20, 2013; revised March 5, 2014; accepted March 8, 2014.

Author contributions: S.L., M.C.F., O.A., F.F., B.G., and C.L. designed research; S.L., M.C.F., O.A., F.H., and F.F. performed research; S.L., M.C.F., O.A., F.H., and F.F. analyzed data; S.L., M.C.F., F.F., B.G., and C.L. wrote the paper.

This work was supported by the German Research Foundation via the Collaborative Research Center 870 and the Elisabeth und Helmut Uhl Stiftung.

The authors declare no competing financial interests.

Correspondence should be addressed to Christian Leibold, Computational Neuroscience, Department Biology II, Ludwig-Maximilians-University Munich, Grosshaderner Strasse 2, D-82152 Planegg-Martinsried, Germany. E-mail: leibold@bio.lmu.de.

DOI:10.1523/JNEUROSCI.4038-13.2014

 0270-6474/14/345370-15$15.00/0

In the present study, we investigated AP generation in neurons of very low input resistance, the principal cells of the medial superior olive (MSO). These neurons have membrane time constants in the range of only a few hundreds of microseconds and input resistances as low as 5 MΩ (Scott et al., 2005; Couchman et al., 2010). The MSO is a binaural nucleus in the ascending auditory pathway. MSO neurons encode the azimuthal position of low-frequency sounds via differences in the time of arrival at the two ears by their firing rate (Goldberg and Brown, 1969; Yin and Chan, 1990; Fitzpatrick et al., 1997; Brand et al., 2002) with a precision of only a few tens of microseconds. This exquisite temporal precision of binaural coincidence detection is partly achieved by the fast membrane time constants of neurons resulting from the high expression of low-voltage-activated potassium channels and hyperpolarization-activated cation channels (Svirskis et al., 2002; Koch et al., 2004; Scott et al., 2005; Mathews et al., 2010; Baumann et al., 2013), both of which are already open at rest. Despite the resulting low input resistance, these neurons can fire at high rates of ~100 Hz and more. The mechanisms by which this is possible are still unresolved.

In this article, we address the question of how AP generation is accomplished in leaky neurons using a computational model of MSO neurons with axonal morphology based on new detailed morphometric data. Our simulations show that, despite the leaky soma, the AIS remains electrotonically isolated and retains its ability to generate APs. However, we also identified conditions under which the APs are initiated at the nodes of Ranvier. This distal initiation of APs increases the dynamic range of the rate code of interaural time differences (ITDs).

Materials and Methods

General

All experiments were performed according to institutional guidelines, and national and regional laws; it was approved by the Regierung von Oberbayern (AZ55.2–1-54–2531-105–10). All results are given as the mean ± SEM.

Retrograde labeling of MSO cells

Mongolian gerbils (*Meriones unguiculatus*) of either sex [$n = 4$; postnatal day 29 (P29) to P31] were anesthetized with pentobarbital (2 mg/kg body weight) and intracardially perfused with ice-cold Ringer's solution containing 0.1% heparin. After decapitation, the brainstem was removed from the skull under ice-cold dissection solution comprising the following (in mM): 125 NaCl, 2.5 KCl, 1 $MgCl_2$, 0.1 $CaCl_2$, 25 glucose, 1.25 NaH_2PO_4, 25 $NaHCO_3$, 0.4 ascorbic acid, 3 *myo*-inositol, and 2 pyruvic acid (all chemicals were from Sigma-Aldrich). For retrograde labeling of MSO cells, the brainstem was sectioned along the posterior–anterior axis until the MSO, lateral superior olive, and superior paraolivary nucleus (SPN) were clearly visible. Borosilicate glass micropipettes with a tip diameter of 10–15 μm were filled with a 10% solution of tetramethylrhodamine dextran (3000 molecular weight; Invitrogen) and visually guided to the SPN. Cells were labeled by applying 2–4 electroporation pulse trains (50 ms, 50 V, 10 Hz; modified from previous studies; Ford et al., 2009). Subsequently, the explants were transferred to a chamber containing oxygenated incubation solution (same as incubation solution, but containing 2 mM instead of 0.1 mM $CaCl_2$) and incubated at room temperature for 90 min. Thereafter, brainstems were immersion fixed at room temperature overnight in 4% paraformaldehyde solution.

Immunohistochemistry

Brainstems were sectioned transversally (80–120 μm slice thickness), rinsed in PBS, and transferred to blocking solution containing 1% bovine serum albumin, 2% Triton X-100, and 0.1% saponin in PBS. Multiple-immunofluorescence labeling was performed with the following primary antibodies: ankyrin G (sc-28561; rabbit; 1:500; Santa Cruz Biotechnology), Kv1.2 (75-008 clone K14/16; mouse; 1:500; NeuroMab), microtubule-associated protein 2 (CH22103; chicken polyclonal; 1:1000; Neuromics), and myelin basic protein (ab7349; rat monoclonal; 1:20; abcam). The incubation time (4°C) for primary antibodies was 3 d. After incubation with secondary antibodies (1–2 d; 4°C) and rinsing in PBS, sections were mounted with Vectashield mounting medium.

Confocal microscopy

Confocal images were acquired with a TCS SP5-2 confocal laser-scanning microscope (Leica Microsystems) equipped with HCX PL APO 63×/numerical aperture 1.3 glycerol objective. Fluorochromes were excited at 405, 488, 561, 594, and 633 nm for aminoethylcoumarin acetate, DyLight488, tetramethylrhodamine dextran, Alexa Fluor 594, and DyLight649, respectively. The emission filters for these fluorochromes were set to (in the same order) 410–460, 510–550, 565–585, 605–625, and 640–760 nm. For each optical section the images were collected sequentially for four to five fluorochromes. Stacks of 8-bit grayscale images were obtained with axial distances of 290 nm between optical sections and a pixel size of 120.4 nm. To obtain an improved signal-to-noise ratio, each section image was averaged from five successive scans. After stack acquisition, the Z chromatic shift between color channels was corrected. RGB stacks, montages of RGB optical sections, and maximum-intensity projections were assembled into tables by using ImageJ 1.37k plugins and Photoshop version 8.0.1 (Adobe Systems) software.

Morphometry

Morphometric measurements were made from overlapping image stacks of MSO principal cells. Using the ImageJ 1.37k paint-brush tool, individual axons of MSO cells filled with tetramethylrhodamine dextran were manually labeled by following single axons subsequently through each optical section of the confocal stack (Werthat et al., 2008; for dendrites, see Couchman et al., 2010). Afterward, the neighboring axons were digitally deleted. We refer to this method as digital extraction. The same axon was identified in the neighboring overlapping confocal stacks and digitally extracted. AISs and nodes of Ranvier were identified on the basis ankyrin G/Kv1.2 antibody staining. AIS and internode lengths were measured in three dimensions in confocal stack images using the ImageJ 1.37k Sync Measure 3D tool. AIS and internodal axon diameters were measured at the positions defined by ankyrin G and Kv1.2 labeling (see Fig. 2*B*) in maximum-intensity projections of image stacks based on tetramethylrhodamine dextran labeling. The mean diameter of the first internode was averaged from measurements at several (10–29) different positions between the outer borders of the juxtaparanodes (see Fig. 2*B*, K3 and K6).

Electrophysiology

Experimental procedures were as described in Couchman et al. (2010). In brief, Mongolian gerbils of either sex of P60–P80 were anesthetized with isoflurane. Brains were removed after decapitation, and 110-μm-thick horizontal brainstem slices were taken with a VT1200S vibratome (Leica) in dissection solution containing the following (in mM): 50 sucrose, 25 NaCl, 27 $NaHCO_3$, 2.5 KCl, 1.25 NaH_2PO_4, 3 $MgCl_2$, 0.1 $CaCl_2$, 25 glucose, 0.4 ascorbic acid, 3 myo-inositol, and 2 Na-pyruvate, pH 7.4 when bubbled with 95% O_2 and 5% CO_2. Slices were incubated in recording solution (same as slice solution but with 125 mM NaCl, no sucrose, and 2 mM $CaCl_2$ and 1 mM $MgCl_2$) at 36°C for 45 min, bubbled with 5% CO_2 and 95% O_2.

Incubated slices were placed into a recoding chamber attached to a BX51WI microscope (Olympus) equipped with a custom-made gradient contrast illumination and continuously perfused with recording solution kept at 34–36°C by a Warner Instruments heating system. MSO neurons were visualized at 60× magnification with a Retiga 2000 DC camera (Till Photonics/FEI Munich). Current-clamp whole-cell recordings were performed using an EPC10/2 amplifier (HEKA Elektronik) on visually identified MSO neurons with electrode resistances of ~3 MΩ. Access resistance was estimated in voltage-clamp after break in and was bridge balanced to 100% in current-clamp mode. The internal recording solution consisted of the following (in mM): 145 K-gluconate, 4.5 KCl, 15 HEPES, 2 Mg-ATP, 2 K-ATP, 0.3 Na_2-GTP, 7.5 Na_2-phosphocreatine, 5 K-EGTA, pH 7.2. The liquid junction potential was corrected on-line with an estimated value of 17 mV.

Computational modeling

Based on the morphometric analysis, a multicompartmental model was created to study the generation of APs in MSO principal cells. The model consists of one large somatic compartment that combines the somatic and dendritic membrane surface (Ashida et al., 2007). The model focuses on the axonal morphology, since APs are generally assumed to be generated there. The axon model consisted of an unmyelinated AIS followed by an extensive myelinated part that was periodically interrupted by 21 nodes of Ranvier. Figure 1*A* shows a schematic drawing of the first segments of the model up to the fourth node of Ranvier (R4). The AIS was further subdivided into a tapering part (tAIS) and a constant part (cAIS), resembling the actual geometry of the AIS. The voltages of the compartments followed a Hodgkin–Huxley-type equation as follows:

$$C_m \frac{dV}{dt} = -(I_{Na} + I_{KHT} + I_{KLT} + I_h + I_{lk} + I_{syn} + I_{axial} + I_{ext}),$$

where I_{ext} is the external current, and the ohmic transmembrane currents are as follows:

$$I_x(V) = g_x a_x^m b_x^n (V - E_x).$$

Here, C_m is the membrane capacitance, g_x is respective peak conductances, a_x and b_x are the gating variables, and m and n are the respective cooperativities. The dynamics of the gating variables are modeled according to first-order kinetics, as follows:

$$\frac{da}{dt} = \frac{a_\infty - a}{\tau_a} \text{ and } \frac{db}{dt} = \frac{b_\infty - b}{\tau_b}$$

where a_∞ and b_∞ are the steady-state activation functions, and τ_a and τ_b are the voltage-dependent time constants.

The axial current for the ith compartment is defined as follows:

$$I^{i}_{\text{axial}} = \frac{V_{i-1} - V_i}{R^{i-1,\,i}_{\text{axial}}} + \frac{V_{i+1} - V_i}{R^{i+1,\,i}_{\text{axial}}},$$

in which R_{axial} denotes the axial resistance between the ith compartment and its respective neighboring compartments. The axial resistance results from the geometry of the axonal segment (diameter and length) as well as the specific axial resistivity of 100 Ωcm, which is in the range of usually assumed values (Mainen et al., 1995; Mainen and Sejnowski, 1996; Shu et al., 2007).

The specific model for the sodium channel was taken from Scott et al. (2010) with a reversal potential for sodium of 69 mV and a modified conductance density in the axon of 4 nS/μm^2 to fit the firing threshold of our current-clamp measurements (see Fig. 4). We chose the somatic sodium conductance density to be 0.2 nS/μm^2, a value 20-fold smaller than that in the axon and reflecting the low sodium channel density found in MSO principal cell somata (Scott et al., 2010). The high-threshold potassium channel was modeled according to Rothman and Manis (2003) without a slow activation variable and only at the soma since it had only little effect in the axon. The low-threshold potassium channel (KLT) was modeled according to (Mathews et al., 2010) and was present in the soma and all unmyelinated axonal compartments. The potassium reversal potential was set to −90 mV. The hyperpolarization-activated cation channel gives rise to a somatic hyperpolarization (h)-activated cation current (I_h), which was modeled using the kinetics measured in dorsal MSO neurons (Baumann et al., 2013), with a reversal potential of −35 mV. The resting potential of −68 mV and the somatic input resistance of 5 MΩ were set by adjusting the peak conductances of KLT and h current. The somatic surface was set to 8750 μm^2, such that we get a somatodendritic capacitance of 70 pF (Rautenberg et al., 2009), assuming a specific capacitance of 0.8 $\mu F/cm^2$ (Gentet et al., 2000; Shu et al., 2007). As a consequence, the somatic membrane time constant is 350 μs, which closely resembles the measured membrane time constants *in vitro* (Scott et al., 2005; Couchman et al., 2010). The specific myelin conductance per lamella was set to 0.1 $\mu F/cm^2$ (McIntyre et al., 2002, 2004). Together with a g-ratio of 0.7 and an assumed myelin periodicity of 16 nm (Agrawal et al., 2009), our standard model exhibits nine myelin lamellae. Thus, we obtain a specific capacitance of the myelin sheath of 0.0111 $\mu F/cm^2$, similar to the value of 0.01 $\mu F/cm^2$ used in Kuba et al. (2006) for axons of nucleus laminaris (NL) neurons. Some computational studies of axons use specific capacitances per lamella that are significantly higher; however, they compensate for this by a larger number of myelin lamellae. Using a substantially larger myelin capacitance (e.g., three times or higher) would cause propagation failures of generated APs in our model, a result that would contradict the secure propagation of APs known from MSO principal neurons (Scott et al., 2007). This matching of an experimental finding argues in favor of our parameter choice. The validity of the parameter choice is further supported by our physiological measurements of firing thresholds for onset-like responses in Figure 4.

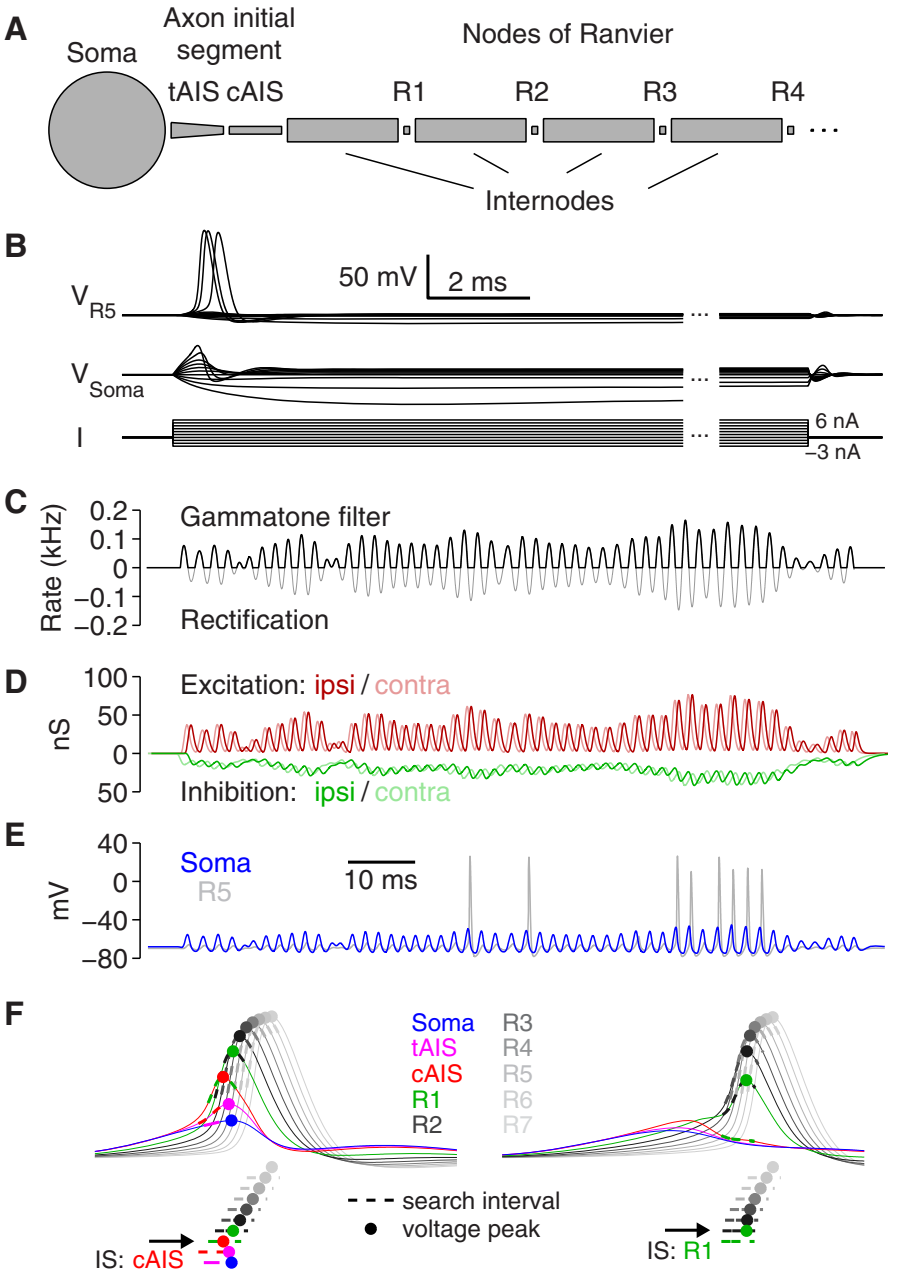

Figure 1. Computational model. ***A***, Schematic drawing of the first segments from the soma to R4 of the MSO model neuron. The AIS is subdivided into two compartments: the tAIS and the cAIS. ***B***, Voltage response in different compartments (top, R5; middle, soma) to current injections at the soma (bottom). ***C***, ***D***, The input conductances were obtained from noise that is filtered by a gammatone filter with a center frequency of 500 Hz (gray) and half-wave rectified (***C***, black). The trace from ***C*** is transformed into conductance inputs by convolution with excitatory (ipsilateral, dark red; contralateral, light red) and inhibitory (ipsilateral, green; contralateral, light green) synaptic kernels (***D***; see Materials and Methods). ***E***, Voltage responses of the soma (blue) and R5 (light gray) of the model when driven with the conductance trains depicted in ***D***. ***F***, The AP initiating segment (IS, black arrow) is derived from the voltage traces at the individual compartments (color coded segments: blue, soma; pink, tAIS; red, cAIS; green, R1; dark gray to light gray, R2–R7). Example traces show a cAIS-generated (left) and an R1-generated (right) AP. Dashed traces indicate the search intervals of duration L that are defined by the voltage peak (dot) of the downstream segment (see Materials and Methods). The voltage peak that occurs earliest in time defines the SIS.

A detailed account of the geometrical and electrical features of the model is given in Tables 1 and 2, respectively.

In response to somatic current injections, the neuron model exhibits typical onset behavior (Fig. 1*B*; i.e., it fires only one AP; Scott et al., 2005; Couchman et al., 2010) at the onset of the depolarizing pulse. The AP amplitude at the soma resembles physiologically measured values of ~10 mV (Scott et al., 2005; Couchman et al., 2010), whereas, at the nodes of Ranvier, the APs exhibit usual amplitude values of ~100 mV.

Table 1. Geometrical parameters of the model

Parameters	Values
Soma/somatodendritic compartment	
Area	8750 μm^2
Axon initial segment (tapering part)	
Length	10 μm
Large diameter	1.64 μm
Small diameter	0.66 μm
Axon initial segment (constant part)	
Length	10 μm
Diameter	0.66 μm
Internodes	
Length	100 μm
Inner diameter	0.66 μm
Outer diameter	0.948 μm (corresponding to a g-ratio of 0.7),
Myelin lamellae	9 (corresponding to a myelin periodicity of 16 nm)*
Node(s) of ranvier	
Length	1 μm
Diameter	0.66 μm

*From Agrawal et al. (2009).

Table 2. Maximum conductances of voltage-gated channels

Channels	Soma	tAIS	cAIS	Internodes	Nodes
gNa	0.2	4	4	0	4
gKHT	0.1	0	0	0	0
gKLT	1.55	1.55	1.55	0	1.55
gh	0.02	0.02	0.02	0	0
glk	0.0005	0.0005	0.0005	0.0002	0.05

Data are in nS/μm^2.

Since ongoing synaptic bombardment under *in vivo* conditions increases the leakiness of the neuron, we decided to study AP generation using a temporally extended naturalistic stimulus that resembles the periodicity of a cochlear channel with a specific center frequency. Our stimuli were generated using bandpass-filtered white noise $n(t)$ (Fig. 1*C*) that was linearly filtered (convolved) with a gammatone kernel, as follows:

$$f(t) = t^4 e^{-t\gamma} \cos(t\omega_c),$$

with $\gamma(\omega_c) = 24.7(4.37 \times \omega_c/(2\pi)+1)$ in kilohertz (Glasberg and Moore, 1990) and the center frequency $\omega_c/(2\pi)$ in kilohertz. The filter output was half-wave rectified and normalized to yield a spike probability function with a mean AP rate R (200 Hz) during the stimulus length l = 300 ms. The resulting input train was then multiplied with a factor S, which we call the stimulus intensity, and afterward convolved with double-exponential functions G_{exc} and G_{inh}, which we created to resemble electrophysiologically measured synaptic kinetics for excitatory and inhibitory synaptic activity (Couchman et al., 2010):

$$G_{exc}(t) = g_{exc} \frac{(1 - e^{-t/1.0})^{1.3}\, e^{-t/0.27}}{\max((1 - e^{-t/1.0})^{1.3}\, e^{-t/0.27})} \text{ and}$$

$$G_{inh}(t) = g_{inh} \frac{(1 - e^{-t/0.4})\, e^{-t/1.6}}{\max((1 - e^{-t/0.4})\, e^{-t/1.6})}.$$

Here, g_{exc} = 37 nS and g_{inh} = 57 nS are the peak conductances of single fibers (Couchman et al., 2010), and time t is considered in milliseconds. Examples for such synaptic conductance trains are shown in Figure 1*D*. Unless mentioned otherwise, we used two inhibitory inputs based on the same stimulus wave form; one advances the excitatory inputs by 0.6 ms and one lags them by 0.11 ms (see Impact of distal AP initiation on ITD coding; Leibold, 2010). Apart from the simulations in which the inhibitory inputs are essential (see Figs. 5*M*, 8), all simulations were performed with only excitatory inputs activated.

Neuron model with dendrites

To test the robustness of our findings in a model with dendrites, we performed simulations (see Fig. 8) in a model variant in which two identical dendrites (five compartments each) were added to the soma. Excitatory synapses were placed at the dendrites (ipsilateral inputs at the lateral dendrite, contralateral inputs at the medial dendrite), and inhibitory synapses were restricted to the soma (Kapfer et al., 2002). The parameters of the dendritic model were chosen such that the basic characteristics at the soma (input resistance, resting potential, capacitance, and EPSP kinetics) matched that of the model with a single somatodendritic compartment and hence the physiological data from Scott et al. (2005) and Couchman et al. (2010). Most importantly, the length of each of the dendrites was 200 μm, with a constant diameter of 5 μm. The somatic surface was reduced to 2467 μm^2, such that the total cell surface remained at 8750 μm^2, which is equal to the model with only one somatodendritic compartment. The geometrical length of the dendritic compartments appears slightly longer than that observed in MSO neurons (Rautenberg et al., 2009), since we did not take into account branching of dendrites but had to match the overall cell surface for comparability.

In the dendritic compartments, sodium channels were omitted (Scott et al., 2010), and thus the sodium density of the remaining somatic compartment was scaled up such that the total sodium conductance matched that of the simpler model with only one somatodendritic compartment. The conductance of the low-threshold potassium channels decayed exponentially along the dendrites with a length constant of 74 μm (Mathews et al., 2010). The peak conductance at the somatic compartment was thereby identical to that of the simpler model. The conductance of the h current was chosen to follow the same gradient along the dendrite to keep the local balance of the two channels. Finally, the input resistance and resting potential of the model with dendrites were matched to those of the simpler model by adjusting the peak conductances of the h current and the passive leak current.

Analysis of simulations

In our simulations, APs during ongoing stimulation were often not detectable in the soma (Fig. 1*E*). However, at more distal locations in the axon, the amplitude and kinetic differences of subthreshold responses and APs are much larger, and, thus, at the more distal axonal compartments these two cases are very easy to separate by a simple amplitude threshold.

Initiating segment. Since the MSO model is described by a system of coupled differential equations, the generation of an AP necessarily requires the interplay of all compartments. The question of where an AP is generated thus can only be answered by a phenomenological criterion. This phenomenological AP-initiating segment was identified as follows (Fig. 1*F*). First, a stimulus evoked AP was defined by a voltage threshold criterion in R7 at which AP and no AP events are clearly separable. Second, we inspected the voltage trace at the axonal nodes of Ranvier and the AIS going from distal to proximal, and identified the segment-specific AP times via the voltage peaks (above −50 mV) that occurred within a certain time interval of duration L around the voltage peak in the (previous) downstream node. The duration L of this time interval is determined by $L = 5.33\,\lambda$, where λ is the impulse conduction time from node to node for a strong current stimulus delivered at rest, which elicits a clear AIS AP. The window is asymmetrically aligned to the previous voltage peak such that the preceding part is three times longer than the part following the voltage peak. The factor 5.33 allows for a slower AP propagation of the AIS and near-threshold stimuli. Within the set of all detected voltage peaks, the earliest in time defines the AP initiation segment. This algorithm has been tested against a variety of simple threshold and phase space criteria, and has proven to give more reliable results for different axonal morphologies and different input parameters, even for extremely fast voltage deflections.

In simulations in which we tested higher somatic input resistances (see Fig. 5*L*), the somatic AP was strongly influencing the voltage trace in the AIS, which made it difficult to identify a clear AIS voltage peak. We therefore identified the AIS AP as the first drop of the voltage derivative below 50 V/s, identifying a shoulder in the voltage deflection.

In few cases (see Fig. 6) during orthodromic propagation does the AP amplitude initially decrease before increasing again in the more distal

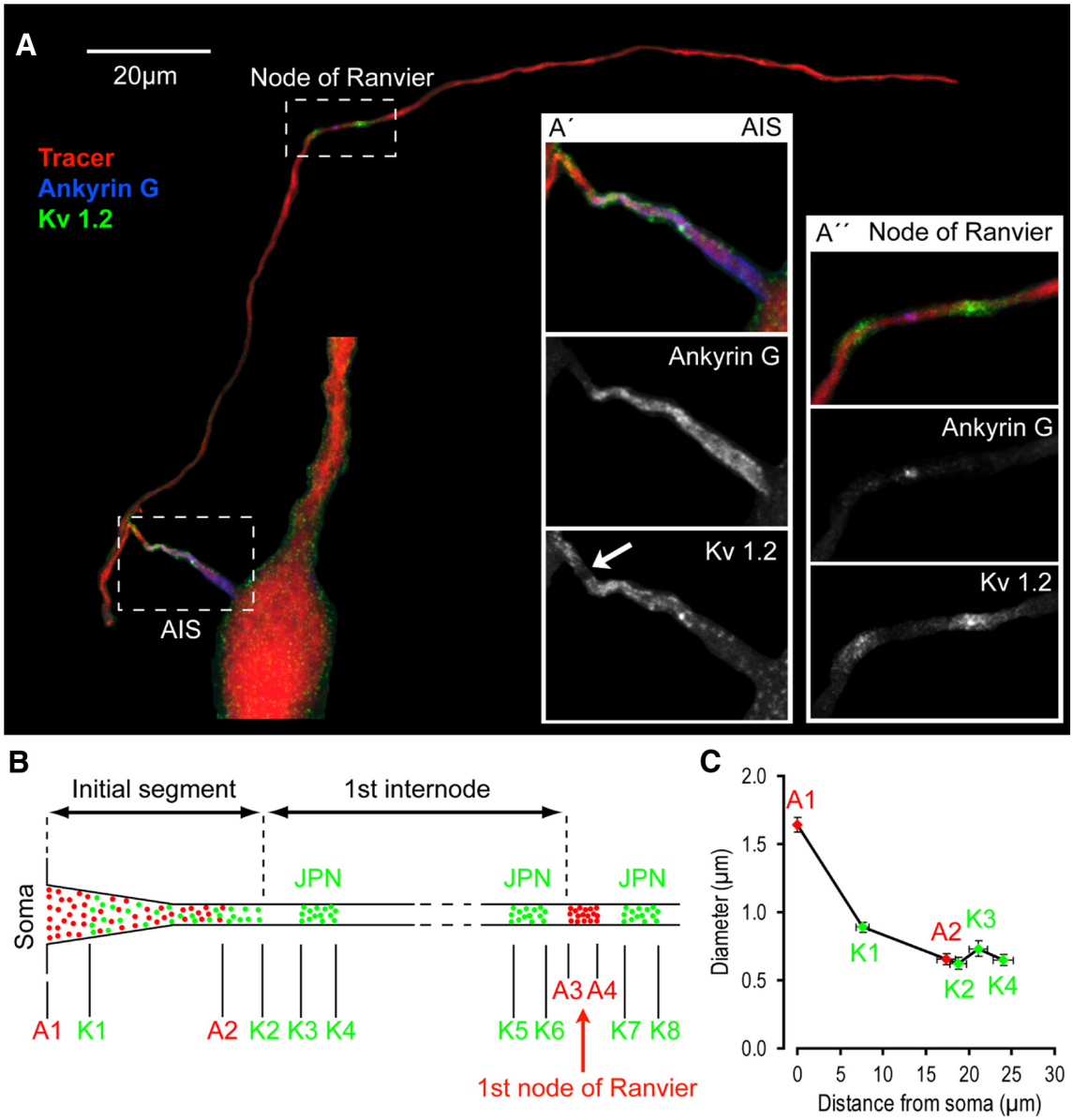

Figure 2. Morphometry of the AIS and first internodal segments in MSO neurons. ***A***, Retrogradely labeled MSO neuron after digital extraction from the surrounding area. Insets ***A′*** and ***A″*** show magnifications of the AIS and first node of Ranvier, respectively. ***B***, Schematic of the proximal axon segment comprising the AIS, the first internode, and the first node of Ranvier, illustrating the positions where measurements were made. Red and green dots indicate the distribution of ankyrin G and Kv1.2 immunolabeling in the AIS and axon. A1–A4 and K1–K8 indicate the borders of ankyrin G- and Kv1.2-positive domains, respectively. JPN, Juxtaparanodes. ***C***, Mean diameter of the AIS at various positions plotted as a function of the mean distance from the soma. Diameter and distance measurements were made at the positions indicated in ***B***. Error bars show the SEM.

axonal segments. Such APs were also labeled as being distally initiated, even though they would have been an AIS AP according to the time-window criterion.

Relative slope during ongoing conductance trains. To identify the input features that are most predictive for spiking, we placed particular emphasis on current amplitude and the relative current slope (derivative divided by amplitude). We chose relative slope because the derivative of any oscillating function linearly scales with the amplitude of the input, and, thus, without such normalization, dependencies on slopes are confounded by amplitude effects. To determine the relative derivative of the input current in Figure 7, *G* and *H*, we normalized by the amplitude of a high-pass-filtered version (fourth-order Butterworth filter with a cutoff of one-third of the stimulation frequency) of the input current rather than by the actual amplitude itself. This was necessary to obtain the actual local relative slope for each cycle and not a distorted value caused by the temporal summation of the input currents of high-frequency stimuli.

ITD coding

To assess how well the responses of the model neuron resolve an ITD τ, we computed the Fisher information $I(\tau)$, assuming a Gaussian distribution of AP counts. From at least 90 repetitions of a 300 ms stimulus, we obtained the mean AP count (tuning curve) $\mu(\tau)$ and its variance $\nu(\tau)$, and calculated the Fisher information as follows:

$$I(\tau) = \frac{\mu'(\tau)^2}{\nu(\tau)} + \frac{1}{2}\left(\frac{\nu'(\tau)}{\nu(\tau)}\right)^2$$

Results

Morphometry of the AIS and proximal axon

Using a combination of retrograde tracing of MSO neurons and immunohistochemical labeling of ankyrin G and Kv1.2 channels, a detailed morphometric analysis of the AIS and proximal axon of

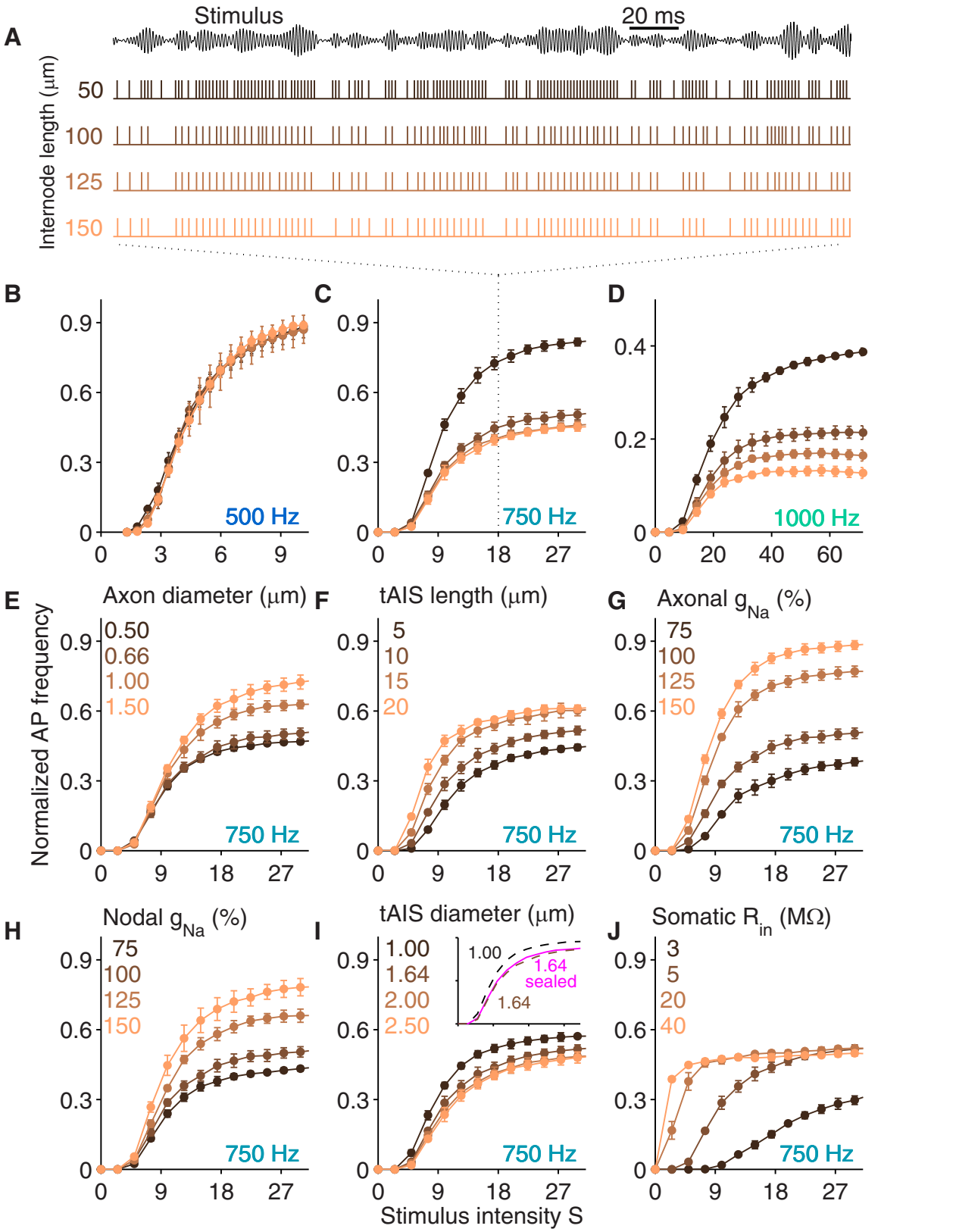

Figure 3. Input/output functions of the model. ***A***, Spike trains were simulated for bandpass stimuli (top trace) of duration 300 ms. The four spike trains are derived from the same (frozen noise) stimulus with a center frequency of 750 Hz and intensity $S = 18$ (as indicated by dotted lines) and internode lengths as indicated by colors. ***B–J***, Graphs depict firing probabilities for different (color-coded) morphological parameters and sodium conductances and for increasing stimulus intensities S (see Materials and Methods). Parameters that were varied are internode length (color coded) and center frequency (***B–D***), axonal diameter (***E***), length of the AIS tapering part (***F***), peak sodium conductance in all unmyelinated parts of the axon (***G***), peak sodium conductance in the nodes of Ranvier (***H***), proximal diameter of the AIS tapering part (***I***), and somatic input resistance (***J***). Inset in ***I*** compares relative AP frequencies of two control traces (with different tAIS diameter) from ***I*** to a model where all subthreshold transmembrane conductances were removed from the tAIS (pink trace, sealed).

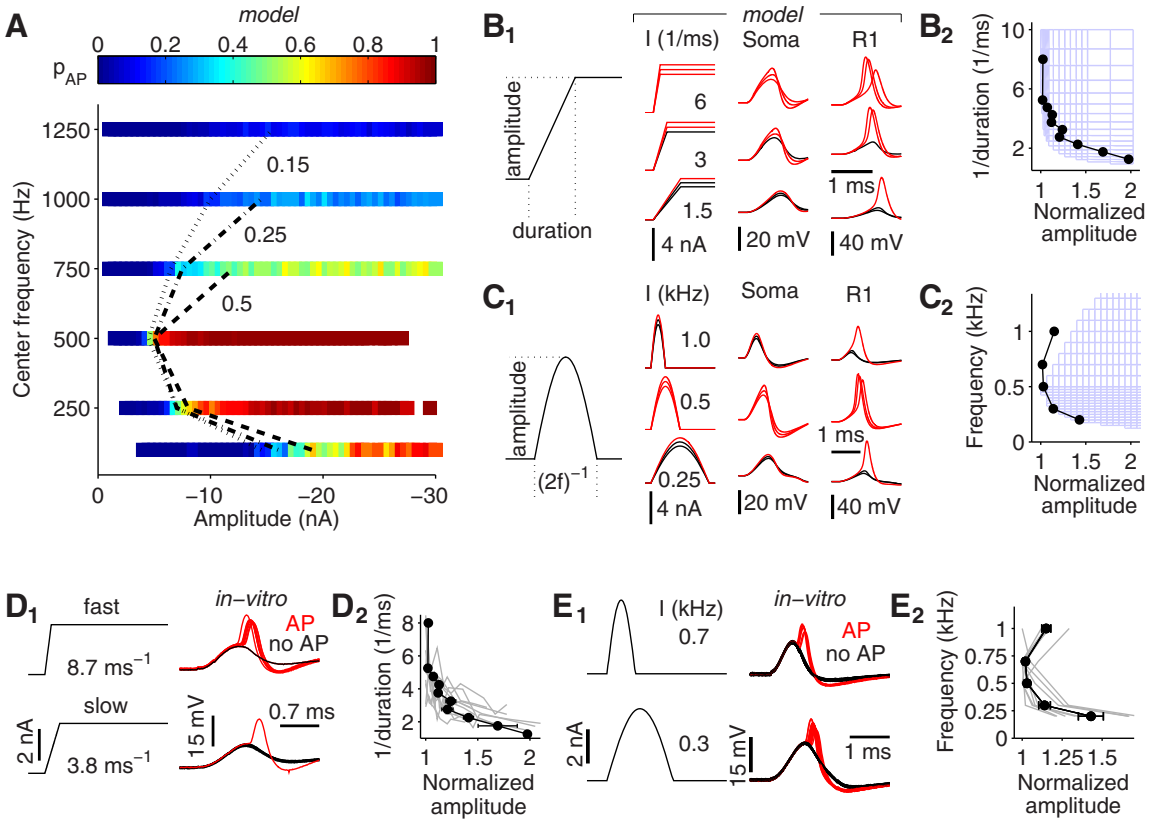

Figure 4. Frequency-dependent AP threshold. ***A***, Firing probability (color coded) of the model cell as a function of center frequency and cycle amplitude for ongoing inputs. Iso-probability contours are shown for firing probabilities of 15% (dotted trace), 25% (dot-dashed trace), and 50% (dashed trace). ***B*$_1$**, Ramp stimulus (left) and raw data of the simulation for three different ramp durations (right). Black and red traces indicate subthreshold and AP responses, respectively. ***B*$_2$**, Light blue mesh shows parameter region that evoked an AP response. *In vitro* threshold is overlaid as a black line (see ***D***). ***C***, same as ***B***, for half-wave-rectified sine stimuli. ***D***, ***E***, *In vitro* results. ***D*$_1$**, Stimuli (left) and current-clamp traces (right) for the ramp stimulus experiment. ***D*$_2$**, Threshold curves from individual neurons (gray traces) and their average (black, $n = 12$, same as in ***B*$_2$**). ***E***, same as ***D***, but for half-wave-rectified sine stimuli *in vitro* ($n = 8$). The data of ***B***–***E*** were normalized to the smallest amplitude that elicited an AP response in the specific cell. Error bars show the SEM.

12 MSO neurons was performed (Fig. 2*A*). Our immunostainings revealed that the AIS consisted of a 17.3 ± 1.1-μm-long ankyrin G-positive domain emerging directly from the soma and a 11.2 ± 0.6-μm-long Kv1.2-positive domain starting at 7.6 ± 0.7 μm distal from the soma in the labeled axons (Fig. 2*A*,*B*). Diameter measurements indicated that the AIS consisted of the tAIS and the cAIS. On average, the diameter of the AIS decreased from 1.6 ± 0.1 μm at the soma (position A1) to 0.6 ± 0.1 μm at the position K2, as defined in Figure 2, *B* and *C*. The length of the AIS (measured from A1 to K2; Fig. 2*B*) ranged from 14.0 to 24.0 μm (18.8 ± 1.0 μm). Adjacent to the AIS was a 2.3 ± 0.2-μm-long segment devoid of ankyrin G and Kv1.2 labeling, which we interpret as the paranodal (or para-AIS) region, where myelin is anchored to the axon (Duflocq et al., 2011; Fig. 2*A*′, arrow). The paranodal region was followed by a 2.9 ± 0.5-μm-long Kv1.2-positive domain representing the juxtaparanode (or juxtapara-AIS). The first node of Ranvier was identified based on its typical arrangement of two juxtaparanodal Kv1.2-positive domains that were separated from the nodal ankyrin G domain through unlabeled paranodes (Fig. 2*A*′). The length of the first internode ranged from ~50 to ~150 μm (100.4 ± 9.1 μm), and its mean diameter (Fig. 2*B*,*C*, measured at several positions between the two juxtaparanodal borders K3 and K6) was 0.7 ± 0.1 μm. These axonal parameters were used to constrain a computational model of the MSO neuron (Table 1).

Input–output functions

We first determined how the AP frequency of our computational neuron model is influenced by the parameters that we assumed to be most crucial for axonal excitability (AP threshold), i.e., the morphological parameters internode length, axonal diameter, proximal diameter, and tAIS length; and the electrical properties density of sodium channels in the unmyelinated axonal segments and somatic input resistance (Fig. 3). We tested how much the influence of these excitability parameters on AP probability depended on the center frequency of the bandpass stimuli (see Materials and Methods) and found that for center frequencies of ≤500 Hz all of the axonal parameters had little influence on spiking probability (Fig. 3*A*–*D*, example of internode length). For higher stimulus frequencies, the axonal parameters had distinct influences on the input–output functions. As we increased the internode length, the spiking probability generally decreased (Fig. 3*A*–*D*), which can be attributed to a reduction of the axial current flow. Geometrical alterations that increase the axonal sodium conductance (while keeping the channel density constant) mostly result in an increase of the firing rate. This increase could be observed in simulations with altered axonal diameter [keeping a constant ratio of 0.7 between the inner (axon) and outer (myelin) diameter of the internode]. The firing rate also increased with axonal diameter (Fig. 3*E*), reflecting the corresponding increase of the number of sodium channels. Also an increase of the length of the tAIS led to a higher AIS sodium

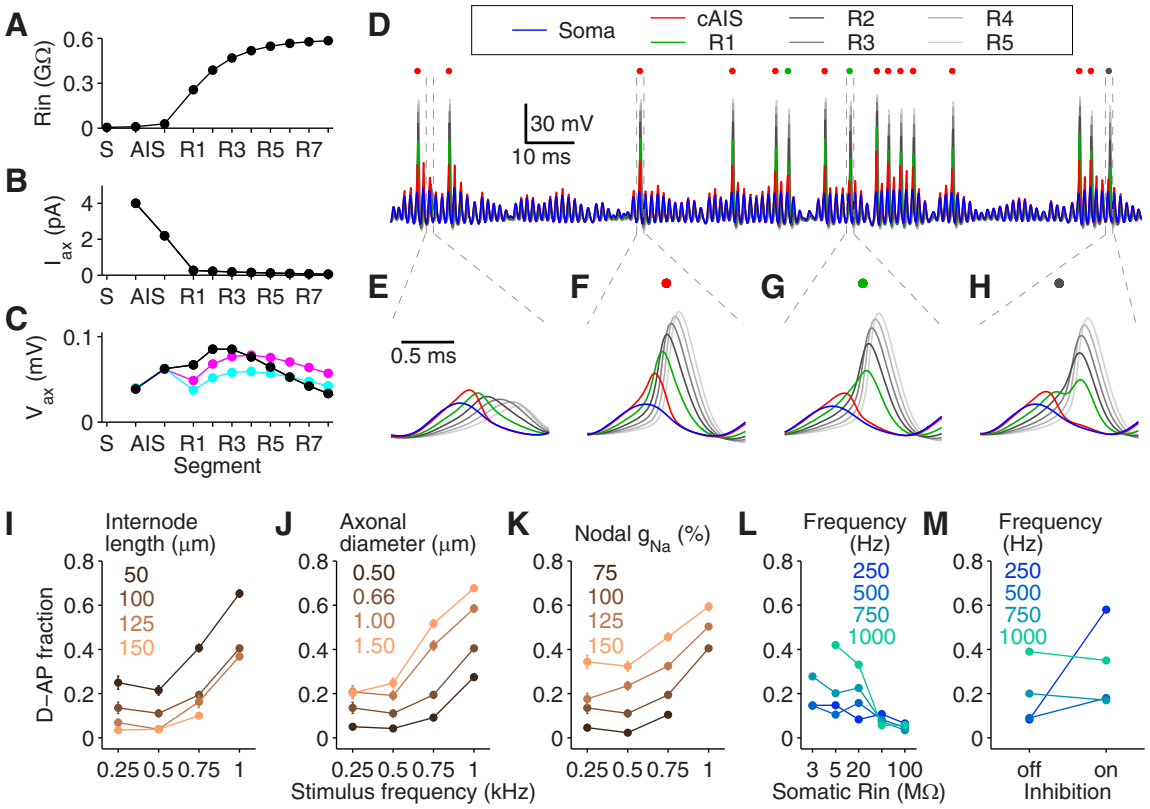

Figure 5. Distal AP initiation. ***A–C***, Local input resistance (***A***), axial current (***B***), and V_{ax} (***C***) in the different model compartments for the standard parameters (black traces), the model with shorter internode lengths of 50 μm (magenta traces), and thicker axonal diameter of 1.5 μm (cyan traces). ***D***, Exemplary voltage traces in different compartments (colors as indicated). Filled colored circles show the AP-initiating segment for each suprathreshold response (see legend). ***E–H***, Example events (from ***D***) for subthreshold response (***E***), and evoked APs generated in the AIS (***F***), R1 (***G***), and R2 (***H***). ***I–K***, Fraction of distally initiated APs (D-AP; for a fixed AP probability of 15%), with varying internode length (***I***), axonal diameter (***J***), and sodium conductance in the nodes of Ranvier (***K***). ***L***, Fraction of distally initiated APs for different somatic input resistances. ***M***, Fraction of distally initiated APs without and with inhibition for several input frequencies.

conductance and an increasing firing probability (Fig. 3*F*). In line with these findings, a direct increase in the sodium conductance in unmyelinated axonal compartments (Fig. 3*G*,*H*) also facilitated AP probabilities. However, a different effect was observed when the proximal diameter of the tAIS was decreased, which also decreased the amount of sodium conductance but, interestingly, increased AP frequency (Fig. 3*I*). This indicates that in addition to the total local sodium conductance excitability of the axon also profits from an increased electrotonic isolation from the leak currents in the soma. This interpretation was corroborated by the following two additional sets of simulations: (1) an increase of the tAIS input resistance by removing all tAIS subthreshold conductances from the equation had almost no effect on firing probability (Fig. 3*I*, inset); and (2) increasing the somatic input resistance (by multiplicative scaling of the peak conductances of KLT channel and h current, keeping a constant resting potential) strongly enhanced AP frequency (Fig. 3*J*). The MSO soma thus acts as a strong current sink for the AIS, and, hence, the axon excitability crucially depends on rather small changes of the somatic current reaching the axon.

Frequency-dependent threshold

Since the firing probabilities strongly depended on the center frequency of the inputs (Fig. 3), we performed a more systematic analysis of the frequency dependence of excitability of our computational neuron model and corroborated these data by *in vitro* measurements of MSO cells. The frequency dependence of MSO firing probability in the model was determined for a large range of bandpass stimuli with center frequencies ranging from 100 to 1250 Hz and varying stimulation intensities (Fig. 4*A*). This allows the assessment of the firing thresholds of MSO neurons with respect to both the shape (frequency content) and the amplitude of the input currents. The lowest current thresholds were observed at ~500 Hz. For higher as well as lower input frequencies, more excitatory drive was necessary to reach a certain firing probability.

To better understand the dependence of AP initiation on the input kinetics, we simulated two onset stimulation paradigms using brief current stimuli applied at rest. First, we applied a ramp stimulus for which we could independently vary amplitude and ramp duration (Fig. 4B_1). The ramp duration was assumed to serve as a proxy for stimulus shape (frequency) during the ongoing bandpass stimulation. The firing probabilities (Fig. 4B_2) obtained with these stimuli very well explained the behavior observed for low-frequency bandpass inputs, which effectively implements a slope threshold (Golding and Oertel, 2012); that is, the neuron fires in response to a specific speed of membrane depolarization that is rather independent of amplitude. Such behavior has been previously described in octopus cells (Ferragamo and Oertel, 2002), in the vestibular pathway (Beraneck et al., 2007) and the MSO (Jercog et al., 2010), and is generally attributed to the fast kinetics of the KLT channels, which are further opening only for slow stimuli and cannot generate such additional leaks for fast-rising stimuli. The high-frequency behavior of our threshold profile, however, could not be modeled using the simple ramp stimuli. We therefore also applied half-wave-rectified sine waves (Fig. 4C_1). Here again, both the low- and the high-frequency increase of threshold amplitudes was observed

(Fig. 4C_2). Thus, the threshold amplitude for high frequencies crucially depends on the duration of the stimulus. This indicated that the high-frequency part of the threshold curve reflects the limit imposed by the charging of the membrane capacitor for regimes in which the membrane voltage rises too quickly to open the low-threshold potassium channels (Jercog et al., 2010). These modeling results were verified physiologically using whole-cell current-clamp recordings using the same stimuli as in the model (see Materials and Methods). From the recorded data obtained with the ramp stimuli, the AP probability was fitted by a sigmoid for each ramp duration as a function of the amplitude using at least 10 consecutive trials. The amplitude at which the fit was at 50% AP probability was defined as the threshold. The physiologically obtained threshold curves qualitatively matched the modeling results for the ramp-current stimuli (Fig. 4B_2, superimposed black trace, *D*) with less firing for slow-input ramps and secure responses for faster ramps. For the half-wave-rectified sine stimuli, threshold amplitudes were obtained by manual testing (Fig. 4C_2, superimposed black trace, *E*) and also qualitatively matched the simulations with the lowest firing threshold for medium frequencies and less firing for low and high frequencies. From these simulations and experiments, we concluded that the threshold behavior observed during ongoing stimulation is functionally very similar to that in onset-like stimulus paradigms with single current pulses.

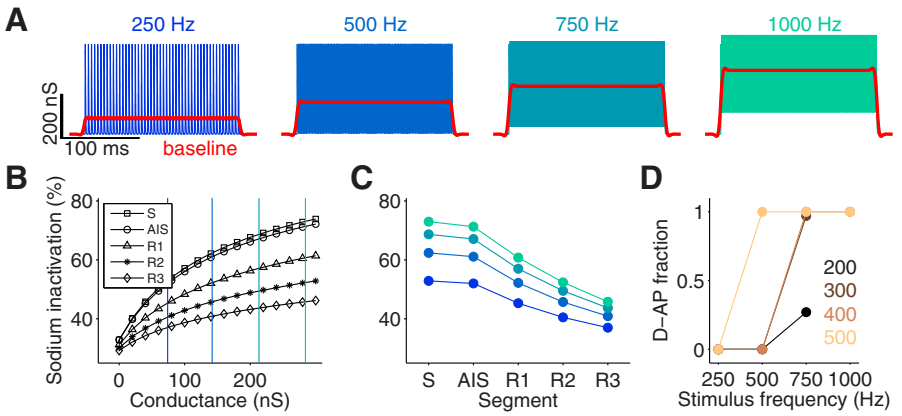

Figure 6. High input frequencies cause sodium channel inactivation in the somatic and proximal axonal membranes. ***A***, Periodic synaptic conductances with a peak value of 400 nS for center frequencies of 250, 500, 750, and 1000 Hz. Red traces are obtained by low-pass filtering the voltage traces (cutoff frequency, 100 Hz). ***B***, Steady-state sodium channel inactivation measured in different model compartments for increasing excitatory conductances. ***C***, Steady-state sodium channel inactivation for traces (color coded) in ***A*** in different compartments. ***D***, Fraction of distally initiated APs (D-APs) for input traces in ***A*** with different conductance peak values (color coded; in nS).

Site of AP initiation

Although AP initiation might be functionally similar under onset and ongoing stimulus conditions, the underlying mechanisms may be different, since, owing to the temporal summation of the inputs, the ongoing stimulation sets the cell membrane into a state that is very different from resting conditions (e.g., because of steady-state activation of channels and changes in input resistance). We therefore investigated AP initiation during ongoing stimulation in greater detail. In particular, we were interested in the contributions of the different cellular (somatic and axonal) compartments to the generation of APs.

A first assessment of the local excitability of the model neuron was derived from local input resistance measurements, using small hyperpolarizing current pulses (amplitude, −100 pA for 300 ms) that were consecutively injected into the soma, the cAIS, and the nodes of Ranvier of our model at rest (Fig. 5*A*, black trace). Here, the input resistance was derived from the peak of the voltage responses and not the steady-state component to obtain a measure for the instantaneous susceptibility of the local membrane. In our model, the peak conductance parameters were chosen such that the somatic input resistance was fixed at 5 MΩ (Scott et al., 2005; Couchman et al., 2010). With the standard parameter settings (Tables 1 and 2), the AIS had two (tAIS, 9.7 MΩ) to six times (cAIS, 28.5 MΩ) the input resistance of the soma. Further distally in the axon, the R1 showed a 50-fold increase of input resistance (256.5 MΩ). We next applied a current pulse of 1 nA at the soma while at the same time extracting the peak of the axial current in the respective axonal segments (Fig. 5*B*, black trace). The portion of this current that spread from the soma into the AIS was only 0.4% (4 pA), with further attenuation at the R1 (0.3 pA). Multiplying the axial current by the local input resistance yields a measure that can be interpreted as the axonally mediated voltage amplitude (V_{ax}). This voltage amplitude was further used as an estimate for the local excitability. The axially mediated voltage amplitude was maximal at the second and third nodes of Ranvier (Fig. 5*C*, black trace). Thus, in contrast to the classical model of AP initiation at the AIS, the second and third nodes appear to be more excitable, indicating that the more distal compartments play an important role in axon excitability in leaky neurons.

A detailed analysis of AP times in the individual compartments revealed that the site of AP initiation was indeed not restricted to the AIS (Fig. 5*D–H*). Although many APs were initiated in the AIS (Fig. 5*F*,*I–K*), 5–60% (depending on input conditions) of the APs first crossed the detection threshold (see Materials and Methods) at the first (Fig. 5*G*) or even the second (Fig. 5*H*) node of Ranvier, while the AIS showed a response similar to the subthreshold case (Fig. 5*E*). The amplitudes of the somatic and AIS APs were relatively small, independent of where they were generated, and underwent subsequent amplification by the nodes of Ranvier as they orthodromically propagated along the axon (Fig. 5*F–H*).

To further elucidate the mechanisms of this distal AP initiation, we quantified its occurrence under our naturalistic ongoing input paradigm for different morphological parameters. For purely excitatory inputs, the fraction of distally initiated APs over AIS APs increased with stimulus frequency (Fig. 5*I–L*). For shorter internodes (Fig. 5*I*) and thicker axonal diameter (Fig. 5*J*), more distal APs were observed. This is because the resulting increased axial conductance allows the stimulus-evoked potential to propagate further along the axon and is also illustrated by the peak of the V_{ax} located at more distal regions of the axon in both conditions (Fig. 5*C*, cyan and magenta traces). Consistently, a higher nodal sodium conductance increased the fraction of distally initiated APs as well, because APs could be more easily initiated at the nodes (Fig. 5*K*).

A major factor influencing distal AP initiation for inputs at all center frequencies is the somatic input resistance. The prevalence of distal AP initiation is strongly reduced with the increase of input resistance of the soma (Fig. 5*L*). Hence, distal spiking

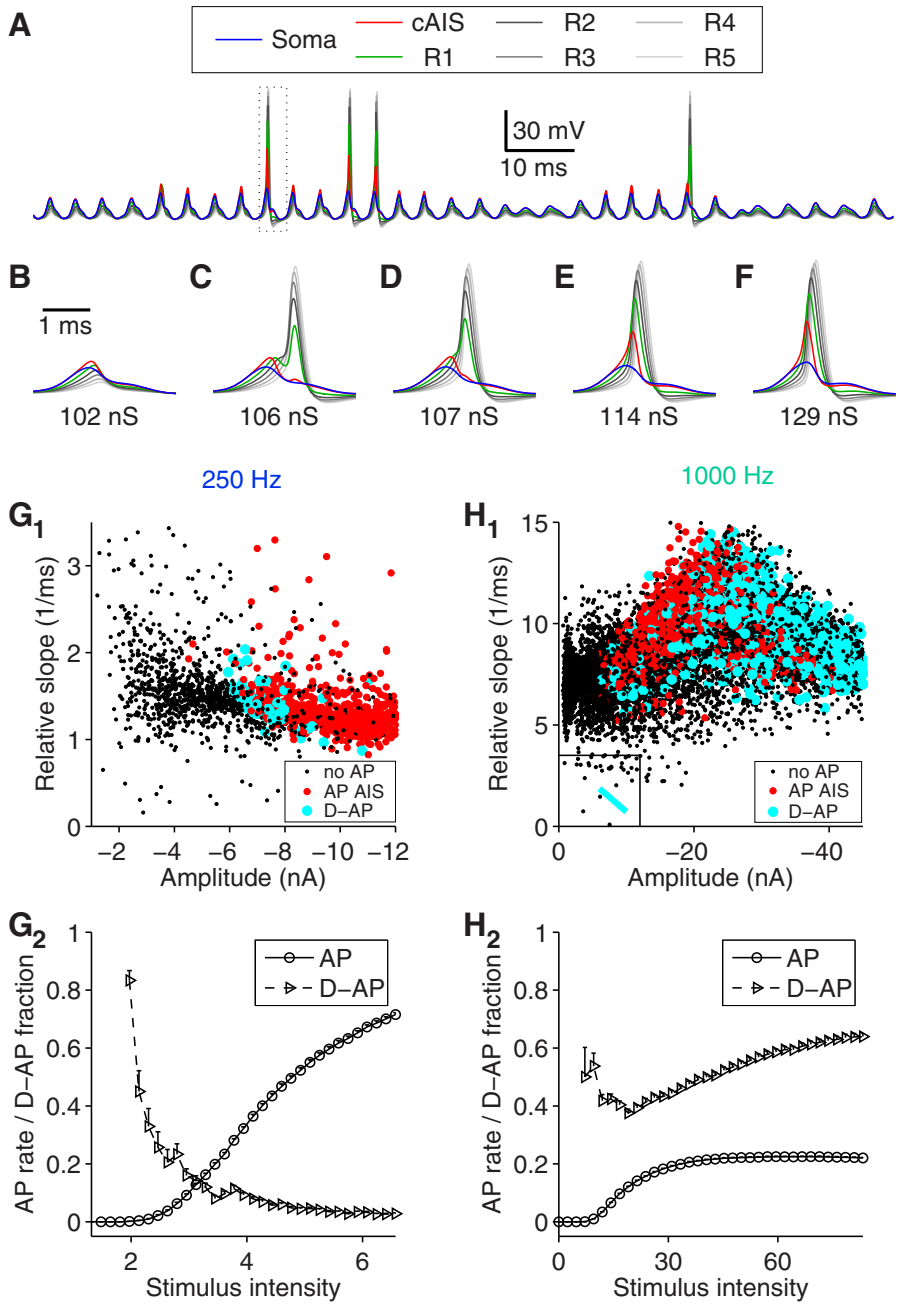

Figure 7. Function of distal AP initiation. ***A***, Example voltage traces for a stimulus with center frequency 250 Hz. The box indicates a cycle that was further investigated for different excitatory peak conductance values. ***B–F***, The selected stimulus cycle evolves from a subthreshold response (***B***), via a distally initiated AP (***C***, ***D***), to an AP initiated in the AIS (***E***, ***F***). G_1, Model responses to input trains with a center frequency of 250 Hz generate a broad range of cycle amplitudes and relative derivatives (see Materials and Methods). Each dot corresponds to a cycle within the input train. Black, Subthreshold response; red, AP response initiated in the AIS; cyan, AP response initiated in a node of Ranvier (D-AP). G_2, Firing rate and fraction of distally initiated APs for increasing excitatory synaptic conductances and an input with 250 Hz center frequency. H_1, Same as G_1 for an input with a center frequency of 1000 Hz. The cyan line in the box is a linear fit to the distally initiated APs from G_1. H_2, Same as G_2 but for inputs with 1000 Hz center frequency.

should be particularly prevalent in leaky neurons that receive fast-fluctuating inputs such as in the MSO.

Since MSO neurons not only receive excitatory inputs but also strong phase-locked inhibitory inputs via the medial and lateral trapezoid body, we also performed simulations with excitatory and inhibitory inputs. In these simulations, the frequency dependence of the site of AP initiation is less clear (Fig. 5*M*). On the one hand, the fraction of distally initiated APs also increased with frequency for center frequencies of >500 Hz. On the other hand, for a low center frequency of 250 Hz, inhibition also generated large amounts of distal AP initiation. This already indicates that distal AP initiation may result from a variety of different mechanisms, particularly also those that add to the somatic current sink.

Distal AP initiation for high-frequency inputs

The steady-state approach to axonal excitability (Fig. 5*A–C*) disregards contributions from the dynamics of the ion channels. To understand whether such dynamic properties of the neuron model also contribute to distal AP initiation, we used strictly periodic synaptic (conductance) input trains of different frequencies (Fig. 6*A*). Temporal summation of the synaptic inputs generated a conductance plateau that increased with frequency as revealed by low-pass filtering (Fig. 6*A*, second-order Butterworth low-pass filter with a cutoff frequency of 100 Hz, red traces). We then applied these average conductance values as a constant conductance to the cell and measured the corresponding steady-state sodium channel inactivation at the soma, the AIS, and the first three nodes of Ranvier (Fig. 6*B*). This revealed that a larger average conductance generally caused more sodium channel inactivation. Moreover, the conductance level was highest at the soma and decreases along the axon. Thus, a regime of a high-frequency input generates a persistent depolarization of the membrane with a larger fraction of inactivated sodium channels at the proximal axonal membranes than at the distal segments (Fig. 6*C*). As a result, this leads to a larger fraction of distal AP initiation with increased input frequency (Fig. 6*D*).

Influence of distal AP initiation on the firing threshold

To understand the functional relevance of distal AP initiation, we next investigated which input properties are particularly amenable to evoke distal APs during ongoing stimulation (Fig. 2*B–D*). We therefore repeatedly stimulated the neuron model with identical input trains for consecutively increasing mean synaptic conductances. Figure 7*A–F* shows an exemplary stimulus cycle for which, with increasing conductance, the voltage profile along the axon transitions from a completely subthreshold response (Fig. 7*B*) over an AP being initiated at the nodes of Ranvier (Fig. 7*C*,*D*) to an AP generated at the AIS (Fig. 7*E*,*F*). From these examples, it seemed that distal AP initiation is particularly prevalent at the AP threshold.

To further evaluate the threshold property of distal AP initiation, we ran the simulations using excitatory bandpass inputs of

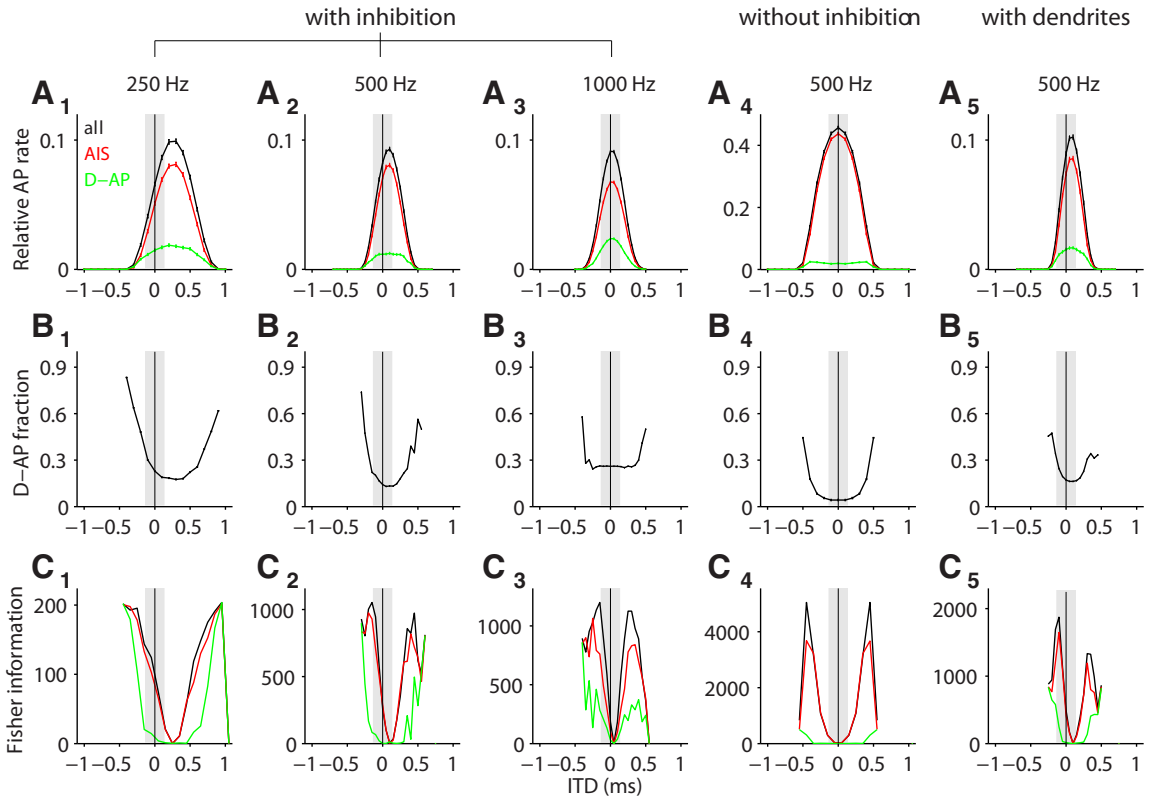

Figure 8. Representation of auditory space. ***A***, ITD tuning curves (more specifically noise delay functions; black) for input trains of 250, 500, and 1000 Hz center frequency, a purely excitatory model, and a model with dendrites (both receiving input with 500 Hz center frequency). Tuning curves without distally initiated APs are depicted in red, and tuning curves with only distally initiated APs are depicted in green. Gray bar indicates the physiological range of ITDs for gerbils. ***B***, Fraction of distally initiated APs (D-APs) of the tuning curves from ***A***. ***C***, Fisher information (in kHz^2, stimulus duration 300 ms) of the tuning curves (and the respective distal and AIS parts) from ***A***.

different center frequencies and amplitudes. For a low-frequency input with a center frequency of 250 Hz, the rate of distally initiated APs was highest right at the border between no APs and AIS APs (Fig. 7G_1,G_2). The orientation of this border was diagonal in amplitude–frequency space and qualitatively matched the AP boundaries from Figure 4 (Fig. 7G_1). For 1000 Hz, the distribution of AIS APs and distally initiated APs is different (Fig. 7H_1,H_2). There, the boundary between AP firing and no firing was approximately vertical, indicating that the cell effectively implemented an amplitude threshold being insensitive to the slope of the input current (Fig. 7H_1). Moreover, for 1000 Hz center frequency, distal AP initiation could no longer be seen as a threshold effect. In fact, after an initial dip for low amplitudes, the overall fraction of distally initiated spikes rose with input amplitude (Fig. 7H), which is in line with the dependence of the fraction of distally initiated APs on sodium inactivation from Figure 6.

In conclusion, distal AP initiation seems to have two effects. (1) If the sodium channels were only slightly inactivated, the cell is able to fire in response to smaller stimulus amplitudes than without distal initiation of APs. (2) If the sodium channels are largely inactivated (as in the case of temporally summed high-frequency input), distal AP initiation allows the cell to keep up high firing rates for high-frequency stimuli with large stimulus amplitudes.

Impact of distal AP initiation on ITD coding

The above findings have important consequences for the firing behavior of MSO cells *in vivo*. We simulated ITD tuning functions using our ongoing input paradigm with synaptic conductances derived from bandpass-filtered noise. Mimicking phase-locked auditory activity from the two ears, we split up the synaptic inputs into two channels with distinct temporal disparity for the putative ipsilateral and contralateral excitatory synapses, which, disregarding possible additional cochlear and transmission delays, we interpret as an ITD. We assumed that the cell also received phase-locked inhibitory input from both ears (from the medial and lateral nuclei of the trapezoid body) and used the inhibitory synapses to generate a maximum shift in best ITD (Brand et al., 2002; Leibold and van Hemmen, 2005; Pecka et al., 2008; Leibold, 2010). For bandpass input with a center frequency of 250 and 500 Hz, the contralateral inhibition was advanced compared with excitation by 0.8 ms, whereas the ipsilateral inhibition was delayed with respect to excitation by 0.11 ms. For these low center frequencies of the input, the model generated a rate code of ITD (Fig. 8A_1,A_2) in which firing at low rates was relatively more supported by distally initiated APs (Fig. 8B_1,B_2). This becomes obvious if one computes Fisher information as a means to assess the ITD resolution of the neuronal responses (Fig. 8C). Fisher information (resolution) is particularly high at the slopes of the tuning curves. In line with the high fractions of distally initiated APs at low firing rates (Fig. 8B), distally initiated APs also contribute a particularly large amount of information at these low rate regimes. Although, for the present definition of ITDs, these low rate parts are largely outside the physiological range (Fig. 8, gray bars), they might still become physiologically relevant if additional bilaterally asymmetric cochlear, axonal, or cellular delays exist that shift the tuning curves in parallel to the ITD axis.

To achieve the maximal peak shift for bandpass input with a center frequency of 1000 Hz, we set the contralateral inhibition to lead the excitation by 0.5 ms. The situation was very similar to

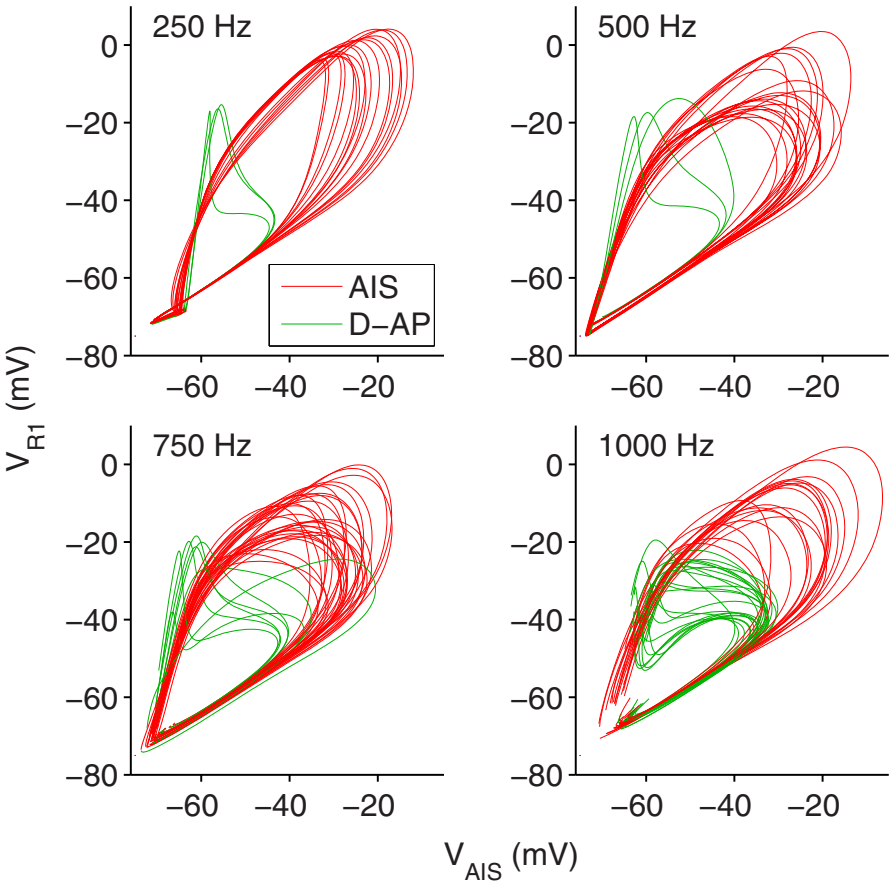

Figure 9. Is there a discrete site of AP initiation? AIS voltage vs voltage at the first node of Ranvier during AP firing for inputs with different center frequencies (as indicated). Red traces are APs identified as AIS APs by the algorithm described in Figure 1*F*. Green traces are APs classified as distally initiated (D-AP).

those for the two lower center frequencies, only that the best ITD, in contrast to *in vivo* findings (Brand et al., 2002), was close to the midline (Fig. 8A_3), and the code was mediated by distal AP initiation to an even larger extent (Fig. 8B_3). Also Fisher information was particularly high for distally initiated APs, even within the physiological range without any additional asymmetric delays (Fig. 8C_3). Thus, the realistically slow decaying inhibition (exponential decay with a time constant of 1.6 ms; Magnusson et al., 2005; Couchman et al., 2010) could well account for the observed peak shifts of low-frequency cells in gerbils, whereas it (at least alone) does not do so for frequencies of ~1 kHz and beyond (Pecka et al., 2008).

As a control, we ran the simulations without inhibitory inputs (Fig. 8A_4,B_4,C_4) which resulted in a best delay of zero. In this case, distally initiated APs were less prevalent. We thus conclude that distal AP initiation is an important mode of AP generation, particularly in the high-frequency channels but also in low-frequency channels with phase-locked inhibition.

In a final set of simulations, we tested how robust our findings are in a model that includes dendrites (Fig. 8A_5,B_5,C_5). MSO neurons typically have two dendrites, a lateral one receives ipsilateral excitatory input fibers and a medial one targeted by contralateral excitatory input fibers. We adjusted the model such that all basic physiological properties matched those of the simpler model and, hence, the published electrophysiological data (Scott et al., 2005; Couchman et al., 2010). The tuning curves and distal AP fractions from this extended model were almost identical to that of the simpler model. We thus conclude that the additional dendritic current sinks do not influence the excitability of the neuron beyond their contribution to the basic physiological parameters (input resistance, resting potential, and EPSP shape).

Discussion

In this study, we used naturalistic synaptic conductance trains to investigate AP initiation in a model of binaural coincidence detector neurons in the MSO, featuring a detailed axonal morphology. Modeling as well as electrophysiology showed that MSO cells incorporate temporal filtering properties such that they were easiest to excite for an input frequency of ~500 Hz. In contrast to current theories, the site of AP generation was not restricted to the AIS but varied depending on the spectral composition of the input. Further distally initiated APs (at the nodes of Ranvier) occurred close to the AP threshold in low-frequency channels, particularly in the presence of inhibition, as well as for strong stimulation in the high-frequency channels. Mechanistically, distal AP initiation at low frequencies was mediated by a strong somatic current sink, whereas for high frequencies it resulted from a stronger sodium channel inactivation in the AIS than in the distal axon. Importantly, in both cases, the ability of the neuron to generate APs in more distal axonal segments increased the dynamic range of firing rates. Distal AP initiation thereby facilitates the resolution of the rate code of ITDs in the cell (Skottun, 1998).

Our model simulations show that AP initiation cannot be viewed to generally occur at one specific site, but rather the proximal axonal segments act as a whole during this process. This is because the axial transport of charge particularly strongly determines the excitability of neighboring axonal segments (Baranauskas et al., 2013). To support the idea of distributed AP generation on a phenomenological level, we compared the trajectories of AIS APs and distally initiated APs plotting AIS voltage against voltage at the first node of Ranvier (Fig. 9). Although, on average, we see a clear distinction between the trajectories of the AIS and distally initiated APs, for higher stimulus frequencies the two sorts of trajectories form a continuum. This means that for some APs it is valid to assign a single site of initiation, but for others (Fig. 9, close to the border between red and green traces) it is rather difficult. A further argument in favor of spatially distributed AP generation is that the distribution of AP initiation sites in our model also depends on stimulus frequency, with high frequencies giving rise to more distal spiking (Fig. 5*I*). This finding is consistent with previous reports about layer 5 pyramidal neurons revealing that the first node of Ranvier facilitates high-frequency (>100 Hz) burst firing and reduces the somatic AP threshold by 5 mV (Kole, 2011). In summary, these results suggest that for high-frequency inputs, AP initiation of MSO cells indeed results from a spatially distributed and collective mechanism,

whereas for low-frequency inputs APs are rather generated at a distinct site.

Our computational model explains the small AP amplitudes observed *in vivo* (Yin and Chan, 1990) and *in vitro* (Scott et al., 2007; Couchman et al., 2010). However, the specific choice of parameters is crucial to further justify the model results. Whereas most of the parameters are closely tied to the existing MSO literature and the new morphometric data presented in this article, specifically the sodium conductances have not yet been determined experimentally in MSO axons. We have set the axonal sodium conductance density such that the firing threshold (70–110 nS) for a single excitatory synaptic conductance stimulus fits our current-clamp measurements (Couchman et al., 2010). Moreover, the axonal sodium conductance density of 4 nS/μm^2 used in the model lies within the range of values reported for cortical pyramidal neuron AISs (2.5 nS/μm^2, Kole et al., 2008) and has been used in several other studies (7.5 nS/μm^2, Shu et al., 2007; 4.5 nS/μm^2, Spirou et al., 2008). In our standard parameter set, we decided to use the same sodium channel density for all unmyelinated axonal compartments (the AIS and the nodes of Ranvier). This simplification rather leads to an underestimation of distal AP initiation (Fig. 5*K*). Assuming a higher sodium channel density in the nodes of Ranvier than in the axon initial segment, as shown by immunogold electron microscopy in cortical pyramidal cells (Lorincz and Nusser, 2010), relatively decreases the excitability of the AIS, thereby increasing the fraction of distally initiated APs.

In the analog ITD circuitry of birds, axonal processing has also been shown to be functionally important (Kuba et al., 2006; Ashida et al., 2007). In NL cells receiving phase-locked inputs up to 3 kHz, the AP initiation zone (clustering of sodium channels) of the AIS is located substantially more distal compared with the low-frequency neurons (Kuba et al., 2006). This finding is in line with the present observation of AP initiation moving to more distal parts of the axon for high-frequency stimuli. Compared with MSO principal neurons, which we suggest to have a dynamically changing site of AP initiation, in NL neurons the site of AP initiation seems rather hardwired, which is also supported by a partial myelination of the initial segment (Carr and Boudreau, 1993).

The mechanisms underlying ITD tuning of MSO principal neurons are highly debated (Grothe et al., 2010; Roberts et al., 2013; van der Heijden et al., 2013). Traditionally, ITD processing was thought to rely exclusively on the coincidence detection of excitatory inputs and neuronal ITD representation on the neurons that respond most at their best ITD. This best ITD is determined by the difference of internal delay lines between the ears and the coincidence detector neuron (Jeffress, 1948). While in the bird systems this concept still seems to constitute the core mechanism underlying ITD maps (Ashida and Carr, 2011), the situation in mammals is less clear. In brainstem and midbrain, the best ITDs change with stimulus frequency inconsistently with the assumption of a solely temporal conduction delay (i.e., they exhibit a so-called characteristic phase; Yin and Chan 1990, Agapiou and McAlpine, 2008, Siveke et al., 2012). Furthermore, blockade of glycinergic transmission *in vivo* shifted the best ITD of MSO neurons toward zero (Brand et al., 2002), hence arguing for a distinct effect of inhibitory inputs on the timing and shape of the excitatory potentials (Brand et al., 2002; Pecka et al., 2008) and providing a putative explanation for the frequency-dependent best ITDs (Leibold, 2010). Although it has been assumed that, given its slow kinetics, inhibition alone cannot account for a substantial shift of the best ITD (Jercog et al., 2010; Day and Semple, 2011; Roberts et al., 2013), our present modeling results show that inhibition has the potential to generate shifts as large as the physiological ITD range of gerbils ($\sim$130 μs), at least for frequencies $<$500 Hz. This, of course, does not exclude further mechanisms like cochlear or axonal delays (Schroeder, 1977; Shamma et al., 1989; Joris et al., 2006; Day and Semple, 2011) and morphological (Zhou et al., 2005; but see Rautenberg et al., 2009) or physiological (Jercog et al., 2010; but see Roberts et al., 2013) asymmetries. A further argument against a contribution of fast inhibition to the shift of best ITDs stems from recent *in vivo* whole-cell recordings (van der Heijden et al., 2013), which state a lack of obvious hyperpolarizing IPSPs. Because of the slow inhibitory time constant, our simulations show that during an ongoing stimulus IPSPs indeed do not show up as isolated potentials (Fig. 1*D*) but nevertheless influence the phase of the monaurally induced oscillations sufficiently to induce a shift of best ITDs (even for 1 kHz, although not much).

Beyond the auditory brainstem, fast and leaky cell membranes have also been reported in cortical pyramidal cells during massive synaptic bombardment such as in high-conductance states [Paré et al., 1998 (who reported input resistances as low as 4 MΩ)] and sharp wave ripple events (Bähner et al., 2011). Under both conditions, the cells show extensive spiking activity *in vivo* (Csicsvari et al., 1999; Steriade, 2001). It is thus tempting to speculate that distal AP initiation contributes to firing as well by allowing the somatic current sink to decouple from the axonal AP-generating zones in a context-dependent manner (Vladimirov et al., 2013).

References

Agapiou JP, McAlpine D (2008) Low-frequency envelope sensitivity produces asymmetric binaural tuning curves. J Neurophysiol 100:2381–2396. CrossRef Medline

Agrawal D, Hawk R, Avila RL, Inouye H, Kirschner DA (2009) Internodal myelination during development quantitated using x-ray diffraction. J Struct Biol 168:521–526. CrossRef Medline

Ashida G, Carr CE (2011) Sound localization: Jeffress and beyond. Curr Opin Neurobiol 21:745–751. CrossRef Medline

Ashida G, Abe K, Funabiki K, Konishi M (2007) Passive soma facilitates submillisecond coincidence detection in the owl's auditory system. J Neurophysiol 97:2267–2282. CrossRef Medline

Bähner F, Weiss EK, Birke G, Maier N, Schmitz D, Rudolph U, Frotscher M, Traub RD, Both M, Draguhn A (2011) Cellular correlate of assembly formation in oscillating hippocampal networks in vitro. Proc Natl Acad Sci U S A 108:E607–616. CrossRef Medline

Baranauskas G, David Y, Fleidervish IA (2013) Spatial mismatch between the Na+ flux and spike initiation in axon initial segment. Proc Natl Acad Sci U S A 110:4051–4056. CrossRef Medline

Baumann VJ, Lehnert S, Leibold C, Koch U (2013) Tonotopic organization of the hyperpolarization-activated current (Ih) in the mammalian medial superior olive. Front Neural Circuits 7:117. CrossRef Medline

Beraneck M, Pfanzelt S, Vassias I, Rohregger M, Vibert N, Vidal PP, Moore LE, Straka H (2007) Differential intrinsic response dynamics determine synaptic signal processing in frog vestibular neurons. J Neurosci 27:4283–4296. CrossRef Medline

Brand A, Behrend O, Marquardt T, McAlpine D, Grothe B (2002) Precise inhibition is essential for microsecond interaural time difference coding. Nature 417:543–547. CrossRef Medline

Carr CE, Boudreau RE (1993) An axon with a myelinated initial segment in the bird auditory system. Brain Res 628:330–334. CrossRef Medline

Couchman K, Grothe B, Felmy F (2010) Medial superior olivary neurons receive surprisingly few excitatory and inhibitory inputs with balanced strength and short-term dynamics. J Neurosci 30:17111–17121. CrossRef Medline

Csicsvari J, Hirase H, Czurkó A, Mamiya A, Buzsáki G (1999) Oscillatory coupling of hippocampal pyramidal cells and interneurons in the behaving Rat. J Neurosci 19:274–287. Medline

Day ML, Semple MN (2011) Frequency-dependent interaural delays in the

medial superior olive: implications for interaural cochlear delays. J Neurophysiol 106:1985–1999. CrossRef Medline

Duflocq A, Chareyre F, Giovannini M, Couraud F, Davenne M (2011) Characterization of the axon initial segment (AIS) of motor neurons and identification of a para-AIS and a juxtapara-AIS, organized by protein 4.1B. BMC Biol 9:66. CrossRef Medline

Ferragamo MJ, Oertel D (2002) Octopus cells of the mammalian ventral cochlear nucleus sense the rate of depolarization. J Neurophysiol 87:2262–2270. CrossRef Medline

Fitzpatrick DC, Batra R, Stanford TR, Kuwada S (1997) A neuronal population code for sound localization. Nature 388:871–874. CrossRef Medline

Ford MC, Grothe B, Klug A (2009) Fenestration of the calyx of Held occurs sequentially along the tonotopic axis, is influenced by afferent activity, and facilitates glutamate clearance. J Comp Neurol 514:92–106. CrossRef Medline

Foust A, Popovic M, Zecevic D, McCormick DA (2010) Action potentials initiate in the axon initial segment and propagate through axon collaterals reliably in cerebellar Purkinje neurons. J Neurosci 30:6891–6902. CrossRef Medline

Gentet LJ, Stuart GJ, Clements JD (2000) Direct measurement of specific membrane capacitance in neurons. Biophys J 79:314–320. CrossRef Medline

Glasberg BR, Moore BC (1990) Derivation of auditory filter shapes from notched-noise data. Hear Res 47:103–138. CrossRef Medline

Goldberg JM, Brown PB (1969) Response of binaural neurons of dog superior olivary complex to dichotic tonal stimuli: some physiological mechanisms of sound localization. J Neurophysiol 32:613–636. Medline

Golding NL, Oertel D (2012) Synaptic integration in dendrites: exceptional need for speed. J Physiol 590:5563–5569. CrossRef Medline

Grothe B, Pecka M, McAlpine D (2010) Mechanisms of sound localization in mammals. Physiol Rev 90:983–1012. CrossRef Medline

Jeffress LA (1948) A place theory of sound localization. J Comp Physiol Psychol 41:35–39. CrossRef Medline

Jercog PE, Svirskis G, Kotak VC, Sanes DH, Rinzel J (2010) Asymmetric excitatory synaptic dynamics underlie interaural time difference processing in the auditory system. PLoS Biol 8:e1000406. CrossRef Medline

Joris PX, Van de Sande B, Louage DH, van der Heijden M (2006) Binaural and cochlear disparities. Proc Natl Acad Sci U S A 103:12917–12922. CrossRef Medline

Kapfer C, Seidl AH, Schweizer H, Grothe B (2002) Experience-dependent refinement of inhibitory inputs to auditory coincidence-detector neurons. Nat Neurosci 5:247–253. CrossRef Medline

Koch U, Braun M, Kapfer C, Grothe B (2004) Distribution of HCN1 and HCN2 in rat auditory brainstem nuclei. Eur J Neurosci 20:79–91. CrossRef Medline

Kole MH (2011) First node of Ranvier facilitates high-frequency burst encoding. Neuron 71:671–682. CrossRef Medline

Kole MH, Letzkus JJ, Stuart GJ (2007) Axon initial segment Kv1 channels control axonal action potential waveform and synaptic efficacy. Neuron 55:633–647. CrossRef Medline

Kole MH, Ilschner SU, Kampa BM, Williams SR, Ruben PC, Stuart GJ (2008) Action potential generation requires a high sodium channel density in the axon initial segment. Nat Neurosci 11:178–186. CrossRef Medline

Kuba H, Ishii TM, Ohmori H (2006) Axonal site of spike initiation enhances auditory coincidence detection. Nature 444:1069–1072. CrossRef Medline

Leibold C (2010) Influence of inhibitory synaptic kinetics on the interaural time difference sensitivity in a linear model of binaural coincidence detection. J Acoust Soc Am 127:931–942. CrossRef Medline

Leibold C, van Hemmen JL (2005) Spiking neurons learning phase delays: how mammals may develop auditory time-difference sensitivity. Phys Rev Lett 94:168102. CrossRef Medline

Lorincz A, Nusser Z (2010) Molecular identity of dendritic voltage-gated sodium channels. Science 328:906–909. CrossRef Medline

Magnusson AK, Kapfer C, Grothe B, Koch U (2005) Maturation of glycinergic inhibition in the gerbil medial superior olive after hearing onset. J Physiol 568:497–512. CrossRef Medline

Mainen ZF, Sejnowski TJ (1996) Influence of dendritic structure on firing pattern in model neocortical neurons. Nature 382:363–366. CrossRef Medline

Mainen ZF, Joerges J, Huguenard JR, Sejnowski TJ (1995) A model of spike initiation in neocortical pyramidal neurons. Neuron 15:1427–1439. CrossRef Medline

Mathews PJ, Jercog PE, Rinzel J, Scott LL, Golding NL (2010) Control of submillisecond synaptic timing in binaural coincidence detectors by K(v)1 channels. Nat Neurosci 13:601–609. CrossRef Medline

McIntyre CC, Richardson AG, Grill WM (2002) Modeling the excitability of mammalian nerve fibers: influence of afterpotentials on the recovery cycle. J Neurophysiol 87:995–1006. Medline

McIntyre CC, Grill WM, Sherman DL, Thakor NV (2004) Cellular effects of deep brain stimulation: model-based analysis of activation and inhibition. J Neurophysiol 91:1457–1469. CrossRef Medline

Palmer LM, Stuart GJ (2006) Site of action potential initiation in layer 5 pyramidal neurons. J Neurosci 26:1854–1863. CrossRef Medline

Palmer LM, Clark BA, Gründemann J, Roth A, Stuart GJ, Häusser M (2010) Initiation of simple and complex spikes in cerebellar Purkinje cells. J Physiol 588:1709–1717. CrossRef Medline

Paré D, Shink E, Gaudreau H, Destexhe A, Lang EJ (1998) Impact of spontaneous synaptic activity on the resting properties of cat neocortical pyramidal neurons In vivo. J Neurophysiol 79:1450–1460. Medline

Pecka M, Brand A, Behrend O, Grothe B (2008) Interaural time difference processing in the mammalian medial superior olive: the role of glycinergic inhibition. J Neurosci 28:6914–6925. CrossRef Medline

Popovic MA, Foust AJ, McCormick DA, Zecevic D (2011) The spatiotemporal characteristics of action potential initiation in layer 5 pyramidal neurons: a voltage imaging study. J Physiol 589:4167–4187. CrossRef Medline

Rautenberg PL, Grothe B, Felmy F (2009) Quantification of the three-dimensional morphology of coincidence detector neurons in the medial superior olive of gerbils during late postnatal development. J Comp Neurol 517:385–396. CrossRef Medline

Roberts MT, Seeman SC, Golding NL (2013) A mechanistic understanding of the role of feedforward inhibition in the mammalian sound localization circuitry. Neuron 78:923–935. CrossRef Medline

Rothman JS, Manis PB (2003) The roles potassium currents play in regulating the electrical activity of ventral cochlear nucleus neurons. J Neurophysiol 89:3097–3113. CrossRef Medline

Schroeder MR (1977) New viewpoints in binaural interactions. In: Psychophysics and physiology of hearing (Evans EF, Wilson JP, eds), pp 455–467. New York: Academic.

Scott LL, Mathews PJ, Golding NL (2005) Posthearing developmental refinement of temporal processing in principal neurons of the medial superior olive. J Neurosci 25:7887–7895. CrossRef Medline

Scott LL, Hage TA, Golding NL (2007) Weak action potential backpropagation is associated with high-frequency axonal firing capability in principal neurons of the gerbil medial superior olive. J Physiol 583:647–661. CrossRef Medline

Scott LL, Mathews PJ, Golding NL (2010) Perisomatic voltage-gated sodium channels actively maintain linear synaptic integration in principal neurons of the medial superior olive. J Neurosci 30:2039–2050. CrossRef Medline

Shamma SA, Shen NM, Gopalaswamy P (1989) Stereausis: binaural processing without neural delays. J Acoust Soc Am 86:989–1006. CrossRef Medline

Shu Y, Duque A, Yu Y, Haider B, McCormick DA (2007) Properties of action-potential initiation in neocortical pyramidal cells: evidence from whole cell axon recordings. J Neurophysiol 97:746–760. CrossRef Medline

Siveke I, Leibold C, Schiller E, Grothe B (2012) Adaptation of binaural processing in the adult brainstem induced by ambient noise. J Neurosci 32:462–473. Medline

Skottun BC (1998) Sound location and neurons. Nature 393:531. CrossRef Medline

Spirou GA, Chirila FV, von Gersdorff H, Manis PB (2008) Heterogeneous Ca2+ influx along the adult calyx of held: a structural and computational study. Neuroscience 154:171–185. CrossRef Medline

Steriade M (2001) Impact of network activities on neuronal properties in corticothalamic systems. J Neurophysiol 86:1–39. Medline

Stuart GJ, Sakmann B (1994) Active propagation of somatic action poten-

tials into neocortical pyramidal cell dendrites. Nature 367:69–72. CrossRef Medline

Stuart G, Schiller J, Sakmann B (1997) Action potential initiation and propagation in rat neocortical pyramidal neurons. J Physiol 505:617–632. CrossRef Medline

Svirskis G, Kotak V, Sanes DH, Rinzel J (2002) Enhancement of signal-to-noise ratio and phase locking for small inputs by a low-threshold outward current in auditory neurons. J Neurosci 22:11019–11025. Medline

van der Heijden M, Lorteije JA, Plauška A, Roberts MT, Golding NL, Borst JG (2013) Directional hearing by linear summation of binaural inputs at the medial superior olive. Neuron 78:936–948. CrossRef Medline

Vladimirov N, Tu Y, Traub RD (2013) Synaptic gating at axonal branches, and sharp-wave ripples with replay: a simulation study. Eur J Neurosci 38:3435–3447. CrossRef Medline

Werthat F, Alexandrova O, Grothe B, Koch U (2008) Experience-dependent refinement of the inhibitory axons projecting to the medial superior olive. Dev Neurobiol 68:1454–1462. CrossRef Medline

Yin TC, Chan JC (1990) Interaural time sensitivity in medial superior olive of cat. J Neurophysiol 64:465–488. Medline

Zhou Y, Carney LH, Colburn HS (2005) A model for interaural time difference sensitivity in the medial superior olive: interaction of excitatory and inhibitory synaptic inputs, channel dynamics, and cellular morphology. J Neurosci 25:3046–3058. CrossRef Medline

4 Discussion

At a first glance, the two studies that have been presented here, have little in common. They represent two completely different brain areas and circuits, with extremely different functions. Nevertheless, principal cells in the medial superior olive (MSO) as well as pyramidal neurons in the hippocampus (HC) share some profoundly similar properties. In the following I will highlight a selection of these and discuss their impact on the presented studies. Unless stated otherwise, the results are obtained from experiments with rodents, typically mice or rats, or in the case of MSO studies gerbils.

To begin with, I will give an overview of the most important discussion points of each study separately. Afterwards, I will discuss the impact of high-conductance states in the information processing of single neurons and on the network level. This topic leads to an analysis of the influence of dendritic integration.

4.1 Summary of Study 1

Many studies suggest a tight link between memory formation and the HC. In our study, we focus on SWR, large voltage deflections, visible in the LFP, which are accompanied by fast, bursting oscillations. In the living animal, they mainly occur during quiet wakefulness and sleep. SWR are thought to be important in memory consolidation. In this work (see Chapter 2), we focus on the memory capacity of SWR.

Therefor, we created two different models of a CA1 pyramidal neuron, an one compartmental leaky-integrate and fire model, and a biophysically inspired

Hodgkin-Huxley type model. We used physiological, compound postsynaptc currents (cPSCs) as inputs, recreated from *in vitro* slice recordings (Maier et al., 2011). These inputs allowed us to investigate memory capacity of single ripple cycles in a continuous time space. Former studies mainly treated a ripple cycle as one discrete event in time (Kammerer et al., 2013).

To begin with, we studied the impact on spiking at a specific cycle with respect to the activity in the preceding ripple cycle. Unaltered reconstructed, excitatory cPSCs were modified such that at the beginning of the experiment the PSCs at selected cycle were deleted. Instead as average PSC was inserted, which amplitude was increased until an AP was elicited. We could not observe a strong effect of preceding activity on spike timing at the following cycle. The amplitudes of our conductances appear not to be sufficiently high. We conclude that most of the cPSCs serve as a form of noisy background activity. Thus, this finding allowed us to treat each ripple cycle as an individual unit for pattern association.

To study the memory capacity of a single ripple cycle, artificial cPSCs were created. We fixed the duration of one ripple event to 7 cycles and defined the 4th cycle to be our signal cycle, at which we expected the generation of APs. All other cycles were treated, as noise cycles, in accordance with our first finding. Setting of the synaptic weights depended on the activity during signal pattern. We varied the number of ripple inputs, and measured the ability of the neuron to retrieve those. Large numbers of ripple patterns could only be restored in the case of sparse coding in the inputs.

As our biophysical model relied on parameters drawn from observations made in *in vitro* recordings, we applied the same learning paradigm in a leaky-integrate and fire neuron. This gave us control over the spiking threshold. In each trial we determined the threshold such that the output firing rate resembled the input rate. When only excitation was applied, the results match the findings in the biophysical model. However, adding inhibition improves the memory capacity for larger numbers of patterns, although to a small extent. Thus, threshold adaptation as well as excitation, accompanied by inhibition, are necessary requirements,to improve memory retrieval.

4.2 Summary of Study 2

The MSO is known for its importance in interaural time difference (ITD) processing. Despite the very low input resistance of MSO neurons, they can generate and sustain very high firing rates. How this works is still unclear and thus, we try to give more insights into the topic of action potential (AP) initiation in the principal MSO neurons (Lehnert et al., 2014).

The main core of this study (see Chapter 3) is a biophysically inspired multicompartment model of a binaural coincidence detection neuron featuring a very detailed axonal segment. The synaptic conductance inputs were created based on experimental findings. The study could show that AP initiation is possible at different locations along the axon and not only at the axonal initial segment (AIS). Thereby, the exact position of the initiation appears to be dependent on the spectral profile of the used input. Especially high frequency inputs seem to be able to generate APs at distal parts of the axon. In contrast, low frequency inputs appear to be more restricted to initiate APs in the region of the AIS. The possibility of generating APs at different locations might have a profound impact on the integration of inputs.

Two major effects have to be mentioned which are possibly ascribed to the flexible AP initiation site. First, high stimulus amplitudes are able to keep high firing rates, despite the large excitement. And second, it is more likely to generate APs using small stimulus amplitudes.

Both of these findings play a key role in keeping the high precision in the rate code of ITDs.

Adding inhibition, enhances the occurrence of APs to appear more distal.

Another very unique feature in our study is the chosen sodium conductance density used in the axonal segments. In contrast to other parameters, the actual values do not come from direct electrophysiological recordings. As such experiments haven't been conducted, the value for the sodium conductance was inferred from current-clamp experiments. It was known which excitatory conductance trace should elicit an AP. Thus, the sodium conductance density was adjusted such that a conductance trace evokes an AP.

4.3 The impact of a high-conductance state

The typical or not so typical neuron

Due to their shape, pyramidal neurons are often used to depict a standard 'textbook neuron' (see, e.g., Abbott and Dayan (2001) as a reference for classical information transfer in a single neuron). In this classical view, a pyramidal neuron consists of a highly branching dendrite and a single axon, typically drawn on the opposite of the dendrite. The described shape goes back to the first drawings of cortical neurons from Cajal in 1911 (Cajal, 1911).
In textbooks this setting is used to explain the input-output behavior in a single neuron. Signal processing in this traditional view takes the following steps. Synapses target the dendrite. Any input travels from the dendrites, through the soma to the axon. In case of a strong enough input, an AP will be generated at the axon hillock or axon nodes, which travels along the axon to target via a synapse the next neuron and the transfer can start over again.
And indeed, this type of pyramidal neuron has been described in the HC. But over the years of studying the cortex, a whole variety of pyramidal neurons, with respect to their shape, was found. Not to mention the huge diversity of neurons in general, which ranges from extensive branching axons in neocortical interneurons to Purkinje cells in the cerebellum with two highly branching dendrites, and all possible variations in between those two examples (Parekh and Ascoli, 2013). It is still unclear how much impact the actual shape of each individual neuron has on the overall integration of information in neuronal networks. Additionally, the effects on the integration of inputs at single cell level are most uncertain, as well. Thome et al. (2014) started looking into this topic inside the hippocampal framework. They unraveled the finding that a huge portion of pyramidal neurons in the region CA1 have axon-carrying dendrites (AcDs). As already explained, the classical view would be that the axon emerges from an AIS attached to the soma. Here, the axon is linked to the soma via a small dendritic compartment. Thome et al. (2014) described effects on the AP generation. AcD neurons tend to exhibit more dendritic spikes. When a current input is injected into an AcD a lower threshold is needed to elicit an AP in comparison to an injection into a normal dendrite.

Thus, altering the form of a neuron comes along with profound changes in electrical properties. On the one hand, this can be simply explained from the geometrical properties. Here, cable theory applies, which is basically the attempt to describe the current flow in a passive neuron through mathematical equations. Therefore, the neuron is theoretically subdivided in cylindrical units with certain values for their resistance and capacitance (Hodgkin and Huxley, 1952). On the other hand, the distribution of ion channels in the membrane has a high impact on the electrophysiological properties of a neuron.

The properties of neurons are mainly gained through stainings of slices or recordings in the latter, so called *in vitro* recordings. The big advantage of slice recordings, in contrast to *in vivo* recordings, is the high control over external parameters, like temperature or ions in the surrounding fluid. In theory, this should allow for a good reproducibility, in case of performing experiments under the same conditions. Unfortunately, this aim is in reality more difficult, e.g., due to parameters which cannot be easily controlled, like atmospheric pressure or temperature in the laboratory, among many others.

But, *in vitro* recordings lack a very important feature, which was neglected for a long time. Namely the existence of a fully functioning neuronal network, the cell of interest is embedded in. This is especially important when considering that the cerebral cortex is known for its very dense connectivity, with one cell receiving inputs from several thousand synapses. Thus, by cutting those connections one can expect a huge effect on the overall activity of the neurons.

One key difference between *in vitro* and *in vivo* recordings, I want to focus on, is the input resistance. Interestingly, *in vitro* recordings go along with higher values for the input resistance than *in vivo* recordings. Moreover, the input resistance in *in vivo* recordings highly depends on the behavior of the animal. A supplementary point, which will be discussed later. Additionally, I also want to highlight the influence of higher conductances in precise temporal processing in MSO cells.

Impact of a high-conductance state

Conductance describes how well a current travels through a medium, and it is the inverse of the resistance. Thus, it is equivalent to talk about low resistance

instead of high conductance.

In neurons the conductance plays a crucial role for their excitability, thereby affecting the spiking behavior of the cells, i.e., altering the neural code. Before I go into details about the effects of changes in the resistance, I want to briefly introduce the notion of neural code, which resembles a bit my description of a ”textbook” neuron from above.

The process of information transfer through the brain can be called neural coding. The first clear definition of this term was given in a report from a work session in 1968. Here, the participants subdivided neural coding into 4 parts (Bullock, TH and Perkel, 1968). The coding starts with the generation of information *(1)*. This information can then be transformed *(2)* and transmitted *(3)*. As a last step the receiver has to interpret it *(4)*. The aim of this is a reliable transmission of information through the neuronal system. Interestingly, the participants already concluded that computational simulations of neurons have a big advantage in comparison to *in vitro* experiments. Simulations allow to control the effect of surrounding cells with a high level of detail and thereby mimicking the real environment of a cell.

Neurons with a low input resistance, equal to a high-conductance state, are characterized by a variety of properties (for a review see Destexhe et al. (2003)).

As previously mentioned, high-conductances allow for an increased temporal precision in firing. By analyzing the response time of a cell with respect to a current step inserted into the soma, the membrane time constant can be measured (Destexhe and Paré, 1999). It was shown that a higher conductance comes with a reduced membrane time constant. The smaller time constant is responsible for different effects. Among others, the ability to effectively resolve inputs exhibiting high frequencies has to be mentioned (Rudolph and Destexhe, 2003). The presented effect is assumed to be crucial for the high resolution needed in processing auditory cues.

Another consequence, resulting from a low resistance, is an altered responsiveness of the neuron. An increased conductance reinforces the responsiveness of a neuron (Paré et al., 1998; Zerlaut and Destexhe, 2017). It has to be noted that this is not the case with a constant high conductance, but rather a fluctuation is needed. Otherwise, the effect is reversed, i.e., the responsiveness is reduced. To

achieve this enhancement effect, a balanced synaptic bombardment with respect to excitation and inhibition is needed (Shu et al., 2003). A prominent example for this extreme increase of synaptic activity are UP states during slow-wave sleep (Steriade et al., 2001). Especially, in contrast to their counterpart, the DOWN states, where activity levels are low. Shu et al. (2003) used this framework to study the effects on a single cell exposed to this synaptic barrage. It appears that UP states allow for an easier generation of AP with a small number of inputs. Additionally, the authors attribute the creation of context, e.g., attention, to the high synaptic background activity. Fast changes between different states are possible. In contrast to changes in modulatory transmitters, tuning on and off of the synaptic barrage is rather quick. Thereby, making it the perfect choice to switch between different network states, depending on the situation.
Moreover, high conductance-states have impact on the effectiveness of synaptic inputs with respect to their entry location at the dendrite (Destexhe et al., 2003).
Last, I want to mention the impact of high-conductance state on the temporal integration of input signals. This specific condition seems to allow for switching between different coding strategies, e.g., between a firing-rate based coding strategy and coincidence detection (Perkel and Holmes Bullock, 1968). Different coding strategies have an impact on the spike synchrony and the degree to which this synchrony can be kept from one neuron to the next (Ratté et al., 2013).
Already the chosen selection of consequences, high-conductance states can have in neurons, makes clear how much impact they do have. The above section was kept more generic and not all of the described observations can be applied to neurons in general, and in particular to hippocampal pyramidal or principal MSO neurons. Thus, in the following, I try to examine the impact of this state on the two mentioned cell types. A conclusion that can be drawn from all of these effects is the general phenomenon of cells being more ore less stochastic in their responses. This can be explained by the huge barrage of synaptic inputs the cells receive during the high-conductance states.

Hippocampus. As it is apparent from the paragraph above, high-conductance influences the cell in several ways. Specifically in the HC, the following observa-

tions have been made.

In a study from 2001, Stacey and Durand (2001) performed slice recordings of CA1 pyramidal neurons. They injected current pulses into the Schaffer collaterals. To generate synaptic noise, they placed an electrode nearby the CA3 region and applied a long current pulse. Modulating the noise influenced the capability of detecting subthreshold activity in CA1 neurons. To be more precise, noise improves the ability of doing so. Moreover, they also suggest that this barrage of synaptic input could also be used to get over the effect of attenuation, seen in passive dendrites (Stacey and Durand, 2000). Thus, signal detection in general seems to largely benefit from enhanced noise. It seems that increasing the background activity, leads to an enhancement of random spiking, which in turn decreases the signal to noise ratio (Stacey and Durand, 2001)

Hô and Destexhe (2000) focused their simulation study of neocortical pyramidal neurons on the different components of background activity. Next to a tonically active conductance, voltage fluctuations are important to be observed. Especially these voltage fluctuations seem to account for a higher sensitivity of the cell towards subthreshold inputs.

MSO. In general, MSO neurons are, as previously mentioned, known for their extremely high temporal precision, used for sound localization. The membrane time constant of these cells is small, with values around a few hundreds of miliseconds (Scott et al., 2005). The high precision is needed for accurate coincidence detection, which is the ability to solely generate a response in the case of synchronous inputs (Ratté et al., 2013). The crucial ion channels are namely the low-threshold potassium channel Kv1 and sodium channels (Svirskis et al., 2004). The low-threshold potassium currents impact the absolute as well as the relative refractory period of the MSO neuron, together with the cation currents (Negm and Bruce, 2014). Using a computational model, Svirskis et al. (2004) could show that increasing the potassium current results in a reduced coincidence detection. Increasing the sodium current exhibited the opposite effect. Thus, the authors concluded that in order to gain a precise time window for the coincidence detection, sodium channels should be more activated and the low-threshold potassium

channels deactivated by the requested synaptic inputs.
Here, the distribution of the specific ion channels along the cell are vital as well. Mathews et al. (2010) focused on the effect of Kv1 channels. They demonstrated that in synaptic integration the time resolution can be increased by activation of Kv1 channels. Additionally, the gradient of this potassium channel allows for compensation of filter effects stemming from the passive cable properties.

Coincidence detection. The ability of a neuron to function as a coincidence detector, and thereby transforming temporal code into a rate code, relies on several factors. One major factor seems to be the integration time with respect to the interspike interval. If the integration time of a neuron is long in comparison to the interspike interval of the input, the cell can sum up the inputs and thereby acts as a temporal integrator (König et al., 1996). In contrast, coincidence detectors have a low integration time that allows the neuron to transmit signals with high temporal precision and depend on the membrane time constant (Kempter et al., 1998).
In the case of coincidence detection with subthreshold inputs, a reduced low-threshold potassium channel activity is suggested to play a key role (Svirskis et al., 2004). These potassium currents appear to be involved in the generation of membrane potential resonances (Beraneck et al., 2007) that help to intensify the subthreshold signal and thereby overcome noise (Kempter et al., 1998).
Neurons acting as coincidence detectors can be found in different brain areas. In the auditory brain stem, next to other nuclei, the MSO is known for its ability to process incoming inputs with a high temporal precision (Hermann et al., 2007). Fischer et al. (2018) argue that neurons can actively change their integration properties via these subthreshold membrane resonances and thereby serving different frequency inputs. The authors assume that in particular the leakiness of a neuron affects the resonance, a property of a cell that can dynamically change. Thereby, Fischer et al. (2018) predict that their finding is not restricted to a specific type of neuron.
Thus, also hippocampal pyramidal cells could potentially function like this. During SWR occurrence the single cell has to overcome massive background noise

and exhibits an increased membrane conductance (Prescott et al., 2006). The increased membrane conductance directly results in a decreased membrane time constant (Bernander and Koch, 1991). An effect that, similar to MSO cells, alters the integration properties of a pyramidal neuron and allows it to function as coincidence detector.

The aim of this thesis was to identify possible mechanisms, that allow neurons to perform reliable computations in high-conductance state. Hippocampal pyramidal neurons and MSO neurons proved as a good study object choice, as they are well studied and ample functional knowledge is available.
CA1 pyramidal neurons show a decrease of signal to noise ratio with enhanced noise. MSO neurons appear to change the AP generation site along the axon with increased input frequency.

References

Abbott, L. and P. Dayan (2001). Theoretical Neuroscience. *Computational and Mathematical Modeling of Neural Systems*. 22, 74

Abeles, M. (1982). Role of the cortical neuron: integrator or coincidence detector? *Israel Journal of Medical Sciences 18*(1), 83. 2

Adams, J. C. (1979). Ascending projections to the inferior colliculus. *Journal of Comparative Neurology*. 29

Amaral, D. G. (1978). A Golgi study of cell types in the hilar region of the hippocampus in the rat. *The Journal of Comparative Neurology 182*(4 Pt 2), 851–914. 6

Amaral, D. G., H. E. Scharfman, and P. Lavenex (2007). The dentate gyrus: fundamental neuroanatomical organization (dentate gyrus for dummies). *Progress in Brain Research 163*, 3–790. 6

Amaral, D. G. and M. P. Witter (1989). The three-dimensional organization of the hippocampal formation: A review of anatomical data. *Neuroscience 31*(3), 571–591. 4, 7

Andersen, P., T. V. Bliss, and K. K. Skrede (1971). Lamellar organization of hippocampal excitatory pathways. *Experimental Brain Research 13*(2), 222–238. 7

Angell, J. R. and W. Fite (1901). From the Psychological Laboratory of the Uni-

versity of Chicago: The monaural localization of sound. *Psychological Review 8*(3), 225–246. 26

Aronov, D., R. Nevers, and D. W. Tank (2017). Mapping of a non-spatial dimension by the hippocampal-entorhinal circuit. *Nature 543*(7647), 719–722. 9

Backus, A. R., J. M. Schoffelen, S. Szebényi, S. Hanslmayr, and C. F. Doeller (2016). Hippocampal-prefrontal theta oscillations support memory integration. *Current Biology 26*(4), 450–457. 14

Benson, J. B. (2020). *Encyclopedia of infant and early childhood development*. Elsevier. 6

Beraneck, M., S. Pfanzelt, I. Vassias, M. Rohregger, N. Vibert, P.-P. Vidal, L. E. Moore, and H. Straka (2007). Differential intrinsic response dynamics determine synaptic signal processing in frog vestibular neurons. *Journal of Neuroscience 27*(16), 4283–4296. 79

Bernander, O. and C. Koch (1991). Synaptic Background Activity Influences Spatiotemporal Integration in Single Pyramidal Cells. *The Biological Bulletin*. 80

Blackstad, T. W. (1956). Commissural connections of the hippocampal region in the rat, with special reference to their mode of termination. *Journal of Comparative Neurology 105*(3), 417–537. 6

Blauert, J. (1970). Sound localization in the median plane(Frequency function of sound localization in median plane measured psychoacoustically at both ears with narrow band signals). *Acustica*. 26

Bliss, T. V. and a. R. Gardner-Medwin (1973). Long-lasting potentiation of synaptic transmission in the dentate area of the unanaestetized rabbit following stimulation of the perforant path. *The Journal of Physiology 232*(2), 357–374. 21

Bramham, C. R. and B. Srebro (1987). Induction of long-term depression and potentiation by low- and high-frequency stimulation in the dentate area of the anesthetized rat: magnitude, time course and EEG. *Brain Research 405*(1), 100–107. 22

Brand, A., O. Behrend, T. Marquardt, D. McAlpine, and B. Grothe (2002). Precise inhibition is essential for microsecond interaural time difference coding. *Nature 417*(6888), 543–547. 30, 31

Brodal, A. (1947). The hypocampus and the sense of smell; a review. *Brain: A Journal of Neurology*, 179–222. 3

Brun, V. H., T. Solstad, K. B. Kjelstrup, M. Fyhn, M. P. Witter, E. I. Moser, and M. B. Moser (2008). Progressive increase in grid scale from dorsal to ventral medial entorhinal cortex. *Hippocampus 18*(12), 1200–1212. 11

Bullock, TH and Perkel, D. (1968). Neutral coding- A report based on an NRP work session(Neural coding by impulses and trains on single and multiple channels, and representation of information in nonimpulse carriers). 76

Bunsey, M. and H. Eichenbaum (1996). Conservation of hippocampal memory function in rats and humans. *Nature 379*(6562), 255–257. 4

Burgess, N., E. A. Maguire, and J. O'Keefe (2002). The human hippocampus and spatial and episodic memory. *Neuron 35*(4), 625–641. 8

Burgess, N. and J. O'Keefe (1996). Neuronal computations underlying the firing of place cells and their role in navigation. *Hippocampus 6*(6), 749–762. 11

Butler, R. A. (1986). The bandwidth effect on monaural and binaural localization. *Hearing Research*. 26

Buzsáki, G. (1989). Two-stage model of memory trace formation: a role for "noisy" brain states. *Neuroscience 31*(3), 551–570. 19

Buzsáki, G. (2015). Hippocampal sharp wave-ripple: A cognitive biomarker for episodic memory and planning. *Hippocampus 25*(10), 1073–1188. 13

Buzsáki, G., Z. Horváth, R. Urioste, J. Hetke, and K. Wise (1992). High-frequency network oscillation in the hippocampus. *Science 256*(5059), 1025–1027. 14, 33

Buzsáki, G., L. Lai-Wo S., and C. H. Vanderwolf (1983). Cellular bases of hippocampal EEG in the behaving rat. *Brain Research Reviews 6*(2), 139–171. 1, 13, 14

Cajal, S. R. (1911). Histologie du système nerveux de l'homme et des vertébrés. *Volume 2. Paris: Maloine*, 891–942. 5, 74

Cant, N. B. and J. H. Casseday (1986). Projections from the anteroventral cochlear nucleus to the lateral and medial superior olivary nuclei. *Journal of Comparative Neurology*. 28, 29

Chirila, F. V., K. C. Rowland, J. M. Thompson, and G. A. Spirou (2007). Development of gerbil medial superior olive: Integration of temporally delayed excitation and inhibition at physiological temperature. *Journal of Physiology*. 29, 30

Cohen, N. and L. Squire (1980). Preserved learning and retention of pattern analysing skill in amnesia: dossiciation of knowing how and knowing that. *Science 210*(4466), 207–210. 18

Colgin, L. L., T. Denninger, M. Fyhn, T. Hafting, T. Bonnevie, O. Jensen, M. B. Moser, and E. I. Moser (2009). Frequency of gamma oscillations routes flow of information in the hippocampus. *Nature 462*(7271), 353–357. 14

Collingridge, G. L., S. J. Kehl, and H. McLennan (1983). Excitatory amino acids in synaptic transmission in the Schaffer collateral commissural pathway of the rat hippocampus. *The Journal of Physiology 334*(1), 33–46. 21

Cornwell, B. R., L. L. Johnson, T. Holroyd, F. W. Carver, and C. Grillon (2008). Human Hippocampal and Parahippocampal Theta during Goal-Directed Spatial Navigation Predicts Performance on a Virtual Morris Water Maze. *Journal of Neuroscience 28*(23), 5983–5990. 21

Csicsvari, J., H. Hirase, A. Czurko, and G. Buzsáki (1998). Reliability and state dependence of pyramidal cell-interneuron synapses in the hippocampus: An ensemble approach in the behaving rat. *Neuron 21*(1), 179–189. 14

Csicsvari, J., H. Hirase, A. Mamiya, and G. Buzsáki (2000). Ensemble patterns of hippocampal ca3-ca1 neurons during sharp wave–associated population events. *Neuron 28*(2), 585–594. 16

Csicsvari, J., B. Jamieson, K. D. Wise, and G. Buzsáki (2003). Mechanisms of gamma oscillations in the hippocampus of the behaving rat. *Neuron 37*(2), 311–322. 14

Danjo, T., T. Toyoizumi, and S. Fujisawa (2018). Spatial representations of self and other in the hippocampus. *Science*. 10

Davis, H. P. and L. R. Squire (1984). Protein synthesis and memory: A review. *Psychological Bulletin 96*(3), 518–559. 19

Destexhe, A. and D. Paré (1999). Impact of network activity on the integrative properties of neocortical pyramidal neurons in vivo. *Journal of Neurophysiology*. 76

Destexhe, A., M. Rudolph, and D. Paré (2003). The high-conductance state of neocortical neurons in vivo. *Nature Reviews Neuroscience*. 1, 76, 77

Donoso, J. R., D. Schmitz, N. Maier, and R. Kempter (2018). Hippocampal ripple oscillations and inhibition-first network models: frequency dynamics and response to gaba modulators. *Journal of Neuroscience 38*(12), 3124–3146. 16

Douglas, R. J. (1967). The hippocampus and behavior. *Psychological Bulletin 67*(6), 416–442. 3

Draguhn, A. and G. Buzsaki (2004). Neuronal oscillations in cortical networks. *Science 304*(5679), 1926–9. 12

Draguhn, A., R. D. Traub, D. Schmitz, and J. G. R. Jefferys (1998). Electrical coupling underlies high-frequency oscillations in the hippocampus in vitro. *Nature 394*(6689), 189–192. 16, 17

Dudek, S. M., G. M. Alexander, and S. Farris (2016). Rediscovering area CA2: Unique properties and functions. *Nature Reviews Neuroscience 17*(2), 89–102. 6

Eichenbaum, H. and N. J. Cohen (2014). Can We Reconcile the Declarative Memory and Spatial Navigation Views on Hippocampal Function? *Neuron 83*(4), 764–770. 3

Eichenbaum, H., T. Otto, and N. J. Cohen (1992). The hippocampus: What does it do? *Behavioral & Neural Biology 57*(1), 2–36. 3

English, D. F., A. Peyrache, E. Stark, L. Roux, D. Vallentin, M. A. Long, and G. Buzsáki (2014). Excitation and Inhibition Compete to Control Spiking during Hippocampal Ripples: Intracellular Study in Behaving Mice. *The Journal of Neuroscience 34*(49), 16509–16517. 1

Ennaceur, A. and J. Delacour (1988). A new one-trial test for neurobiological studies of memory in rats. 1: Behavioral data. *Behavioural Brain Research 31*(1), 47–59. 20

Epsztein, J., A. K. Lee, E. Chorev, and M. Brecht (2010). Impact of Spikelets on Hippocampal CA1 Pyramidal Cell Activity During Spatial Exploration. *Science 327*(5964), 474–477. 17

Falkai, P. and B. Bogerts (1986). Cell loss in the hippocampus of schizophrenics. *European Archives of Psychiatry and Neurological Sciences 236*(3), 154–161. 6

Fischer, L., C. Leibold, and F. Felmy (2018). Resonance properties in auditory brainstem neurons. *Frontiers in Cellular Neuroscience 12*, 8. 79

Foster, D. and M. Wilson (2006). Reverse replay in hippocampal place cells during the awake state. *Nature 440*(30 March), 680–683. 17

Freund, T. and G. Buzsáki (1998). Interneurons of the hippocampus. *Hippocampus 6*(4), 347–470. 6

Friauf, E. and J. Ostwald (1988). Divergent projections of physiologically characterized rat ventral cochlear nucleus neurons as shown by intra-axonal injection of horseradish peroxidase. *Experimental Brain Research*. 28

Fuhrmann, F., D. Justus, L. Sosulina, H. Kaneko, T. Beutel, D. Friedrichs, S. Schoch, M. K. Schwarz, M. Fuhrmann, and S. Remy (2015). Locomotion, Theta Oscillations, and the Speed-Correlated Firing of Hippocampal Neurons Are Controlled by a Medial Septal Glutamatergic Circuit. *Neuron 86*(5), 1253–1264. 13

Fyhn, M., S. Molden, M. P. Witter, E. I. Moser, and M.-B. Moser (2004). Spatial representation in the entorhinal cortex. *Science 305*(5688), 1258–64. 11

Galambos, R. and H. Davis (1943). The response of single auditory-nerve fibres to acoustic stimulation. *Journal of Neurophysiology*. 29

Gan, J., S. ming Weng, A. J. Pernía-Andrade, J. Csicsvari, and P. Jonas (2017). Phase-locked inhibition, but not excitation, underlies hippocampal ripple oscillations in awake mice In vivo. *Neuron 93*(2), 308–314. 18

Gaskin, S., A. Tremblay, and D. G. Mumby (2003). Retrograde and anterograde object recognition in rats with hippocampal lesions. *Hippocampus 13*(8), 962–969. 20

Gerstner, W. and W. M. Kistler (2002). Mathematical formulations of Hebbian learning. *Biological Cybernetics 87*(5-6), 404–415. 24

Giovanello, K. S., D. Schnyer, and M. Verfaellie (2009). Distinct hippocampal regions make unique contributions to relational memory. *Hippocampus 19*(2), 111–117. 3

Girardeau, G., K. Benchenane, S. I. Wiener, G. Buzsáki, and M. B. Zugaro (2009). Selective suppression of hippocampal ripples impairs spatial memory. *Nature Neuroscience 12*(10), 1222–1223. 15, 17, 33

Girardeau, G., A. Cei, and M. Zugaro (2014). Learning-induced plasticity regulates hippocampal sharp wave-ripple drive. *Journal of Neuroscience 34*(15), 5176–5183. 15

Goelet, P., V. F. Castellucci, S. Schacher, and E. R. Kandel (1986). The long and the short of long-term memory - A molecular framework. *Nature 322*(6078), 419–422. 19

Goldberg, J. M. and P. B. Brown (1969). Response of binaural neurons of dog superior olivary complex to dichotic tonal stimuli: some physiological mechanisms of sound localization. *Journal of Neurophysiology 32*(4), 613–636. 34

Golomb, D., N. Rubin, and H. Sompolinsky (1990). Willshaw model: Associative memory with sparse coding and low firing rates. *Physical Review A 41*(4), 1843–1854. 25

Grothe, B., C. Köppl, J. H. Casseday, and C. E. Carr (2004). The evolution of central pathways and theyr neural processing patterns. In *Evolution of the Vertebrate Auditory System*, pp. 289–359. 32

Grothe, B. and M. Pecka (2014). The natural history of sound localization in mammals - a story of neuronal inhibition. *Frontiers in Neural Circuits*. 27

Grothe, B., M. Pecka, and D. McAlpine (2010). Mechanisms of Sound Localization in Mammals. *Physiological Reviews*. 28

Grothe, B. and D. H. Sanes (1993). Bilateral inhibition by glycinergic afferents in the medial superior olive. *Journal of Neurophysiology*. 31

Guinan, J. J., B. E. Norris, and S. S. Guinan (1972). Single auditory units in the superior olivary complex: II: Locations of unit categories and tonotopic organization. *International Journal of Neuroscience*. 30

Hafting, T., M. Fyhn, S. Molden, M. B. Moser, and E. I. Moser (2005). Microstructure of a spatial map in the entorhinal cortex. *Nature 436*(7052), 801–806. 4, 11

Harrison, J. M. and W. B. Warr (1962). A study of the cochlear nuclei and ascending auditory pathways of the medulla. *Journal of Comparative Neurology*. 28

Harvey, C. D., F. Collman, D. A. Dombeck, and D. W. Tank (2009). Intracellular dynamics of hippocampal place cells during virtual navigation. *Nature 461*(7266), 941–946. 9

Haukvik, U. K., L. T. Westlye, L. Mørch-Johnsen, K. N. Jørgensen, E. H. Lange, A. M. Dale, I. Melle, O. A. Andreassen, and I. Agartz (2015). In vivo hippocampal subfield volumes in schizophrenia and bipolar disorder. *Biological Psychiatry 77*(6), 581–588. 7

Hebb, D. O. . E. A. and T. J. Bussey (1949). The Organization of Behavior. Technical report. 21, 24

Heffner, R. S. and H. E. Heffner (1988). Sound Localization and Use of Binaural Cues by the Gerbil (Meriones unguiculatus). *Behavioral Neuroscience 102*(3), 422–428. 28

Held, H. (1893). Die zentrale Gehörleitung. *Arch. Anat. Physiol. Anat. Abt. 17*, 201–248. 28

Hermann, J., M. Pecka, H. von Gersdorff, B. Grothe, and A. Klug (2007). Synaptic Transmission at the Calyx of Held Under In Vivo–Like Activity Levels. *Journal of Neurophysiology 98*(2), 807–820. 29, 31, 79

Hitti, F. L. and S. A. Siegelbaum (2014). The hippocampal CA2 region is essential for social memory. *Nature 508*(1), 88–92. 8

Hô, N. and A. Destexhe (2000). Synaptic Background Activity Enhances the Responsiveness of Neocortical Pyramidal Neurons. *Journal of Neurophysiology*. 1, 78

Hodgkin, A. L. and A. F. Huxley (1952). A quantitative description of membrane current and its application to conduction and excitation in nerve. *The Journal of Physiology 117*(4), 500—-544. 23, 75

Hulse, B. K., L. C. Moreaux, E. V. Lubenov, and A. G. Siapas (2016). Membrane Potential Dynamics of CA1 Pyramidal Neurons during Hippocampal Ripples in Awake Mice. *Neuron 89*(4), 800–813. 18

Jadhav, S. P., C. Kemere, P. W. German, and L. M. Frank (2012). Awake Hippocampal Sharp-Wave Ripples Support Spatial Memory. *Science 336*(6087), 1454–1458. 15, 33

Jeffress, L. A. (1948). A place theory of sound localization. *Journal of Comparative and Physiological Psychology 41*(1), 35–39. 31

Jones, M. W. and T. J. Mchugh (2011). Updating hippocampal representations: CA2 joins the circuit. *Trends in Neurosciences 34*(10), 526–535. 8

Jouvet, M. (1969). Biogenic amines and the state of sleep. *Science 163*, 32–41. 13

Kammerer, A., Á. Tejero-Cantero, and C. Leibold (2013). Inhibition enhances memory capacity: optimal feedback, transient replay and oscillations. *Journal of Computational Neuroscience 34*(1), 125–136. 72

Kapfer, C., A. H. Seidl, H. Schweizer, and B. Grothe (2002). Experience-dependent refinement of inhibitory inputs to auditory coincidence-detector neurons. *Nature Neuroscience 5*(3), 247–253. 30, 31

Kempter, R., W. Gerstner, and J. L. Van Hemmen (1998). How the threshold of a neuron determines its capacity for coincidence detection. *Biosystems 48*(1-3), 105–112. 79

Khodagholy, D., J. N. Gelinas, and G. Buzsáki (2017). Learning-enhanced coupling between ripple oscillations in association cortices and hippocampus. *Science 358*(6361), 369–372. 20

Klausberger, T. and P. Somogyi (2008). Neuronal Diversity and Temporal Dynamics: The Unity of Hippocampal Circuit Operations. *Science 321*(5885), 53–57. 6

Klumpp, R. G. and H. R. Eady (1956). Some Measurements of Interaural Time Difference Thresholds. *The Journal of the Acoustical Society of America*. 1, 2, 27

König, P., A. K. Engel, and W. Singer (1996). Integrator or coincidence detector? the role of the cortical neuron revisited. *Trends in Neurosciences 19*(4), 130–137. 79

Kropff, E., J. E. Carmichael, M. B. Moser, and E. I. Moser (2015). Speed cells in the medial entorhinal cortex. *Nature 523*(7561), 419–424. 12

Kubota, D. (2002). Endogenous Waves in Hippocampal Slices. *Journal of Neurophysiology 89*(1), 81–89. 15

Kuwabara, N. and J. M. Zook (1992). Projections to the medial superior olive from the medial and lateral nuclei of the trapezoid body in rodents and bats. *Journal of Comparative Neurology*. 29

Lee, A. K. and M. A. Wilson (2002). Memory of sequential experience in the hippocampus during slow wave sleep. *Neuron 36*(6), 1183–1194. 9, 16

Lehnert, S., M. C. Ford, O. Alexandrova, F. Hellmundt, F. Felmy, B. Grothe, and C. Leibold (2014). Action potential generation in an anatomically constrained model of medial superior olive axons. *Journal of Neuroscience 34*(15), 5370–5384. 55, 73, 105

Leibold, C. and R. Kempter (2006). Memory capacity for sequences in a recurrent network with biological constraints. *Neural computation 18*(April), 904–941. 19

Leutgeb, S., J. K. Leutgeb, C. A. Barnes, E. I. Moser, B. L. McNaughton, and M.-B. Moser (2005). Independent codes for spatial and episodic memory in hippocampal neuronal ensembles. *Science (New York, N.Y.) 309*(5734), 619–23. 9

Lever, C., S. Burton, A. Jeewajee, J. O'Keefe, and N. Burgess (2009). Boundary vector cells in the subiculum of the hippocampal Formation. *Journal of Neuroscience 29*(31), 9771–9777. 11

Lisman, J. E. (1999). Relating hippocampal circuitry viewpoint to function: recall of memory sequences by reciprocal dentate–CA3 interactions. *Neuron 22*, 233–242. 7

Maier, N., Á. Tejero-Cantero, A. L. Dorrn, J. Winterer, P. S. Beed, G. Morris, R. Kempter, J. F. A. Poulet, C. Leibold, and D. Schmitz (2011). Coherent Phasic Excitation during Hippocampal Ripples. *Neuron 72*(1), 137–152. 15, 17, 18, 33, 72

Maki, K. and S. Furukawa (2005). Acoustical cues for sound localization by the Mongolian gerbil, Meriones unguiculatus. *The Journal of the Acoustical Society of America*. 27

Mathews, P. J., P. E. Jercog, J. Rinzel, L. L. Scott, and N. L. Golding (2010). Control of submillisecond synaptic timing in binaural coincidence detectors by Kv1 channels. *Nature Neuroscience 13*(5), 601–609. 79

McNaughton, B. L. and R. G. M. Morris (1987). Hippocampal synaptic enhancement and information storage within a distributed memory system. *Trends in Neurosciences 10*(10), 408–415. 7

Memmesheimer, R.-M. (2010). Quantitative prediction of intermittent high-frequency oscillations in neural networks with supralinear dendritic interactions. *Proceedings of the National Academy of Sciences of the United States of America 107*(24), 11092–11097. 16

Middlebrooks, J. C. and D. M. Green (1991). Sound localization by human listeners. *Annual Review of Psychology*. 27

Miles, R. M., C. Le Duigou, J. Simonnet, M. Telenczuk, and D. Fricker (2014). Recurrent synapses and circuits in the ca3 region of the hippocampus: an associative network. *Frontiers in Cellular Neuroscience 7*, 262. 7

Milner, B. (1972). Disorders of learning and memory after temporal lobe lesions in man. *Clinical Neurosurgery 19*, 421–446. 3

Milner, B., S. Corkin, and H. L. Teuber (1968). Further analysis of the hippocampal amnesic syndrome: 14-year follow-up study of H.M. *Neuropsychologia 6*(3), 215–234. 3

Morris, G. M. (1981). Spatial localization does not require local cues the presence of local cues. *Learning and Motivation 12*, 239–260. 20

Morris, R. (1984). Developments of a water-maze procedure for studying spatial learning in the rat. *Journal of Neuroscience Methods 11*(1), 47–60. 20

Nasrallah, K., R. a. Piskorowski, and V. Chevaleyre (2015). Inhibitory plasticity permits the recruitment of CA2 pyramidal neurons by CA3. *eNeuro 2*(August), 1–12. 8

Nasrallah, K., R. A. Piskorowski, and V. Chevaleyre (2017). Bi-directional interplay between proximal and distal inputs to CA2 pyramidal neurons. *Neurobiology of Learning and Memory 138*, 173–181. 8

Negm, M. H. and I. C. Bruce (2014). The effects of HCN and KLT ion channels on adaptation and refractoriness in a stochastic auditory nerve model. *IEEE Transactions on Biomedical Engineering*. 78

O' Keefe, J. and N. Burgess (1996). Geometric determinants of the place fields of hippocampal neurons. *Nature 381*(6581), 425–428. 11

O'Keefe, J. and J. Dostrovsky (1971). The hippocampus as a spatial map. Preliminary evidence from unit activity in the freely-moving rat. *Brain Research 34*(1), 171–175. 4, 8

O'Keefe, J. and L. Nadel (1978). Hippocampus physiology. *The Hippocampus as a Cognitive Map* (1), 141–230. 4, 9

Oldfield, S. R. and S. P. Parker (1986). Acuity of sound localisation: a topography of auditory space. III. Monaural hearing conditions. *Perception*. 26

Olton, D. S. and R. J. Samuelson (1976). Remembrance of places passed: Spatial memory in rats. *Journal of Experimental Psychology: Animal Behavior Processes 2*(2), 97–116. 21

Omer, D. B., S. R. Maimon, L. Las, and N. Ulanovsky (2018). Social place-cells in the bat hippocampus. *Science (New York, N.Y.) 359*(6372), 218–224. 9, 10

Pangalos, M., J. R. Donoso, J. Winterer, A. R. Zivkovic, R. Kempter, N. Maier, and D. Schmitz (2013). Recruitment of oriens-lacunosum-moleculare interneurons during hippocampal ripples. *Proceedings of the National Academy of Sciences 110*(11), 4398–4403. 17

Paré, D., E. Shink, H. Gaudreau, A. Destexhe, and E. J. Lang (1998). Impact of spontaneous synaptic activity on the resting properties of cat neocortical pyramidal neurons in vivo. *Journal of Neurophysiology*. 1, 76

Parekh, R. and G. A. Ascoli (2013). Neuronal morphology goes digital: a research hub for cellular and system neuroscience. *Neuron 77*(6), 1017–1038. 74

Park, T. J. and G. D. Pollak (1994). Azimuthal receptive fields are shaped by GABAergic inhibition in the inferior colliculus of the mustache bat. *Journal of Neurophysiology*. 29

Pastalkova, E., V. Itskov, A. Amarasingham, and G. Buzsáki (2008). Internally generated cell assembly sequences in the rat hippocampus. *Science 321*(5894), 1322–1327. 19

Perez-Velazquez, J. L., T. A. Valiante, and P. L. Carlen (1994). Modulation of gap junctional mechanisms during calcium-free induced field burst activity: a possible role for electrotonic coupling in epileptogenesis. *The Journal of neuroscience : The official Journal of the Society for Neuroscience 14*(7), 4308–17. 17

Perkel, D. H. and T. Holmes Bullock (1968). Neural Coding: A report based on an NRP work session. *N Neurosciences Research Program Neurosciences Res. Prog. Bull*. 77

Peyrache, A., F. P. Battaglia, and A. Destexhe (2011). Inhibition recruitment in prefrontal cortex during sleep spindles and gating of hippocampal inputs. *Proceedings of the National Academy of Sciences 108*(41), 17207–17212. 20

Pfeiffer, B. E. and D. J. Foster (2013). Hippocampal place-cell sequences depict future paths to remembered goals. *Nature 497*(7447), 74–79. 17

Prescott, S. A., S. Ratté, Y. De Koninck, and T. J. Sejnowski (2006). Nonlinear interaction between shunting and adaptation controls a switch between integration and coincidence detection in pyramidal neurons. *Journal of Neuroscience 26*(36), 9084–9097. 80

Preston, A. R., Y. Shrager, N. M. Dudukovic, and J. D. E. Gabrieli (2004). Hippocampal contribution to the novel use of relational information in declarative memory. *Hippocampus 14*(2), 148–152. 4

Ramón y Cajal, S. (1909). *Histologie du Systeme Nerveux de l'Homme et des Vertebres.* 29

Ratté, S., S. Hong, E. DeSchutter, and S. A. Prescott (2013). Impact of neuronal properties on network coding: Roles of spike initiation dynamics and robust synchrony transfer. 1, 34, 77, 78

Redish, A. D. and D. S. Touretzky (1997). Cognitive maps beyond the hippocampus. [Review] [182 refs]. *Hippocampus. 7*(August 1996), 15–35. 3

Rose, J. E., J. F. Brugge, D. J. Anderson, and J. E. Hind (1967). Phase-locked response to low-frequency tones in single auditory nerve fibers of the squirrel monkey. *Journal of Neurophysiology*. 29

Rudolph, M. and A. Destexhe (2003). Gain modulation and frequency locking under conductance noise. *Neurocomputing*. 76

Ryan, A. (1976). Hearing sensitivity of the mongolian gerbil, Meriones unguiculatis. *The Journal of the Acoustical Society of America 59*(5), 1222. 27

Ryugo, D. K. and S. Sento (1991). Synaptic connections of the auditory nerve in cats: Relationship between endbulbs of held and spherical bushy cells. *Journal of Comparative Neurology*. 28

Sanders, H., C. Rennó-Costa, M. Idiart, and J. Lisman (2015). Grid cells and place cells: an integrated view of their navigational and memory function. *Trends in neurosciences 38*(12), 763–775. 10

Sargolini, F., M. Fyhn, T. Hafting, B. L. McNaughton, M. P. Witter, M. B. Moser, and E. I. Moser (2006). Conjunctive representation of position, direction, and velocity in entorhinal cortex. *Science 312*(5774), 758–762. 11

Schmitz, D., S. Schuchmann, A. Fisahn, A. Draguhn, E. H. Buhl, E. Petrasch-Parwez, R. Dermietzel, U. Heinemann, and R. D. Traub (2001). Axo-axonal

coupling: A novel mechanism for ultrafast neuronal communication. *Neuron 31*(5), 831–840. 17

Schneggenburger, R. and I. D. Forsythe (2006). The calyx of held. *Cell and tissue research 326*(2), 311–337. 28

Scott, L. L., P. J. Mathews, and N. L. Golding (2005). Posthearing developmental refinement of temporal processing in principal neurons of the medial superior olive. *Journal of Neuroscience 25*(35), 7887–7895. 2, 78

Scoville, W. B. and B. Milner (1957). Loss of recent memory after bilateral hippocampal lesions. *Journal of neurology, neurosurgery, and psychiatry 20*(1), 11. 3

Shim, G. M., D. Kim, and M. Y. Choi (1991). Statistical-mechanical formulation of the Willshaw model with local inhibition. *Physical Review A 43*(12), 7012–7018. 25

Shu, Y., A. Hasenstaub, M. Badoual, T. Bal, and D. A. McCormick (2003). Barrages of synaptic activity control the gain and sensitivity of cortical neurons. *The Journal of Neuroscience : The official Journal of the Society for Neuroscience*. 77

Sirota, A., S. Montgomery, S. Fujisawa, Y. Isomura, M. Zugaro, and G. Buzsáki (2008). Entrainment of neocortical neurons and gamma oscillations by the hippocampal theta rhythm. *Neuron 60*(4), 683–697. 14

Skaggs, W. E., B. L. McNaughton, M. A. Wilson, and C. A. Barnes (1996). Theta phase precession in hippocampal neuronal populations and the compression of temporal sequences. *Hippocampus 6*(2), 149–172. 14

Skottun, B. C. (1998). Sound localization and neurons. *Nature 393*(6685), 531–531. 32

Solstad, T., T. Solstad, C. N. Boccara, C. N. Boccara, E. Kropff, E. Kropff, M.-B. Moser, M.-B. Moser, E. I. Moser, and E. I. Moser (2008). Representation of geometric borders in the entorhinal cortex. *Science 322*(December), 1865–1868. 11

Spruston, N. (2008). Pyramidal neurons: dendritic structure and synaptic integration. *Nature Reviews Neuroscience 9*(3), 206–221. 6

Squire, L. R. (1992). ”Memory and the hippocampus: A synthesis from findings with rats, monkeys, and humans”: Correction. *Psychological Review 99*(3), 582. 18

Squire, L. R. and S. M. Zola (1996). Structure and function of declarative and nondeclarative memory systems. *Proceedings of the National Academy of Sciences 93*(24), 13515–13522. 18

Squire, L. R. and S. M. Zola-Morgan (1988). Memory: brain systems and behavior. *Trends in neurosciences 11*, 170–175. 18

Stacey, W. C. and D. M. Durand (2000). Stochastic resonance improves signal detection in hippocampal ca1 neurons. *Journal of Neurophysiology 83*(3), 1394–1402. 78

Stacey, W. C. and D. M. Durand (2001). Synaptic Noise Improves Detection of Subthreshold Signals in Hippocampal CA1 Neurons. *Journal of Neurophysiology*. 78

Stark, E., L. Roux, R. Eichler, Y. Senzai, S. Royer, and G. Buzsáki (2014). Pyramidal cell-interneuron interactions underlie hippocampal ripple oscillations. *Neuron 83*(2), 467–480. 16

Steriade, M., I. Timofeev, and F. Grenier (2001). Natural waking and sleep states: a view from inside neocortical neurons. *Journal of neurophysiology 85*(5), 1969–1985. 77

Steward, O. and S. A. Scoville (1976). Cells of origin of entorhinal cortical afferents to the hippocampus and fascia dentata of the rat. *Journal of Comparative Neurology 169*(3), 347–370. 5

Stotler, W. A. (1953). An experimental study of the cells and connections of the superior olivary complex of the cat. *Journal of Comparative Neurology*. 30

Strutt (Lord Rayleigh), J. W. (1907). On our perception of sound direction. *Philosophical Magazine Series 6*. 28

Sullivan, D., J. Csicsvari, K. Mizuseki, S. Montgomery, K. Diba, and G. Buzsáki (2011). Relationships between hippocampal sharp waves, ripples, and fast gamma oscillation: influence of dentate and entorhinal cortical activity. *Journal of Neuroscience 31*(23), 8605–8616. 15

Svirskis, G., V. Kotak, D. H. Sanes, and J. Rinzel (2004). Sodium along with low-threshold potassium currents enhance coincidence detection of subthreshold noisy signals in mso neurons. *Journal of neurophysiology 91*(6), 2465–2473. 34, 78, 79

Taube, J. S., R. U. Muller, and J. B. Ranck (1990a). Head-direction cells recorded from the postsubiculum in freely moving rats. i. description and quantitative analysis. *Journal of Neuroscience 10*(2), 420–435. 11

Taube, J. S., R. U. Muller, and J. B. Ranck, JB (1990b). Head-direction cells recorded from the postsubiculum in freely moving rats. II. Effects of environmental manipulations. *J. Neurosci. 10*(2), 436–447. 11

Taxidis, J., S. Coombes, R. Mason, and M. R. Owen (2012). Modeling sharp wave-ripple complexes through a CA3-CA1 network model with chemical synapses. *Hippocampus 22*(5), 995–1017. 16

Thome, C., T. Kelly, A. Yanez, C. Schultz, M. Engelhardt, S. B. Cambridge, M. Both, A. Draguhn, H. Beck, and A. V. Egorov (2014). Axon-carrying dendrites convey privileged synaptic input in hippocampal neurons. *Neuron 83*(6), 1418–1430. 74

Thompson, S. P. (1882). On the function of the two ears in the perception of space. *The London, Edinburgh, and Dublin Philosophical Magazine and Journal of Science 13*, 406—-416. 27

Tollin, D. J. (2005). Interaural Phase and Level Difference Sensitivity in Low-Frequency Neurons in the Lateral Superior Olive. *Journal of Neuroscience 25*(46), 10648–10657. 29

Tóth, K. and T. F. Freund (1992). Calbindin D28k-containing nonpyramidal cells in the rat hippocampus: Their immunoreactivity for GABA and projection to the medial septum. *Neuroscience 49*(4), 793–805. 13

Traub, R. D. and A. Bibbig (2000). A model of high-frequency ripples in the hippocampus based on synaptic coupling plus axon-axon gap junctions between pyramidal neurons. *The Journal of neuroscience 20*(6), 2086–2093. 17

Van Hoesen, G. W., D. N. Pandya, and N. Butters (1975). Some connections of the entorhinal (area 28) and perirhinal (area 35) cortices of the rhesus monkey. II. Frontal lobe afferents. *Brain Research 95*(1), 25–38. 7

Van Wanrooij, M. M. (2004). Contribution of Head Shadow and Pinna Cues to Chronic Monaural Sound Localization. *Journal of Neuroscience 24*(17), 4163–4171. 26

Vorhees, C. V. and M. T. Williams (2006). Morris water maze: Procedures for assessing spatial and related forms of learning and memory. *Nature Protocols 1*(2), 848–858. 20

Werthat, F., O. Alexandrova, B. Grothe, and U. Koch (2008). Experience-dependent refinement of the inhibitory axons projecting to the medial superior olive. *Developmental Neurobiology*. 30

Willshaw, D. J., O. P. Buneman, and H. C. Longuet-Higgins (1969). Non-holographic associative memory. *Nature 222*(5197), 960–962. 25

Wilson, M. A. and B. L. McNaughton (1993). Dynamics of the hippocampal ensemble code for space. *Science 261*(5124), 1055–1058. 9

Wilson, M. A. and B. L. McNaughton (1994). Reactivation of hippocampal ensemble memories during sleep. *Science 265*(5172), 676–679. 16, 33

Winograd, T. (1975). Frame representations and the declarative / procedural controversy. *Representation and Understanding: Studies in Cognitive Science*, 185–210. 18

Winson, J. (1978). Loss of hippocampal theta rhythm results in spatial memory deficit in the rat. *Science 201*(4351), 160–163. 14

Witter, M. P., A. W. Griffioen, B. Jorritsma-Byham, and J. L. Krijnen (1988). Entorhinal projections to the hippocampal CA1 region in the rat: An underestimated pathway. *Neuroscience Letters 85*(2), 193–198. 8

Witter, M. P., P. A. Naber, T. Van Haeften, W. C. M. Machielsen, S. A. R. B. Rombouts, F. Barkhof, P. Scheltens, and F. H. Lopes Da Silva (2000). Cortico-hippocampal communication by way of parallel parahippocampal-subicular pathways. *Hippocampus 10*(4), 398–410. 5, 8

Witter, M. P., F. G. Wouterlood, P. A. Naber, and T. Van Haeften (2000). Anatomical organization of the parahippocampal-hippocampal network. *Annals of the New York Academy of Sciences 911*(1), 1–24. 5

Ylinen, A., A. Bragin, Z. Nádasdy, G. Jandó, I. Szabo, A. Sik, and G. Buzsáki (1995). Sharp wave-associated high-frequency oscillation (200 hz) in the intact hippocampus: network and intracellular mechanisms. *Journal of Neuroscience 15*(1), 30–46. 16

Zerlaut, Y. and A. Destexhe (2017). Enhanced responsiveness and low-level awareness in stochastic network states. *Neuron 94*(5), 1002–1009. 76

List of publications

Lehnert S; Ford MC; Alexandrowa O; **Hellmundt F**; Felmy F; Grothe B; Leibold C (2014) *Action Potential Generation in an Anatomically Constrained Model of Medial Superior Olive Axons* J Neurosci 34: 5370-5384.
doi: 10.1523/JNEUROSCI.4038-13.2014

Thurley K; **Hellmundt F**; Leibold C (2013) *Phase Precession of Grid Cells in a Network Model without External Pacemaker* Hippocampus 23: 786-796.
doi: 10.1002/hipo.22133.

Eidesstattliche Versicherung/Affidavit

Hiermit versichere ich an Eides statt, dass ich die vorliegende Dissertation Computation in the High-Conductance state selbstständig angefertigt habe, mich außer der angegebenen keiner weiteren Hilfsmittel bedient und alle Erkenntnisse, die aus dem Schrifttum ganz oder annähernd übernommen sind, als solche kentlich gemacht und nach ihrer Herkunft unter Bezeichnung der Fundstelle einzeln nachgewiesen habe.

I hereby confirm that the dissertation Computation in the High-Conductance State is the result of my own work and that I have only used sources or materials listed and specified in the dissertation.

München, den 28. September 2020 Franziska Hellmundt

Author Contributions

Chapter 2 is an unpublished manuscript. The work was done under the supervision of Christian Leibold (CL). Franziska Hellmundt (FH) and CL conceived and designed the research. FH wrote the code, carried out the simulations and analyzed the data. FH and CL discussed the results and wrote the manuscript.

Chapter 3 was published in *The Journal of Neuroscience* (Lehnert et al., 2014). Simon Lehnert (SL), Marc C. Ford (MCF), Olga Alexandrova (OA), Felix Felmy (FF), Benedikt Grothe (BG), and Christian Leibold (CL) designed the research. SL performed the computational modeling. Morphometric measurements were performed by MCF, and OA. FH and FF performed the electrophysiological recordings. SL, MCF, OA, FH, and FH analyzed the data. SL, MCF, FF, BG, and CL wrote the paper.

Munich, July 2019

Franziska Hellmundt Christian Leibold